Nanoscale GaN Epitaxy and Polytype Selection in Liquid-metal Mediated Environments and Writing-to-Learn in Materials Science and Engineering

by

Hongling Lott

A dissertation submitted in partial fulfillment
of the requirements for the degree of
Doctor of Philosophy
(Materials Science and Engineering)
in the University of Michigan
2023

Doctoral Committee:

Professor Rachel S. Goldman, Chair
Professor Hui Deng
Associate Professor Liang Qi
Associate Professor Ginger Shultz
Professor Judith Yang, Brookhaven National Laboratory

Hongling Lu

hlingl@umich.edu

ORCID iD: 0000-0001-5758-6645

Acknowledgements

I would like to thank my advisor, Rachel Goldman, for her support throughout my studies at the University of Michigan, as well as Prof. Judith Yang, Prof. Liang Qi, Prof. Hui Deng, and Prof. Ginger Shultz for their time, patience, and guidance as members of my dissertation committee. I would like to thank Dr. Ovidiu Toader from Michigan Ion Beam Lab for his help and support on our vacuum system leak checking and maintenance on our cryopump. I would like to thank Dr. Kai Sun at Michigan Ion Beam Lab and Dr. Dmitri Zakharov at Brookhaven National Lab for their insight on transmission electron microscopy to help us understand epitaxial relationships in our indium nanoparticles.

This dissertation would not have been possible without the support of my fellow group members, past and present. Your tenacity, kindness, and passion inspire me. Thank you especially to my mentors from the group: Dr. Christian Greenhill, Dr. Davide Del Gaudio, and Dr. Jordan Occena. Thank you, my MBE teammates: Jared Mitchell, Joshua Cooper, Hailey Lovelace, and Abby Liu. Thank you, my labmates from STM lab: Tao-Yu Huang, Sam Frisone, Armando Gil, and Yu-Chen Yang. Thank you, undergraduate researchers that I have worked with over the years: Ethan Lu, Andra Chen, Jiaheng He, Jason (Guanjie) Cheng, Arianna Wu and Erdem Ozdemir. Last but not least, thank you Thales Borrely.

I would like to thank the following people for their friendship and support: Alex Sun, Xinyan Wang, David Xu, Xinjing Huang, Sicen Du, Andong Chen, Junding Wang, Junhong Guo, Dejiu Fan, Zac Zhang, and Haoyue Zhu. I would like to thank my therapist Jordan Cusumano for

her support, and GGD group for those fun evenings we had, while I was completing this thesis. There are so many people I wish to thank than I can possibly list here. My personal and professional success on this journey would not have been possible without them.

I deeply thank you and miss you, mom, and dad.

Thank you Kougar Lott. I love you very much.

I gratefully acknowledge support from the National Science Foundation through the Materials Research Science and Engineering Center at the University of Michigan, under Grant No. DMR-1120923, Grant No. ECCS-1610362, and DMR-1410282. For the Writing to Learn project I gratefully acknowledge the UM Provost's Third Century Initiative for financial support of the MWrite program. We also gratefully acknowledge Anne Ruggles Gere and Ginger Shultz for their leadership of the MWrite program, which has provided support for the development and implementation of WTL in the introductory materials science and engineering courses.

Table of Contents

List of Figures

List of Tables

List of Appendices

Abstract

Most low dimensional materials possess properties different from their bulk counterparts and can be engineered to exhibit a wide range of physical properties for the fabrication of electronic, optoelectronic, and quantum devices. In the case of epitaxial nitride nanostructures, the role of liquid-metal-mediated environments on the polytype selection and layer dimensionality (i.e., films, NWs, and QDs) remains controversial. To elucidate the role of group-III metals (i.e., In and Ga) on nanostructure formation, we utilize advanced experimental and computational tools to monitor fundamental processes across growth conditions. In particular, droplet epitaxy of GaN and InN QDs, and the formation mechanism and crystal structure (polytype) selections of GaN nanowires on Si(001) were investigated in the thesis.

First, the formation mechanisms of GaN quantum dots (QDs) via annealing of Ga droplets in a nitrogen flux using a combined computational-experimental approach are presented. Temperature- and substrate-dependence of the size distributions of droplets and QDs, as well as the relative roles of Ga/N diffusivity and GaN nucleation rates on QD formation are considered. The relative roles of nucleation- and coarsening-dominant growth, as well as zincblende vs wurtzite polytype selection, on various substrates are discussed. These insights provide an opportunity for tailoring QD size distributions and polytype selection for a wide range of III-N semiconductor QDs.

Next, the formation of InN QDs during nitridation of In droplets was examined using ETEM and HRTEM. As the substrate temperature increases, the nanoparticle (NP) sizes decrease,

while their density increases; meanwhile moiré pattern formation suggests the formation of coherently strained InN/In2O3 interfaces. At the lowest nitridation temperatures, the smallest NPs primarily exhibited 2D moiré fringes (MF) suggesting ZB InN formation. At the highest nitridation temperatures, larger NPs primarily exhibited 1D MF. We hypothesize that there is a higher probability of ZB nucleation from smaller particles and WZ nucleation from larger particles, with unintentional In_2O_3 formation on InN.

Furthermore, the influence of Ga surface saturation on GaN nanowire (NW) polytype selection is examined. The Ga surface saturation in the absence and presence of nitrogen determines the GaN polytype and morphology selection, respectively. The interplay between surface and step-edge diffusion barriers governing the NW-to-film-transition and the influence of Si_xN_y interlayer formation on zinc blende (ZB) vs wurtzite (WZ) polytype selection of GaN is discussed. In addition, distinct exciton emissions associated with ZB and WZ GaN are observed, suggesting a type-I WZ/ZB GaN band-offset. This work provides a crucial step toward the realization of polarization-free GaN-based optoelectronics.

Finally, I discuss the impact of writing-to-learn (WTL) on promoting conceptual understanding of introductory materials science and engineering. Our WTL process asks students to write a response to a prompt, performing, and receiving content-focused peer review, and finally revising their initial response. MSE concept-inventory-style assessment is used to analyze students' gain in conceptual knowledge. Across topics, the normalized gains that reflect conceptual knowledge gain are highest for students who completed WTL. These gains imply the presence of an additional source of learning beyond that of the traditional course components. Details of the findings and suggestions of strategies for future WTL design and implementation are presented.

Chapter 1

Introduction

1.1 Overview

This chapter opens with discussion of polytype selection in compounds. Two polytypes of III-N materials, namely wurtzite (WZ) and zincblende (ZB), are introduced in Section 1.2. Following the introduction of WZ and ZB, Section 1.3 and Section 1.4 discuss the droplet epitaxy (DE) of III-N quantum dots (QDs) and epitaxial III-N nanowires (NWs), respectively. The applications of nanoparticles and nanostructures, including droplets, QDs, and NWs, are also discussed in Section 1.3 and Section 1.4. Finally, this chapter concludes with an outline and objectives of the dissertation in Section 1.5.

1.2 Polytype selection in compounds

Many solid-state materials are polymorphic, i.e., they are able to crystallize in multiple-crystal structures, called polytypes. However, only those with a single thermodynamically preferred polytype[1,2,3] have become ubiquitous for electronics and optoelectronics. For example, as shown in Figure 1.1, III-V semiconductors, which prefer the ZB polytype, are the building blocks for infrared optoelectronics and high efficiency photovoltaics. WZ polytype exhibits a spontaneous polarization [4], which is useful for separating charge in photodetectors and photovoltaics, while the ZB polytype lacks a spontaneous polarization and exhibits enhanced p-type doping,[5,6] both of which facilitate efficient carrier recombination for light-emitters.

Furthermore, III-N semiconductors, which prefer the WZ polytype, are fueling a revolution in visible to ultraviolet light-emission and high-power electronics.[7,8] On the other hand, some II-VI semiconductors, which were initially associated with visible phosphorescence, are thermodynamically favored to crystallize in both the ZB and WZ polytype. Indeed, many attempts to utilize II-VI semiconductors for visible light emission ultimately resulted in devices with insufficient long-term reliability. Indeed, semiconductor polytype heterostructures, which consist of chemically homogeneous structures formed via an abrupt change in crystal structure, offer opportunities for performance exceeding those of composition-based semiconductor heterostructures.

In contrast to bulk systems whose polytype selection is determined by thermodynamics (Figure 1.2),[2,3] it has been hypothesized that NW polytype selection is governed by surface/interface energies[9], surface diffusivities[10], and/or droplet contact angles[64,11] that determine ABC vs. AB stacking of atomic planes, resulting in ZB or WZ polytypes. For GaN, a WZ-polytype preferring material, the "contact angle" models for NW polytype selection, using literature values for WZ and ZB GaN surface energies[12,13], would predict ZB polytype formation, across contact angles, even though WZ GaN NWs are most frequently reported in the literature[14,15,71,16].

For polymorphic materials with a thermodynamically-preferred polytype, the presence of multiple polytypes during thin film epitaxy is typically attributed to a flawed synthesis process. On the other hand, in the case of NWs, unintentional polytype superlattices have been reported to be promising for crystal phase quantum dots.[17] During plasma-assisted MBE of GaN, it has been shown that high Ga fluxes increase the surface temperature;[18] however, the increase is likely insufficient to induce a transition from ZB to WZ GaN.[19] Substrate-biasing-induced selection of ZB vs. WZ GaN is attributed to suppression of Ga desorption,[20,21] without consideration of

polarization effects. Interestingly, it has been shown that charged particles induce the selection of the metastable WZ polytype during chemical vapor deposition of ZnS.[22] Further understanding of the ZB-to-WZ transformation will provide a new tool for inducing such transformations at will.

1.3 Droplet epitaxy of III-N quantum dots

Quantum dots (QDs) are low dimensional nanostructures with size <100 nm in three directions. III-nitride QDs structures are becoming increasingly important as active regions of various (opto)electronic devices, such as solar cells,[23,24] light-emitting diodes,[25,26,27] lasers,[28,29] and single-photon emitters.[30,31] In the early 1990s, two bottom-up epitaxial approaches emerged, leading to self-assembled QDs of III-V semiconductor materials, namely the Stranski–Krastanov (SK) growth mode, which consists of three-dimensional island formation on top of a thin wetting layer (WL),[32,33] and the droplet epitaxy (DE) method, exploiting the controlled conversion of metal nanodroplets to semiconductor.[34] Compared to SK, DE offers additional advantages that overcome problems in SK.[35] Thus, understanding DE is critical for elucidation of the mechanisms for III-nitride QD growth under liquid-metal mediated environment. QDs growth via DE can also lead to low impurity incorporation. For example, in Ga-rich growth, the low solubility of carbon in some metal melts can lead to low carbon incorporation into the QDs.[36] In the case of GaN QDs, the reactivity of oxygen in Ga, with subsequent desorption of GaO at growth temperatures, can lead to low oxygen incorporation.[37] Despite the great potential of DE, the higher degree of freedom also makes the controlling of size, shape, and distribution of quantum dots more challenging than other methods such as S-K growth. Thus, developing an understanding of the nanoscale mechanism of DE is critical. However, the formation mechanisms of DE are still a matter of debate.

Beyond Ga nanoparticles (NPs) and GaN QDs, In NPs and InN QDs have received increased interest for enhancing the performance of power electronics, optoelectronics, and light

harvesting. [38,39,40,41,42] InN is predicted to exhibit high electron mobility (~4000−5000 $cm^2/(Vs)$), and low electron effective mass (~0.1 m_{e0}). [43,44,45] The room temperature bandgap of WZ InN was reported to be 0.7-0.9 eV,[42,46] which makes InN an exciting material for near infrared LED applications. Notably, these reports disagree with older studies that found the bandgap of InN to be 1.7-1.8 eV.[47,48] Bandgap widening in with higher oxygen impurity concentrations has been demonstrated in WZ InN,[49] leading to the hypothesis that older bandgap measurements were higher than modern reports because of oxygen incorporation. Conversely, the bandgap of zinc-blende (ZB) InN is predicted to be 0.58 eV,[50] offering an appealing possibility to further extend the available ranges of low wavelength LED devices. Additionally, the bandgap of WZ InN QDs was shown to increase from 0.67 eV to 0.85 eV as QD diameters decreased from 32 nm to 4.5 nm.[51] Considering the lower bandgap of ZB InN, control over WZ/ZB polytype selection could further expand low energy tunability for light collection and emission by InN QDs. While polytype selection between WZ and ZB in bulk materials is thermodynamically governed, [52,53] substrate/droplet contact angles,[54,55] surface/interfacial energies,[56] and surface diffusivities[57] are predicted to determine WZ/ZB polytype selection in processes such as QD formation.

1.4 Epitaxial III-N nanowires

Epitaxial III-N nanowires (NWs) are low dimensional nanostructures with diameters < 100 nm and length exceeding the diameter. For a cylindrical NW grown on a substrate, there are free surfaces on the top and on the sides. Thus, nanowire possesses large surface-to-volume ratio, and the strain-induced polarization in the material is reduced relative to that of bulk films.[58] This reduction of strain-induced polarization makes NWs promising for a wide range of optical and electronic applications.[59] Synthesis of nanoscale crystals has been pursued with both top-down[60] and bottom-up[61] approaches. For nanowires, an especially promising bottom-up approach to

fabrication involves metal catalysis.[62] Generally, liquid metal droplets act as catalysts, which allow gaseous species to be transformed into a nanoscale crystal in the vicinity of the vapor-liquid-solid (VLS) triple junction. The metal droplet catalysts can be the same group III material as used for the III-N nanowire, or they can be foreign metal, such as gold.[63,64] However, there are a few problems with using foreign metal droplets as catalysts. Foreign materials, which are commonly used as catalysts in VLS growth method, introduce contamination in NWs and subsequently deteriorate optical and structural quality.[65] In addition, noble metals and their alloys are also incompatible with practical semiconducting applications.[66,67] Thus there is a need to study and develop self-catalyzed (or "self-assisted") epitaxy for which extrinsic metal droplets are not utilized. In such self-catalyzed epitaxy, the contamination and incompatibility issues are minimized. However, compared to the self-assembly of NW with foreign noble metal droplets as catalysts, it is still in debate whether liquid metal droplets are present, continuously supplied, and consumed during self-catalyzed NWs growth.[68,69]

In addition, a framework for nanoscale morphology (i.e., film vs. NW) selection during self-assembly without external catalysis has yet to emerge. Currently, the transitions from island to NW growth have been attributed to surface energy anisotropies,[70] while selection of NWs vs. films has been attributed to differences in sticking coefficients[71] and diffusivities[72,73] on polar vs. non-polar planes. This thesis studies the mechanism of self-catalyzed NWs and the mechanisms for NW and film transitions, influenced by Ga surface saturation. Chapter 5 examines the influence of Ga surface saturation on GaN nanowire polytype selection during molecular-beam epitaxy (MBE) on Si(001). I discuss the interplay between surface and step-edge diffusion barriers governing the NW-to-film transition and reveal the influence of Si_xN_y interlayer formation on the selection of the ZB vs. WZ polytype. In addition, distinct exciton emissions associated with ZB

and WZ GaN suggest a type-I WZ/ZB GaN band-offset. These findings are expected to be applicable to a wide range of III-nitride alloys and heterostructures.

1.5 Dissertation objectives and organization

This dissertation is organized as follows. In Chapter 2, we describe the experimental methods used for this thesis work, including molecular beam epitaxy (MBE), reflection high-energy electron diffraction (RHEED), and atomic force microscopy (AFM).

In Chapter 3, we discuss the formation mechanisms of GaN quantum dots (QDs) via annealing of Ga droplets in a nitrogen flux. We consider the temperature- and substrate-dependence of the size distributions of droplets and QDs, as well as the relative roles of Ga/N diffusivity and GaN nucleation rates on QD formation. We report on two competing mechanisms mediated by Ga surface diffusion, namely, QD formation at or away from pre-existing Ga droplets. We discuss the relative roles of nucleation- and coarsening-dominant growth, as well as zincblende vs. wurtzite polytype selection, on various substrates. These insights provide an opportunity for tailoring QD size distributions and polytype selection for a wide range of III-N semiconductor QDs.

In Chapter 4, we present our investigation of environmental transmission electron microscopy (ETEM) studies of nitridation of In droplets. In this work, we study the In droplet deposition via MBE on Si(001) single crystal TEM film and the subsequent nitridation of In droplets in ETEM. In ETEM, we observed temperature-dependent size change of the observed nanoparticles as well as the formation of a moiré pattern suggesting the nucleation of crystallites during the nitridation process. The epitaxy is further examined under TEM. These observations provide insight into the transformation of indium nanoparticles into InN. The experimental details of In deposition and nitridation in ETEM are described in Sections 2.3.2 and 2.6.

In Chapter 5, we discuss the influence of Ga surface saturation on gallium nitride (GaN) nanowire (NW) polytype selection during molecular-beam epitaxy. The Ga surface saturation in the absence and presence of nitrogen determines the GaN polytype and morphology (i.e., films vs. NW) selection, respectively. We discuss the interplay between surface and step-edge diffusion barriers governing the NW-to-film-transition and the influence of Si_xN_y interlayer formation on ZB vs WZ polytype selection of GaN. In addition, distinct exciton emissions associated with ZB and WZ GaN are observed, suggesting a type-I WZ/ZB GaN band-offset. This work provides a crucial step toward the realization of polarization-free, CMOS-compatible GaN-based optoelectronics.

In Chapter 6, we discuss the impact of writing-to-learn (WTL) on promoting conceptual understanding of introductory materials science and engineering, including crystal structures, stress–strain behavior, phase diagrams, and corrosion. We utilize a WTL process in which students write a response to a prompt conveying an authentic scenario, perform and receive content-focused peer review, and revise their initial response.[74] This three-step WTL process, as illustrated in Figure 1.3, incorporates the key elements for effective WTL assignments, including clearly defined and interactive writing expectations that incorporate meaning-making tasks and support metacognition, by increasing students' awareness of their own thinking processes through writing.[75,76] We use an analysis of writing products in comparison with pre/post concept-inventory-style assessments. For all topics, statistically significant improvements between draft and revision scores are apparent. For the stress–strain and phase diagram WTL assignments that require synthesis of qualitative data into quantitative formats while emphasizing microstructure-properties correlations, the highest WTL effect sizes and medium-to-high gains on corresponding

assessments are observed. We present these findings and suggest strategies for future WTL design and implementation. Finally, in Chapter 7, we present a summary and suggestions for future work.

1.6 Figures

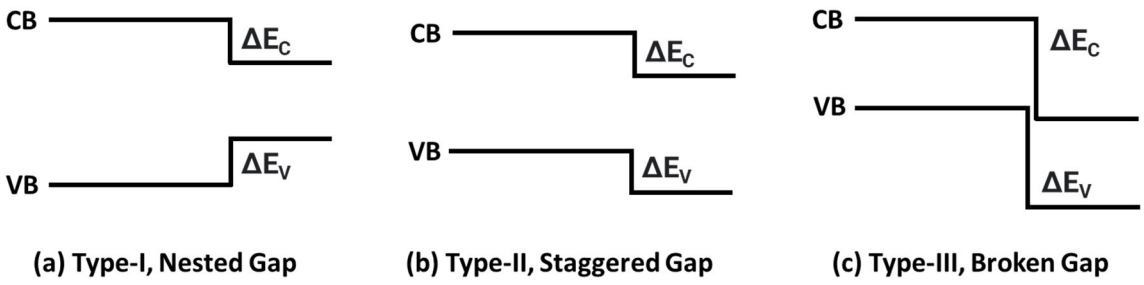

Figure 1.1 Three types of band alignment for semiconductor heterojunctions. (a) nested gap (type I), (b) staggered gap (type II), (c) broken gap (type III). The VB and CB represent the valance and conduction band positions, respectively. ΔE_V and ΔE_C represent the valance and conduction band offsets, respectively.

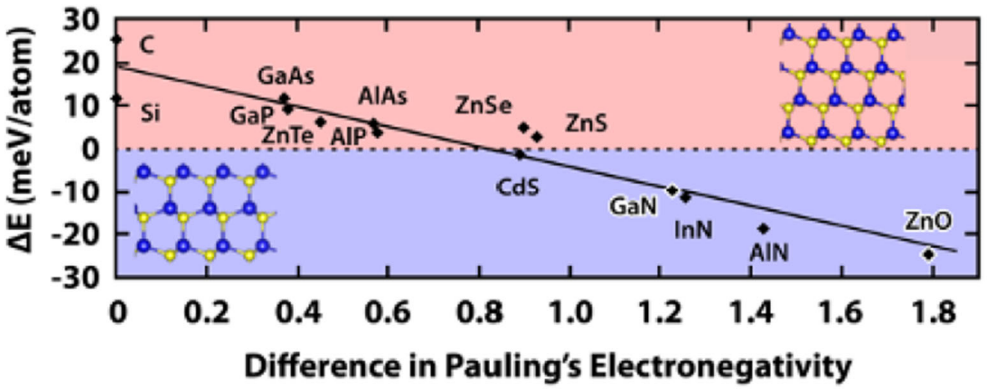

Figure 1.2 Difference in equilibrium formation energies for ABC stacking [zincblende (ZB)] vs. AB stacking [wurtzite (WZ)] of III-V compounds. For $\Delta E > 0$, the ZB polytype is preferred; for $\Delta E < 0$, the WZ polytype is preferred. Reuse figure with permission from Ref 2 (Copyright 1992, American Physical Society).

Figure 1.3 Each WTL assignment consists of an initial written response to a prompt ("draft"), anonymous open-response peer review performed by 2–3 randomly selected students ("peer review"), and a revision of the draft ("final submission"). Peer review is guided by content-focused rubrics, as shown in supplemental materials of Ref. 77. Reprinted figure with permission from Ref. 77 (Copyright 2022, Springer Nature Publishing).

1.7 References

[1] N.L. Adamski, C.E. Dreyer, and C.G. Van de Walle, "Radiative capture rates at deep defects from electronic structure calculations", Phys. Rev. B. 102, 201301 (2020).

[2] C.-Y. Yeh, Z.W. Lu, S. Froyen, and A. Zunger. "Zinc-blende–wurtzite polytypism in semiconductors", Phys. Rev. B. 46, 0086 (1992).

[3] T. Ito. "Simple Criterion for Wurtzite-Zinc-Blende Polytypism in Semiconductors", Jpn. J. Appl. Phys. 37, L1217 (1998).

[4] C.E. Dreyer, A. Janotti, C.G. Van de Walle, and D. Vanderbilt, "Correct Implementation of Polarization Constants in Wurtzite Materials and Impact on III-Nitrides", Phys. Rev. X. 6, 021038 (2016).

[5] C.A. Hernandez-Gutierrez, Y.L. Casallas-Moreno, V.-T. Rangel-Kuoppa, D. Cardona, Y.Q. Hu, Y. Kudriatsev, M.A. Zambrano-Serrano, S. Gallardo-Hernandez, and M. Lopez-Lopez, "Study of the heavily p-type doping of cubic GaN with Mg", Sci. Reports 10, 16858 (2020).

[6] Y.-C. Tsai, and C. Bayram. Comp. "Mitigate self-compensation with high crystal symmetry: A first-principles study of formation and activation of impurities in GaN", Mat. Sci. 190, 110283 (2021).

[7] S. Strite, M.E. Lin, and H. Morkoç, "Progress and prospects for GaN and the III–V nitride semiconductors", Thin Solid Films. 231, 197 (1993).

[8] R. Yakimova, "Developments in the growth of wide bandgap semiconductors", Phys. Scr. 2006 121 (2006).

[9] F. Glas, J.-C. Harmand, and G. Patriarche, "Why Does Wurtzite Form in Nanowires of III-V Zinc Blende Semiconductors?" Phys. Rev. Lett. 99, 146101 (2007).

[10] B. Puchala, M.L. Falk, and K. Garikipati, "An energy basin finding algorithm for kinetic Monte Carlo acceleration", J. Chem. Phys. 132, 134104 (2010).

[11] V.G. Dubrovskii, N.V. Sibirev, N.N. Halder, and D. Ritter, "Classification of the Morphologies and Related Crystal Phases of III–V Nanowires Based on the Surface Energy Analysis", J. Phys. Chem. C. 123, 18693 (2019).

[12] J.E. Northrup and J. Neugebauer. "Theory of GaN($10\bar{1}0$) and ($11\bar{2}0$) surfaces", Phys. Rev. B 53, R10477 (1996).

[13] U. Grossner, J. Furthmuller, and F. Bechstedt, "Bond-rotation versus bond-contraction relaxation of (110) surface of group-III nitrides", Phys. Rev. B 58, R1722 (1998).

[14] E. Calleja, M.A. Sanchez-Garcia, F.J. Sanchez, F. Calle, F.B. Naranjo, and E. Munoz, "Luminescence properties and defects in GaN nanocolumns grown by molecular beam epitaxy", Phys. Rev. B 62, 16826 (2000).

[15] H. Li, A.H. Chin, and M.K. Sunkara, "Direction-Dependent Homoepitaxial Growth of GaN Nanowires", Adv. Mat. 18, 216 (2006).

[16] W. Guo, M. Zhang, A. Banerjee, and P. Bhattacharya. "Catalyst-Free InGaN/GaN Nanowire Light Emitting Diodes Grown on (001) Silicon by Molecular Beam Epitaxy", Nano Lett. 10, 3355 (2010).

[17] P. Caroff, J. Bolinsson, and J. Johansson, "Crystal Phases in III--V Nanowires: From Random Toward Engineered Polytypism", IEEE Journal of Selected Topics in Quantum Electronics 17, 829 (2011).

[18] W. Hoke, D. Barlett, T. Kennedy, B. Wissman, and J. Mosca, "Short wavelength band edge thermometry during molecular beam epitaxial growth of GaN on SiC substrates and detected adatom self-heating effects", J. Vac. Sci. Technol. 28, C3F5 (2010).

[19] J. Yang, J. Kuznia, Q. Chen, M. Khan, T. George, M. DeGraef, and S. Mahajan, "Temperature-mediated phase selection during growth of GaN on (111)A and $(\bar{1}\bar{1}\bar{1})$B GaAs substrates", Appl. Phys. Lett. 67, 3759 (1995).

[20] T. Araki, T. Minami, M. Kijima, and Y. Nanishi, "Structural Control of Cubic and Hexagonal GaN by Changing the Electric Bias during ECR-MBE Growth", Phys. Stat. Sol. A, 188, 677 (2001).

[21] Y. Chiba, Y. Shimizu, T. Tominari, S. Hokuto, and Y. Nanishi, "Analysis of MBE growth mode for GaN epilayers by RHEED", J. Cryst. Growth, 189/190, 317 (1998).

[22] X. Hou and K. L. Choy, "Crystal growth of ZnS films by a charged aerosol-assisted vapor deposition process", Chem. Vap. Depos. 12, 631 (2006).

[23] L. Sang, M. Liao, Q. Liang, M. Takeguchi, B. Dierre, B. Shen, T. Sekiguchi, Y. Koide, and M. Sumiya," A Multilevel Intermediate-Band Solar Cell by InGaN/GaN Quantum Dots with a Strain-Modulated Structure", Adv. Mater. 26, 1414 (2014).

[24] Q. Deng, X. Wang, C. Yang, H. Xiao, C. Wang, H. Yin, Q. Hou, J. Li, Z. Wang, and X. Hou, "Theoretical study on $In_xGa_{1-x}N$/GaN quantum dots solar cell", Physica B 406, 73 (2011).

[25] B. Damilano, N. Grandjean, J. Semond, J. Massies, and M. Leroux, "From visible to white light emission by GaN quantum dots on Si(111) substrate", Appl. Phys. Lett. 75, 962 (1999).

[26] T. Egawa, B. Zhang, and H. Ishikawa, "High performance of InGaN LEDs on (111) silicon substrates grown by MOCVD", IEEE Electron Device Lett. 26, 169 (2005).

[27] M. Zhang, P. Bhattacharya, and W. Guo, "InGaN/GaN self-organized quantum dot green light emitting diodes with reduced efficiency droop", Appl. Phys. Lett. 97, 011103 (2010).

[28] T. Frost, A. Banerjee, K. Sun, S. L. Chuang, and P. Bhattacharya, "InGaN/GaN Quantum Dot Red (λ=630 nm) Laser", IEEE J. Quantum Electron 49, 923 (2013).

[29] M. Zhang, A. Banerjee, C.-S. Lee, J.M. Hinckley, and P. Bhattacharya, "A InGaN/GaN quantum dot green (λ=524 nm) laser", Appl. Phys. Lett. 98, 221104 (2011).

[30] S. Kako, C. Santori, K. Hoshino, S. Götzinger, Y. Yamamoto, and Y. Arakawa, "A gallium nitride single-photon source operating at 200 K", Nat. Mater. 5, 887 (2006).

[31] S. Kremling, C. Tessarek, H. Dartsch, S. Figge, S. Höfling, L. Worschech, C. Kruse, D. Hommel, and A. Forchel, "Single photon emission from InGaN/GaN quantum dots up to 50 K", Appl. Phys. Lett. 100, 061115 (2012).

[32] D. Eaglesham, and M. Cerullo, "Dislocation-free stranski-krastanow growth of Ge on Si (100)", Phys. Rev. Lett. 64, 1943 (1990).

[33] D. Leonard, M. Krishnamurthy, C.M. Reaves, S.P. Denbaars, and P.M. Petroff. "Direct formation of quantum-sized dots from uniform coherent islands of InGaAs on GaAs surfaces", Appl. Phys. Lett. 63, 3203 (1993).

[34] N. Koguchi, S. Takahashi, and T. Chikyow, "New MBE growth method for InSb quantum well boxes", J. Cryst. Growth 111, 688 (1991).

[35] J. Wu and Z.M. Wang, "Droplet epitaxy for advanced optoelectronic materials and devices", J. Phys. D: Appl. Phys. 47, 173001 (2014).

[36] T.F. Kuech, Handbook of Crystal Growth: Thin Films and Epitaxy: Basic Techniques (Elsevier, Burlington, 2014), p. 281.

[37] T.D. Moustakas and A. Bhattacharyya, "The role of liquid phase epitaxy during growth of AlGaN by MBE", Phys. Status Solidi C 9, 580 (2012).

[38] F.I. Chowdhury, K. Islam, S. Alkis, B. Ortaç, and M. Alevli, N, Dietz, A. Okyay, and A. Nayfeh, "Enhanced Light Scattering with Energy Downshifting Using 16 Nm Indium Nitride Nanoparticles for Improved Thin-Film a-Si N-I-P Solar Cells." ECS Trans. 66, 9 (2015).

[39] X. Wang, A. Yoshikawa, "Molecular Beam Epitaxy Growth of GaN, AlN and InN", Prog. Cryst. Growth Charact. Mater. 48, 42 (2004).

[40] T. Hoshino, and N. Mori, "Electron Mobility Calculation for Two-Dimensional Electron Gas in InN/GaN Digital Alloy Channel High Electron Mobility Transistors", Jpn. J. Appl. Phys. 58, SCCD10 (2019).

[41] H.K. Rouf, and J. Dey, "Indium Nanoparticle Enhanced Light Trapping in Thin Film Silicon Solar Cells", J. Nano- Electron. Phys. 10, 06008 (2018).

[42] J. Wu, W. Walukiewicz, K.M. Yu, J.W. Ager, E.E. Haller, H. Lu, W.J. Schaff, Y. Saito, and Y. Nanishi, "Unusual Properties of the Fundamental Band Gap of InN", Appl. Phys. Lett. 80, 3967 (2002).

[43] V.W.L. Chin, T.L. Tansley, and T. Osotchan, "Electron Mobilities in Gallium, Indium, and Aluminum Nitrides", J. Appl. Phys. 75, 7365 (1994).

[44] B.R. Nag, "Electron Mobility in Indium Nitride", J. Cryst. Growth, 269, 35 (2004).

[45] P. Carrier, S.-H. Wei, "Theoretical Study of the Band-Gap Anomaly of InN", J. Appl. Phys. 97, 033707 (2005).

[46] V.Y. Davydov, A.A. Klochikhin, R.P. Seisyan, V.V. Emtsev, S.V. Ivanov, F. Bechstedt, J. Furthmuller, H. Harima, A. Mudryi, J. Aderhold, O. Semchinova, and J. Graul, "Absorption and Emission of Hexagonal InN. Evidence of Narrow Fundamental Band Gap", Phys. Stat. Sol. (b). 229, r1 (2002).

[47] N. Puychevrier, and M. Menoret, "Synthesis of III–V Semiconductor Nitrides by Reactive Cathodic Sputtering", Thin Solid Films. 36, 141 (1976).

[48] K.L. Westra, and M.J. Brett, "Near IR Optical Properties of Sputtered InN Films". Thin Solid Films. 192, 227 (1990).

[49] Y. Uesaka, A. Yamamoto, and A. Hashimoto, "Band Gap Widening of MBE Grown InN Layers by Impurity Incorporation", J. Cryst. Growth, 278 402 (2005).

[50] F. Bechstedt, J. Furthmüller, M. Ferhat, L.K. Teles, L.M.R. Scolfaro, J.R. Leite, V.Y. Davydov, O. Ambacher, and R. Goldhahn, "Energy Gap and Optical Properties of $In_xGa_{1-x}N$. Physica Status Solidi (a) 195, 628 (2003).

[51] M. Kumar, M.K. Rajpalke, T.N. Bhat, B. Roul, A.T. Kalghatgi, and S.B. Krupanidhi, "Size Dependent Bandgap of Molecular Beam Epitaxy Grown InN Quantum Dots Measured by Scanning Tunneling Spectroscopy", J. Appl. Phys. 110, 114317 (2011).

[52] C.Y. Yeh, Z.W. Lu, S. Froyen, and A. Zunger, "Zinc-Blende–Wurtzite Polytypism in Semiconductors", Phys. Rev. 46, 10086 (1992).

[53] T. Ito, "Simple Criterion for Wurtzite-Zinc-Blende Polytypism in Semiconductors", Jpn. J. Appl. Phys. 37, L1217 (1998).

[54] D. Jacobsson, F. Panciera, J. Tersoff, M.C. Reuter, S. Lehmann, S. Hofmann, K.A. Dick, and F.M. Ross, "Interface Dynamics and Crystal Phase Switching in GaAs Nanowires", Nature, 531, 317 (2016).

[55] V.G. Dubrovskii, N.V. Sibirev, N.N. Halder, and D. Ritter, "Classification of the Morphologies and Related Crystal Phases of III–V Nanowires Based on the Surface Energy Analysis". J. Phys. Chem. C. 123, 18693 (2019).

[56] F. Glas, J.C. Harmand, and G. Patriarche, "Why Does Wurtzite Form in Nanowires of III-V Zinc Blende Semiconductors?" Phys. Rev. Lett. 99, 146101 (2007).

[57] V. Pankoke, S. Sakong, and P. Kratzer, "Role of Sidewall Diffusion in GaAs Nanowire Growth: A First-Principles Study", Phys. Rev. B. 86, 085425 (2012).

[58] N.P. Dasgupta, J.W. Sun, C. Liu, S. Brittman, S.C. Andrews, J.W. Lim, H.W. Gao, R.X. Yan, and P. Yang, "25th Anniversary Article: Semiconductor Nanowires – Synthesis, Characterization, and Applications", Adv. Mat. 26, 2137 (2014).

[59] C. Zhao, N. Alfaraj, R. C. Subedi, J. W. Liang, A. A. Alatawi, A. A. Alhamoud, M. Ebaid, M. S. Alias, T. K. Ng, and B. S. Ooi, "III-nitride nanowires on unconventional substrates: From materials to optoelectronic device applications", Prog. Quantum Electron. 61, 1 (2018).

[60] R.G. Hobbs, N. Petkov, and J.D. Holmes, "Semiconductor Nanowire Fabrication by Bottom-Up and Top-Down Paradigms", Chem. Mater. 24, 1975 (2012).

[61] R.S. Wagner and W.C. Ellis, "Vapor-liquid-solid mechanism of single crystal growth", Appl. Phys. Lett. 4, 89 (1964).

[62] W. Lu, and C.M. Lieber, "Nanoelectronics from the bottom up", Nat. Mat. 6, 841 (2007).

[63] C.Y. Wen, J. Bruley, J. Tersoff, S. Kodambaka, E.A. Stach, and F.M. Ross, "Formation of compositionally abrupt axial heterojunctions in Si/Ge nanowires", Science. 326, 1247 (2009).

[64] D. Jacobsson, F. Panciera, J. Tersoff, M.C. Reuter, S. Lehmann, S. Hofmann, K.A. Dick, and F.M. Ross, "Interface dynamics and crystal phase switching in GaAs nanowires", Nature. 531, 317 (2016).

[65] C. Chèze, L. Geelhaar, O. Brandt, W. M. Weber, H. Riechert, S. Münch, R. Rothemund, S. Reitzenstein, A. Forchel, T. Kehagias, P. Komninou, G. P. Dimitrakopulos, and T. Karakostas, "Direct comparison of catalyst-free and catalyst-induced GaN nanowires", Nano Res. 3, 528 (2010).

[66] G. Harbeke, Polycrystalline Semiconductors: Physical Properties and Applications: Proceedings of the International School of Materials Science and Technology at the Ettore Majorana Centre, Erice, Italy, July 1–15, 1984 Vol. 57. Springer Science & Business Media (2012).

[67] M-J Fang, C-W Tsao, and Y-J Hsu, "Semiconductor nanoheterostructures for photoconversion applications", J. Phys. D: Appl. Phys. 53 143001 (2020).

[68] K.A. Bertness, A. Roshko, L.M. Mansfield, T.E. Harvey, and N.A. Sanford "Mechanism for spontaneous growth of GaN nanowires with molecular-beam epitaxy" J. Cryst. Growth 310, 3154 (2008).

[69] C.E. Kendrick, Ph.D. Thesis, "Revisiting Nitride Semiconductors: Epilayers, p-Type Doping and Nanowires", University of Canterbury, pp. 80-112 (2008).

[70] V. Consonni, M. Hanke, M. Knelangen, L. Geelhaar, A. Trampert, and H. Reichert, "Nucleation mechanisms of self-induced GaN nanowires grown on an amorphous interlayer", Phys. Rev. B. 83, 035310 (2011).

[71] K.A. Bertness, A. Roshko, L.M. Mansfield, T.E. Harvey, and N.A. Sanford, "Mechanism for spontaneous growth of GaN nanowires with molecular beam epitaxy", J. Cryst. Growth 310, 3154 (2008).

[72] R.K. Debnath, R. Meijers, T. Richter, T. Stoica, R. Calarco, and H. Lüth, "Mechanism of molecular beam epitaxy growth of GaN nanowires on Si(111)", Appl. Phys. Lett. 90, 123117 (2007).

[73] V. Consonni, V.G. Dubrovskii, A. Trampert, L. Geelhaar, and H. Reichert, "Quantitative description for the growth rate of self-induced GaN nanowires", Phys. Rev. B. 85, 155313 (2012).

[74] S.A. Finkenstaedt-Quinn, M.N. Petterson, A. Gere, and G. Shultz, "Praxis of Writing-to-Learn: A Model for the Design and Propagation of Writing-to-Learn in STEM", J. Chem. Educ. 98, 1548 (2021).

[75] A.R. Gere, N. Limlamai, E. Wilson, K. MacDougall Saylor, R. Pugh, "Writing and conceptual learning in science: an analysis of assignments", Writ. Commun. 36, 99 (2019).

[76] G.M. Bodner, "Constructivism: a theory of knowledge", J. Chem. Educ. 63, 873 (1986).

[77] L. Marks, H. Lu, T. Chambers, and R. S. Goldman, "Writing-to-learn in introductory materials science and engineering", MRS Commun. 12, 1 (2022).

Chapter 2

Methods

2.1 Overview

This chapter describes the experimental techniques, procedures, and computational methods used in the thesis. Ga and In droplets and the GaN QDs and NWs were grown using GEN-II molecular beam epitaxy (MBE) system in Prof. Rachel Goldman's research group. The details and process of MBE are explained in Section 2.2. Ga droplets and GaN QDs and NWs samples studied in Chapter 3 and Chapter 5 were grown by Dr. Sunyeol Jeon on undoped semi-insulating Si(001) and Si(111) substrates. Reflection high energy electron diffraction (RHEED) was used to examined in-situ growth process and explained in detail in Section 2.3. Indium droplet samples studied in Chapter 4 were grown by Robert Polski and Dr. Sunyeol Jeon on SiMPore single crystal pure Si(001) film TEM grids (part #: US100-C25Q33A) that were indium mounted to Si(001) substrate. The process of the deposition and sample preparation is detailed in Section 2.3.2. Nitridation of In nanoparticles were performed under environmental TEM (ETEM), the details of which are explained in Section 2.6. The nitridation under ETEM was done by Hongling Lott at Brookhaven National Lab (BNL) with the guidance and help of Dr. Dmitri Zakharov.

In Chapter 3, tapping mode atomic force microscopy (AFM) was used to study surface morphologies and was collected by Dr. Sunyeol Jeon using Bruker Dimension Icon AFM in

Electron Microbeam Analysis Laboratory (EMAL)* at the University of Michigan. The details of AFM are explained in Section 2.4. Density functional theory (DFT) was used to study the surface diffusion paths and diffusion barriers of adatoms (Ga and N) on Si(001), Si(111), and silica surfaces, as well as the adsorption energy of Ga on substrate surfaces with high and low nitrogen and oxygen coverage. The method is described in Appendix B and the details are included in Appendix B. The CASTEP (CAmbridge Serial Total Energy Package), the DFT module of Materials Studio, was provided by Professor Liangliang Li at the School of Materials Science and Engineering, Tsinghua University, Beijing, China. The DFT calculation of the diffusion barrier was performed by Dr. Yaming Fan, and the DFT calculation of Ga surface adsorption was performed by Dr. Aditya Sundar from Prof. Liang Qi's group.

In Chapter 4, conventional TEM was used to examine nanostructures. Details of conventional TEM are described in Section 2.6.3. Here "conventional TEM" is used to distinguish it from ETEM. The conventional TEM imaging was done by Abby Liu from Prof. Rachel Goldman's group. Software MountainsSPIP® and ImageJ were used for size analysis, and the process is described in Appendix C. Fast Fourier transform (FFT) was used to estimate lattice spacings in conventional TEM images. The process is described in C.3.

In Chapter 5, scanning electron microscopy (SEM) was used to study the nanostructures of the GaN QDs; the details are explained in Section 2.4.2. X-ray diffraction (XRD) and Grazing Incident X-ray diffraction (GIXRD) were used to study polytypes of GaN. Details of XRD and GIXRD are explained in Section 2.4.3. The SEM and XRD were collected by Dr. Sunyeol Jeon using FEI Nova 200 Nanolab dual-beam SEM and 12 kW Rigaku rotating anode source in the

* In 2015, after a successful move from the basement of the Space Research Building (SRB) to the North Campus Research Complex (NCRC), the Electron Microbeam Analysis Laboratory (EMAL) is being renamed the Michigan Center for Materials Characterization, or MC^2.

Electron Microbeam Analysis Laboratory (EMAL) at the University of Michigan. Low temperature photoluminescence (PL) was used to study the optical properties and band-offset between WZ and ZB. The PL measurements for the GaN nanostructures were performed by Dr. Tyler Hill and Dr. Adam Katcher in Prof. Hui Deng's research group; details are described in Section 2.5.

2.2 Molecular beam epitaxy

2.2.1 Group III sources

Molecular beam epitaxy (MBE) is a vapor deposition technique that enables growth of high-quality epitaxial films and heterostructures.[1,2,3,4] The GaN nanostructure samples discussed in this thesis were grown in a Modified Varian Gen II MBE system. This system, as illustrated in Figure 2.1, consists of separately pumped load-lock, buffer, and growth chambers connected by magnetic transfer rods and trolleys. The growth chamber source flange houses seven solid sources (Ga, In, Al, Si, Be, Bi, and As cracker) and N plasma source, and the source materials are contained in pyrolytic boron nitride (PBN) crucibles located in Knudsen effusion cells (K-cell). The molecular beam flux is exponentially dependent on the temperature of the effusion cell controlled by heating the filaments surrounding the PBN crucible. The effusion cell temperature is monitored by a thermocouple in contact with the crucible, and the beam flux is measured by an ionization gauge sitting at the growth position. All samples discussed in this dissertation were grown with azimuthal rotation of 10 rpm. The MBE systems are equipped with high-purity gallium (99.99999%) and indium (99.99999%) contained in pyrolytic boron nitride crucibles, housed in K-cell. The exposure of each molecular beam is controlled by computer-controlled pneumatic shutters.

2.2.2 Radio frequency plasma sources

The GaN samples studied in this thesis were grown using a Veeco RF-N 450 radio frequency (RF) nitrogen plasma source, which generates a reactive N plasma from high-purity N_2 gas (99.9999%). N_2 gas is filtered by an Entegris 0.003 μm purifier prior to entering the plasma source, and the flow rate is regulated by an MKS mass flow controller (MFC). The plasma source is pumped by a Varian Turbo-V 70LP turbomolecular pump and is separated from the growth chamber by a gate valve, which remains closed except during N deposition. The partial pressure of active N in the growth chamber was monitored using residual gas analyzer (RGA) detection of 14 amu particles. To reproducibly control the N flux during GaN nanostructure growths, we struck the plasma and then monitored the partial pressure of 14 amu (active N) in the chamber with a residual gas analyzer (RGA).

For the Veeco RF-N 450 RF plasma source, a one-step ignition process is used. The MFC is set to 0.5sccm and the RF forward power is raised to 450-500W, while the reflected power is minimized, and the plasma is ignited with a bright purple glow. The GaN QDs and NWs studied in Chapter 3 and Chapter 5 were grown with above mentioned Veeco RF-N 450 RF nitrogen plasma source. However, following the growth of samples studied in Chapter 3 and Chapter 5, the Veeco source was accidentally powered without water cooling, rendering it non-functional. Subsequently, the water flow safety interlock was re-installed, and a “spare” Addon RF plasma source, originally intended to be installed on the Riber 32 MBE, was installed on the Gen II. Since the Addon source was designed for dilute nitride materials, lower N flow rates are used, and the ignition process is quite a bit different than that of the Veeco plasma source. In both cases, it is best to perform the ignition process in pairs, with one person adjusting the plasma power and MFC flow rate, and one person monitoring the plasma color and minimizing the reflected power. The usage of the new plasma sources is described in Appendix A.

2.2.3 Reflection high-energy electron diffraction

The MBE growth chamber contains a STAIB electron source which operates at accelerating voltages of 18 keV for in-situ reflection high-energy electron diffraction (RHEED) and a Stanford Research Systems residual gas analyzer (RGA) for in-situ mass spectrometry. Reflection high-energy electron diffraction (RHEED) provides in-situ information about the morphology and atomic structure of the sample surface. For RHEED measurements, an electron beam is accelerated toward the sample surface at a grazing incidence angle (~ 1°). Electrons diffracted from the sample surface form a diffraction pattern on a phosphor screen; this pattern is then captured by a charge coupled device (CCD) camera. The Gen II MBE is equipped with an IMI-Tech IMB-1040FT camera.

Prior to growth, the temperature of each sample was calibrated using the oxide desorption temperature. The oxide desorption temperature was defined as the temperature at which the RHEED pattern transformed from a diffuse 1 × 1 to a streaky 2 × 1 (7 × 7) pattern for Si (001) (Si (111)) surfaces. The substrate temperature (T_s) was increased to the point where a streaky 2 × 1 or 7 × 7 RHEED pattern is observed, considered to be the surface oxide desorption temperature 880 ºC. Once we found the thermocouple temperature corresponding to T_s = 880ºC, the substrate temperature was raised by an additional 20 °C for 10 minutes to ensure complete desorption of surface oxide. For some of the Si (001) samples, oxide desorption steps were omitted, leaving a native oxide layer on the surfaces.

2.3 Sample growths

2.3.1 GaN QDs growths

For the GaN QD arrays studied in Chapter 3, Si(001) and Si(111) substrates were etched in a 5% HF solution for 1 min, followed by insertion into the load-lock chamber within 30 min.

Following UHV transfer into the MBE, the Si substrates were high temperature annealed (substrate temperature of 900 °C) for 10 min to desorb native oxides. For selected Si(001) substrates, the high temperature annealing step was omitted in order to achieve a native oxide surface. Next, with the substrate temperature set to 550 °C, the substrate was exposed to a N flux of 1.0×10^{-6} Torr for 10 min, the "initial" nitridation step, which provides surface SiN_x. To form droplets, an equivalent Ga thickness of 7.5 ML was deposited at a rate of 0.75 ML/s. Since 1 ML Ga is defined as the quantity needed for the formation of one ML of GaN, this corresponds to a 2 nm equivalent GaN thickness. For the "final" nitridation step, the N shutter was opened, while the Ga shutter was simultaneously closed. Meanwhile, the substrate temperature was either held constant at 550 °C ("fixed") or increased at 50 °C/min to 650 °C ("moderate") or 720 °C ("high"), with the duration of temperature ramping less than 4 min. During the final nitridation, each sample was exposed to a N flux of 1.0×10^{-6} Torr for 30 min, similar to earlier studies.[15] For all growths, the RF-plasma source power and N_2 flow rate were fixed at 350 W and 1.0 sccm, respectively, yielding a N flux of 1.0×10^{-6} Torr [as determined by the partial pressure of 14 amu using a residual gas analyzer (RGA)]. The 1 sccm flow rate corresponds to the maximum flux available for our N source configuration (i.e., the Veeco RF-N 450 RF).

2.3.2 In droplet array deposition

For the In droplet arrays on silicon studied in Chapter 4, samples were prepared using MBE, with a V/III beam-equivalent pressure of 1.0×10^{-7} Torr and a growth rate of 0.1 ML/s. The indium droplet arrays were deposited onto SiMPore single crystal pure Si(001) film TEM grids [with window size 50 um, film thickness 35 nm and frame thickness 100 nm] that were indium bonded on 375 nm Si(001) substrates, as illustrated in Figure 2.4. Prior to indium exposure at 100°C, the Si TEM grids on Si(001) substrates were deoxidized in UHV at 940°C. A series of In NP arrays

were prepared via In exposure for 30, 40, 50, 65, and 80 seconds, yielding 3.0, 4.0, 5.0, 6.5, and 8.0 equivalent MLs of In, as listed in Table E.6. Throughout the growth process, the surface reconstruction was monitored in-situ with an 18 keV RHEED source. Following fabrication, the surface morphology of the In exposure series was examined using AFM. To identify the NPs and quantify their size distributions, we used the Scanning Probe Image Processor (SPIP™) software from Image Metrology.[†] In particular, the gradient and advanced threshold methods (as described in Appendix C.3.2.3) were used to detect NP edges.

2.3.3 GaN NWs Growths

For the GaN NWs studied in Chapter 5, Si (001) substrates were used. In preparation for epitaxy, silicon substrates were etched in a 5% HF solution for 30–60 s, mounted on In-free blocks, and pre-baked at 150°C for 8 hours in the load-lock. Each substrate was then transferred into the MBE growth chamber, and the substrate temperature was increased until the RHEED pattern transformed from a diffuse (1 × 1) to a streaky (2 × 1) pattern, considered to be the surface oxide desorption temperature, 880 ºC. During oxide desorption, Ga pre-deposition, and nitridation, RHEED patterns were collected using a RH30 Staib RHEED source operating at 18 kV. To ensure complete desorption of the surface oxide, the substrate temperature was then raised an additional 20 °C, as determined by the thermocouple at the back of the substrate. Following oxide desorption, Ga surface saturation in the absence of N ("Ga pre-deposition") was achieved using Ga beam-equivalent-pressure (BEP) in the range of 1.0×10^{-8} to 1.5×10^{-7} Torr for 3 min. For the Ga pre-deposition step (Ga surface saturation in the absence of N), the gate valve of the N plasma source

[†] Image Metrology is a subsidiary company of Digital Surf. Image Metrology is as the - creator of SPIP™ or the "Scanning Probe Image Processor". MountainsSPIP® was released in July 2019, based on the industry-standard Mountains® platform and SPIP™ interactivity and analytical tools. After January 2020 SPIP™ is no longer being marketed. (https://www.imagemet.com/)

was closed. Continued Ga surface saturation in the presence of N ("nitridation") was then performed. For the nitridation step (Ga surface saturation in the presence of N), the N_2 flow rate/plasma power were held at 1.0 sccm/350 W for 3 hours, resulting in a N flux of 1.0×10^{-6} Torr, as determined by the partial pressure of 14 amu with a residual gas analyzer. For both steps, the substrate temperature was fixed in the range of 780 to 860°C.

We define three flux series, based on the Ga fluxes used in Ga pre-deposition step and nitridation step, namely "low-low", "high-high", and "high-low". For the "low-low" series, Ga pre-deposition was achieved using a "low" Ga BEP of 3.0×10^{-8} Torr, followed by GaN growth with the same Ga BEP. For the "high-high" series, Ga pre-deposition was achieved using a "high" Ga BEP of 9.0×10^{-8} Torr, followed by GaN growth with the same Ga BEP. For the "high-low" series, Ga pre-deposition was achieved using a "high" Ga BEP of 9×10^{-8} Torr, followed by GaN growth with "low" Ga BEP of 3×10^{-8} Torr.

2.4 Characterization methods

2.4.1 Atomic force microscopy

The surface morphology of the GaN QDs in Chapter 3 was investigated using tapping mode AFM with Bruker Dimension Icon AFM at EMAL at the University of Michigan. Etched silicon Nanoscience AFM probes with tip radius <10 nm, length = 125 μm, resonance frequency = 300 kHz, and spring constant = 40 N/m were used for imaging. The AFM scanning head consists of a piezoelectric tube scanner. Piezoelectric scanners are made from piezoelectric material, which expands and contracts proportionally to an applied voltage. The scanner is constructed by combining independently operated piezo electrodes for X, Y, and Z into a single tube, forming a scanner which can manipulate samples and probes with extreme precision in three dimensions.[5] The z-motion is achieved by expanding or contracting the piezoelectric tube with an applied

voltage to the z-electrode. Similarly, the x- and y- motion of the AFM tip is achieved by applying a voltage to the x- and y- electrodes to enable the bending of the piezoelectric tube in the x- and y-directions, respectively. Figure 2.2 shows a schematic of (a) straight and (b) bended piezoelectric tubes during AFM tip scanning on a flat surface. The bending of the piezoelectric tube results in an offset of the laser reflection on the photodiode. The offset of the laser reflection usually leads to a curvature distortion in the output morphology (a.k.a. "bowing") from the scanning surface, which is more significant for larger area scanning.[6] To correct the bowing in the AFM images, all as-collected AFM images were flattened by subtracting a quadratic background in the lateral directions using software SPIP and Image J.

2.4.2 Scanning electron microscopy

For SEM, a focused beam of accelerated electrons is scanned across the surface of a sample. The collision between the accelerated electron probe and the surface of the sample results mainly in (1) the emission of secondary (SE) electrons from the excitation of the atoms in the sample, (2) the backscatter of probe electrons (BSE) from their interaction with the positive nuclei in the sample, and (3) the emission of X-rays, from the excitation and subsequent relaxation of core electrons within the sample. FEI Nova 200 Nanolab dual-beam scanning electron microscopy (SEM) system was used to image GaN nanostructures. Both plan-view and side-view SEM were used to image the surfaces and cross-sections. Typical SEM imaging conditions involved 10 keV electrons with a beam current of 98 pA. The working distance from the electron beam column to sample surfaces was fixed at to be 5 mm.

2.4.3 X-ray diffraction and grazing incident X-ray diffraction

The crystallinity of GaN nanostructures was determined using X-ray diffraction (XRD), conducted with a 12 kW Rigaku Rotating Anode (Cu k_α target λ = 0.1542 nm and graphite

monochromator). Prior to GaN nanostructure samples, a Si (001) sample was measured to ensure that the equipment was aligned. For θ/2θ scans, a sample is rotated by an angle θ, while the detector is rotated by an angle 2θ. The X-ray source was operated at 40 kV and 100 mA. Additionally, to determine the depth of the ZB to WZ polytype transition, we used grazing incidence X-ray diffraction (GIXRD). In this measurement mode, the angle between the source and sample surface was kept fixed at an incident angle (θ_i) ranging from 1 to 8°.[7] In GIXRD, the X-ray source was operating at 30 kV and 10 mA to avoid damage on the detector. For both θ/2θ scans and GIXRD scans, the measurements were performed with a scan step of 0.01 degree and scan rate of 1 deg/min. The refraction-corrected information depth as a function of θ_i is described in (Equation 2.1) and (Equation *2.2*) and presented in Figure 2.3, where μ is GaN linear absorption coefficient at 0.154 nm.[8]

$$\text{Information depth (nm)} = \frac{1}{\mu k_{\theta_i}} + \frac{t}{1 - \exp\left(\mu \times \text{thickness} \times k_{\theta_i}\right)} \quad \text{(Equation 2.1)}$$

$$k_{\theta_i} = \frac{1}{\sin(\theta_i)} + \frac{1}{\sin(2\theta - \theta_i)} \quad \text{(Equation 2.2)}$$

Post 2017 as described in Section 5.5, XRD was conducted with Rigaku SmartLab, using Cu $K_{\alpha 1}$ radiation from a Cu anode and a scintillation counter detector. The anode of Rigaku SmartLab was operated at 40 kV and 44mA. The X-ray was monochromatized with a Ge(220)×2 monochromator and focused with parallel-beam configuration optics. For XRD scans described in Section 5.5, a step size of 2 arcsec (0.0005°, 1 sec integration time) was used. Scan ranges from 32.9°–33.0°, 33.6°–34.7°, 36.7°–37.2°, and 39.8°–40.3° were used to verify the presence of WZ($10\bar{1}0$), WZ(0002), WZ($10\bar{1}1$), and ZB(200), respectively.

2.5 Photoluminescence

To determine the optical properties of the NWs and films, low-temperature photoluminescence (PL) spectroscopy was performed by exciting the samples mounted in a continuous-flow cryostat operating at 10 K. The excitation laser at 267 nm was obtained by third harmonic generation using a pulsed Ti:Sapphire laser at 800 nm. The laser light (1 mW power) was focused to a 60 μm diameter spot, with scattered light from the excitation laser removed using spectral filters. Finally, the PL emission was collected using a 0.6 NA objective lens, dispersed with a monochromator, and detected using a streak camera in focus mode.

2.6 Conventional and in-situ environmental transmission electron microscopy

The Michigan Ion Beam Lab located at the author's home institution, University of Michigan, is equipped with 300 kV FEI Tecnai TEM, which is equipped with DENSsolutions micro-electromechanical systems (MEMS) heating holder that is capable of raising sample temperature from room temperature to 1000 ± 30 ℃. However, this TEM cannot accommodate in-situ imaging during exposure of gaseous sources. To overcome this limitation, the nitridation of In nanoparticles (Chapter 4) was observed using the environmental transmission electron microscopy (ETEM) at Brookhaven National Lab (BNL).

2.6.1 FEI Titan 80-300 environmental transmission electron microscope

The FEI Titan 80-300 TEM at BNL was used for In droplet study in Chapter 4. This ETEM is a high-resolution TEM equipped with a field emission gun and a corrector for spherical aberration of the imaging lens system, capable of delivering a spatial resolution of 0.08 nm at 300 kV and a gas manifold to control the pressure of various gases in sample area.[9] The instrument allows introduction of gaseous environments up to 20 mbars for selected gases. A mass-flow controlled reaction system capable of providing controlled pressures of gas mixtures allows careful

control over reactions and functionality for understanding nanoparticle formation process. The instrument uses a Gatan K2® IS high speed direct detection camera for high frame rate video acquisition.[10] The nitridation process was captured at 400 frames per second (fps). A double-tilt furnace holder was used for all ETEM studies in this thesis.

Electron energy loss spectroscopy (EELS) instrumentation is also incorporated into Titan 80-300 TEM. To understand the composition of the nanoparticles observed in ETEM, we also performed EELS in ETEM. The electrons can interact either elastically (no energy exchange) or inelastically with the sample, and it is these interactions that EELS exploits to extract information about the sample. EELS data typically consists of energy loss spectral information from the sample.

2.6.2 Nitridation In droplets in ETEM

For the nitridation experiment studied in this thesis, In NP arrays prepared via In exposure for 80 seconds yielding 8.0 equivalent monolayers (MLs) of In were used. In NP arrays via In exposure for 30, 40, 50, 65, and 80 seconds yielding 3.0, 4.0, 5.0, and 6.5 equivalent MLs of In were also prepared but have not been nitridated. Following the studies in Chapter 4, further nitridation experiments in ETEM can be performed on different samples with different In equivalent MLs. Nitridation of In droplets was achieved using 0.5 Torr pressure of ammonia. The purity of ammonia is >99.5% with ammonium hydroxide <0.5%. There are no filters in the gas lines to filter out oxygen. Sample was first heated to 400°C from room temperature (25°C) at a ramp rate of 100°C/min. After reaching 400°C, ammonia was introduced. With a ramp rate of 5°C/min, temperature was increased to and then maintained at 550°C. The temperature profile is plotted in Figure 2.5. Digital videos and images were acquired with a Gatan K2® IS high speed direct detection camera. Gatan Microscopy Suite (GMS) Software, also known as

"DigitalMicrograph (DM)" with a license with "In-situ Player" feature ("IS Cameras" or "K2 IS") is required to view in-situ video captures.

2.6.3 Conventional transmission electron microscopy

To obtain further insight into the epitaxial relationship between QDs and substrate, the TEM sample was further investigated under 300 kV FEI Tecnai TEM at Michigan Ion Beam Lab. A zirconated tungsten thermal emission tip was used as filament. An electron beam current of 60 μA and eccentric height of 0.049 μA were used. TEM images of plan-view samples with magnifications in the range of 81 (to image the entire TEM grid) to 620,000 (with atomic spacing) were taken at different locations of the same sample.

2.7 Figures

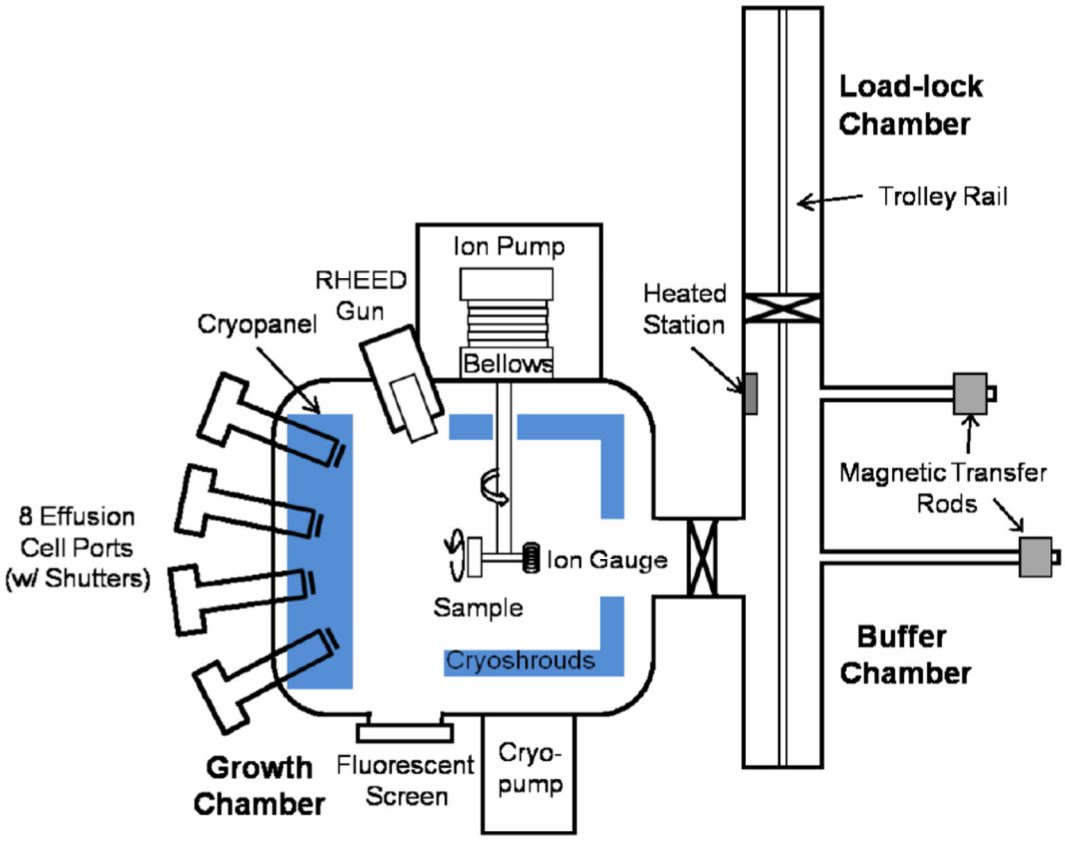

Figure 2.1 Schematic (top-down view) of the Modified Varian Gen II molecular beam epitaxy system used in this thesis study. Ga, Al, In, Si, Be, Bi and As solid sources, and rf N_2 plasma source are located in the effusion cell ports. Reprinted figure with permission from Simon Huang Ph.D. thesis, University of Michigan, Ch.2, 2015.[11]

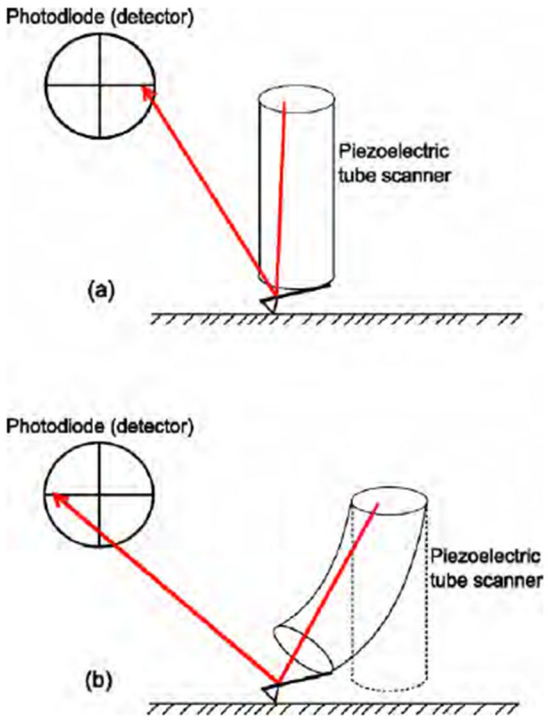

Figure 2.2 Schematic representation of the operation of the AFM scanning tube. The laser light is represented by the red arrowed line. The photodiode, as depicted, is composed of four separate quadrants. The deflection of the tube scanner is exaggerated to better show the deflection of the laser light. Reprinted figure with permission from Simon Huang Ph.D. thesis, University of Michigan, Ch.2, 2015.[11]

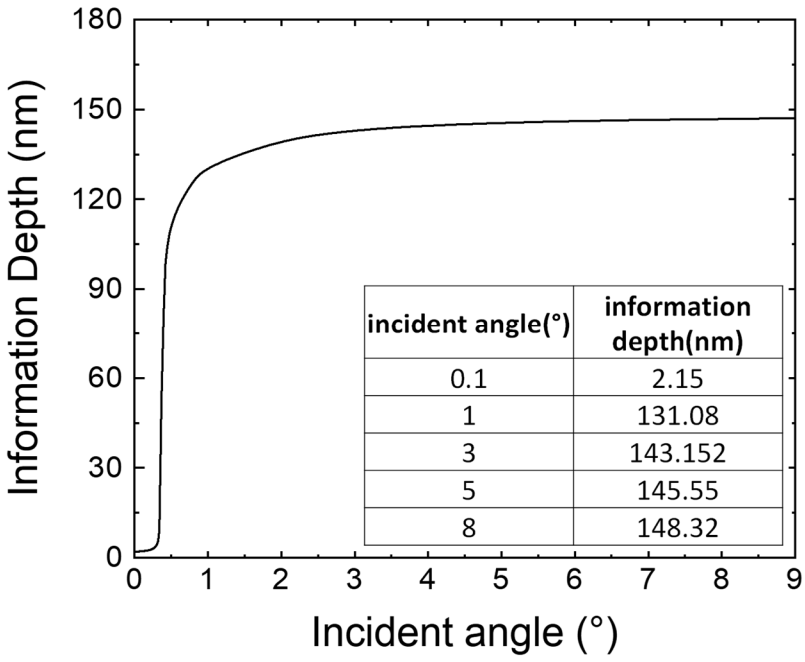

Figure 2.3 Information depth vs. angle of incidence for 0.154 nm X-rays incident upon GaN. Reprinted figure with permission from supplemental materials of Ref 12 (Copyright 2021, AIP Publishing).

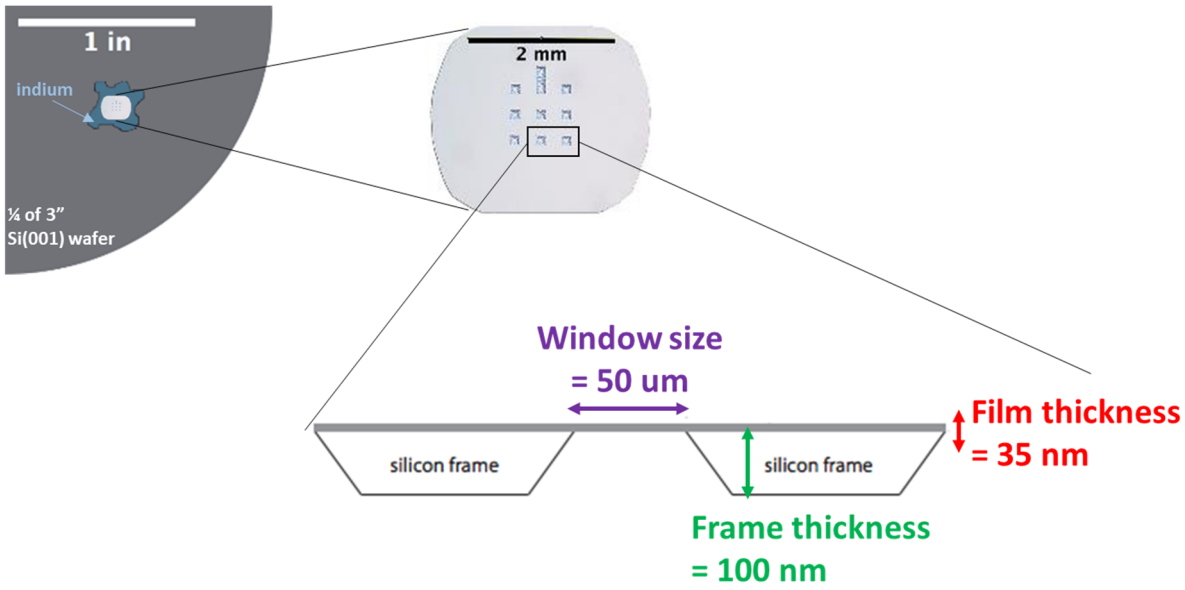

Figure 2.4 Illustration showing sample preparation of single crystal pure Si(001) film TEM grids with window size 50 um, film thickness 35 nm, and frame thickness 100 nm mounted on ¼ of 3” Si(001) wafer using indium.

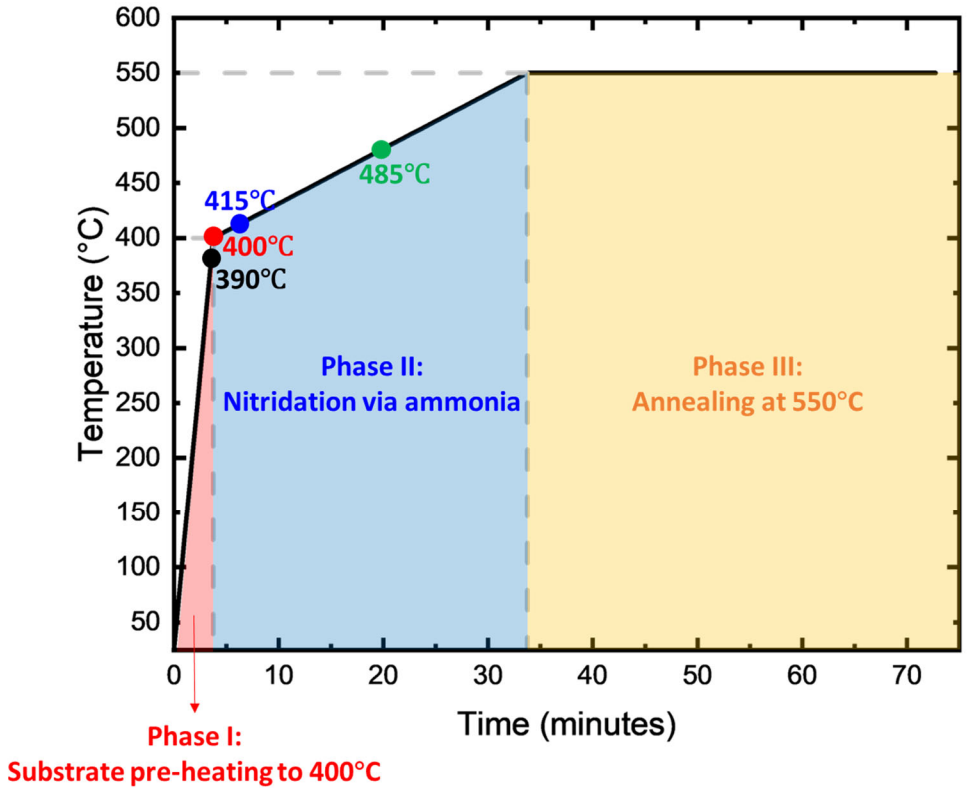

Figure 2.5 Temperature profile of the sample heater during nitridation of ETEM. The sample was first heated to 400°C from room temperature (25°C) at a ramp rate of 100°C/min (Phase I). After reaching 400°C, ammonia was introduced (Phase II). With a ramp rate of 5°C/min, temperature was increased to and then maintained at 550°C (Phase III). The four points labeled in the plot (390°C, 400°C, 415°C, and 485°C) correspond to the temperatures for each size distribution plot in Figure 4.1.

2.8 References

[1] J.R. Arthur, "Interaction of Ga and As2 Molecular Beams with GaAs Surfaces", J. Appl. Phys, 39, 4032 (1968).

[2] A.Y. Cho, "Growth of Periodic Structures By Molecular-Beam Method", Appl. Phys. Lett. 19, 467 (1971).

[3] R.L. Field III, Ph.D. Thesis, "Growth and Electronic Properties of GaAsN and GaAsBi Alloys", University of Michigan, pp. 54, 107–108, 117 (2015).

[4] M.A. Herman, W. Richter, and H. Sitter, "*Epitaxy Physical Principles and Technical Implementation*", (Springer, 2004).

[5] Scanning Probe Microscope Training Book (Rev. E), Copyright © 2003 Bruker, p.p 14 (2003)

[6] R. Howland and L. Benatar, *A Practical Guide: To Scanning Probe Microscopy.* (Park scientific instruments, 1996).

[7] M. Birkholz, *Thin Film Analysis by X-Ray Scattering* (WILEY-VCH, Weinheim, 2006), chapter 4, pp. 155–158.

[8] H. Dakhlaoui, "Linear and nonlinear optical absorption coefficients and refractive index changes in GaN/$Al_xGa_{(1-x)}N$ double quantum wells operating at 1.55 μm", J. Appl. Phys. **117**, 135705 (2015).

[9] S. Takeda, Y. Kuwauchi, H. Yoshida, "Environmental transmission electron microscopy for catalyst materials using a spherical aberration corrector", Ultramicroscopy, 151, 178 (2015).

[10] D. Weber, A. Clausen, and R.E. Dunin-Borkowski, *Handbook on Big Data and Machine Learning in the Physical Sciences* (World Scientific, Singapore, 2020), Chapter 5: "Next-Generation Information Technology Systems for Fast Detectors in Electron Microscopy", pp. 83–120.

[11] S. Huang, Ph.D Thesis, "Formation, Structure, and Properties of InAs/GaAs Quantum Dots", University of Michigan, pp. 26 and 28 (2015).

[12] H. Lu, S. Moniri, C. Reese, S. Jeon, A. Katcher, T. Hill, H. Deng, and R.S. Goldman, "Influence of gallium surface saturation on GaN nanowire polytype selection during molecular-beam epitaxy", Appl. Phys. Lett. 119, 031601 (2021).

Chapter 3

Mechanisms of GaN Quantum Dot Formation During Nitridation of Ga Droplets

3.1 Overview

In this chapter, we present the study of formation mechanisms of GaN QDs via annealing of Ga droplets in a nitrogen flux. In this work, we report the morphology and mechanism of GaN QDs formed on silica, Si(001), and Si(111) after an initial nitridation prior to Ga droplet deposition. Background of this study is introduced in Section 3.2. The in-situ observation of the Ga deposition and GaN QDs growth process is described in Section 3.3. The DFT computational results of diffusion barrier of Ga and N adatoms and Ga adsorption energy are reported and discussed in Sections 3.4 and 3.5, respectively. The details and set-up for DFT calculations are described in Appendix B. In Section 3.6, we report and discuss the morphology of GaN QDs on silica, Si(001), and Si(111). Combining the insights from in-situ growth observations, ex-situ morphology studies, and the DFT calculations, we report on two competing mechanisms mediated by Ga surface diffusion, namely, QD formation at or away from pre-existing Ga droplets, on different substrates at different nitridation temperatures in Section 3.7.

3.2 Background: Gallium nitride-based quantum dots

In recent years, quantum dots (QDs) based on gallium nitride (GaN) and its alloys have been demonstrated for a wide variety of device applications, such as solar cells,[1,2] light-emitting diodes,[3,4,5] lasers,[6,7] and single-photon emitters.[8,9] QDs are typically grown epitaxially via a strain-

induced Stranski–Krastanov (S–K) growth mode transition, which leads to a misfit-strain induced polarization in the QDs.[10] On the other hand, the nucleation and conversion of QDs via nitridation of metallic droplets, known as droplet epitaxy (DE), have attracted much attention as misfit-strain-induced-polarization is expected to be minimized. To date, DE of GaN QDs has been demonstrated on a variety of substrates, including 6H-SiC(0001),[11] Si(111),[12,13,14,15,16] AlGaN/6H-SiC(0001),[17] and c-Al2O3,[18] with single electron transistors achieved on AlN/3C-SiC(001).[19] Furthermore, understanding DE is critical for elucidation of the mechanisms for GaN growth under Ga-rich conditions, which are often argued to be a version of liquid-phase epitaxy (LPE).[20] Indeed, during Ga-rich GaN growth, the low solubility of carbon in Ga and the reactivity of oxygen in Ga, with subsequent desorption of GaO at growth temperatures, lead to low carbon[21] and oxygen[22] co-incorporation. Therefore, DE GaN QDs are expected to be superior to those grown by the S–K method.[23]

However, conflicting results have been reported regarding the formation mechanisms of DE GaN QDs. For example, Wang et al.[18] and Gherasimova et al.[24] reported the formation of QDs via a LPE-like process, where GaN crystallizes along the substrate/droplet interface when N supersaturates the liquid Ga. On the other hand, Debnath et al.[13] proposed a surface diffusion-driven mechanism, where Ga diffuses away from the droplets and reacts with N on the surface to form small QDs. Finally, Kawamura et al.[25] proposed a formation mechanism where N diffuses along the surface to the droplet edges, and small QDs nucleate at the periphery. Here, we investigate the formation mechanisms for DE GaN QDs using a combined computational-experimental approach. Our first-principles calculations of activation barriers suggest that N is nearly immobile, while Ga has a relatively high surface diffusivity, independent of the starting surface structure and chemistry. We present the temperature and substrate dependence of the

droplet and QD size distributions and report on two competing mechanisms mediated by Ga surface diffusion, namely, QD formation at or away from pre-existing Ga droplets. We also report the formation of ZB vs. WZ polytype GaN and discuss the relative roles of nucleation and coarsening dominant growth on various substrates. These mechanisms provide an opportunity for tailoring the QD size and polytype distributions for a wide range of III-N semiconductor QDs.

3.3 In-situ observation of GaN QDs on silicon and silica

To determine the surface reconstructions prior to and during growth, reflection high-energy electron diffraction (RHEED) patterns were collected along the [110] direction, as shown in Figure 3.1. For silica surfaces [Figure 3.1 (a)], as the temperature is increased to 550 °C, a streaky 1 × 1 pattern is apparent, suggesting an unreconstructed Si(001) surface with an oxide layer, which we term the "silica" surface. For the Si(001) surface [Figure 3.1 (b)], a 2 × 1 reconstruction appears as the temperature is increased to 900 °C, indicating an oxide-free Si(001) surface. It is interesting to note the presence of weaker satellite streaks surrounding the 10 and $\bar{1}0$ streaks. Similar satellite streaks have been attributed to the presence of two levels of steps with terraces shorter than the RHEED coherence length.[26] Thus, in our case, these satellite streaks may be due to the presence of both monolayer and bilayer height steps induced during oxide desorption.[27] For the Si(111) surface [Figure 3.1 (c)], as the temperature is increased to 900 °C, the appearance of a 7 × 7 reconstruction suggests an oxide-free Si(111) surface.

During the initial nitridation of silica, streaky RHEED patterns [Figure 3.1 (d)] resemble the pattern observed after surface preparation [Figure 3.1 (a)], suggesting incomplete nitrogen surface coverage. During the deposition of Ga, hazy-streaky RHEED patterns, with the underlying streaks corresponding to the 1 × 1 Si(001) [Figure 3.1 (g)], suggest the formation of Ga droplets in lieu of complete Ga surface coverage. During the final nitridation of the silica surface, shown in

Figure 3.1 (j), the RHEED pattern transitions to concentric rings, containing both WZ and ZB GaN reflections, suggesting the conversion of Ga droplets into crystalline GaN with multiple polytypes and/or orientations, resulting from the incomplete N coverage of the SiO_2 layer shown in Figure 3.1 (d).

On silicon surfaces, hazy-streaky RHEED patterns [Figure 3.1 (e) and Figure 3.1 (f)] were observed after initial nitridation, consistent with the formation of a surface layer of amorphous Si_xN_y. During the deposition of Ga, hazy-streaky RHEED patterns, with the underlying streaks corresponding to the 1 × 1 Si(001) [Figure 3.1 (e)] or 7 × 7 Si(111) [Figure 3.1 (f)] surfaces, are apparent, suggesting the formation of Ga droplet ensembles in lieu of complete Ga surface coverage. During the final nitridation of the Si(001) surface, shown in Figure 3.1 (k), a cubic spotty pattern is observed, with reflections corresponding to ZB GaN, suggesting the transformation of Ga droplets to ZB GaN QDs. The formation of ZB QDs is likely due to epitaxial QD growth mediated by the cubic substrate surface.[19] During the final nitridation of the Si(111) surface, shown in Figure 3.1 (l), spotty-ring RHEED patterns corresponding to WZ GaN are observed, indicating the conversion of droplets to WZ GaN QDs. Presumably, the growth of WZ QDs is due to epitaxial QD growth on the hexagonal-like substrate surface.[12,15,18]

3.4 Computed diffusion barrier for Ga and N adatoms

As shown in Figure B.1, Figure B.2, and Figure B.3, the computed diffusion barriers for a Ga adatom on SiO_2(001), Si(001), and Si(111) are 0.32 eV, 0.38 eV, and 0.41 eV, respectively. Since the epitaxy process involves the use of an N-plasma source[28], from which atomic nitrogen and excited molecular nitrogen are produced,[29] we assume the predominance of atomic N, as opposed to molecular N_2 on the surface. Consequently, as shown in as shown in Figure B.4, Figure B.5, and Figure B.6, the computed diffusion barrier for N adatoms on SiO_2(001), Si(001), and

Si(111) are 4.30 eV, 2.64 eV, and 3.44 eV, respectively. The diffusion barriers for Ga and N on silica and silicon surfaces were determined using first-principles calculations with density functional theory (DFT) in the generalized-gradient approximation (GGA), as discussed in Appendix B. In all cases, the activation energy for diffusion (the diffusion barrier) of N is predicted to be significantly higher than that for Ga. On silica surfaces, Ga is expected to rapidly diffuse on silica and silicon surfaces, while N atoms are nearly immobile on all those surfaces. Since k_BT ~ 0.0259 eV when T = 300 K and the pre-exponential factor is on the order of 10^{13} s^{-1}, the jumping frequency of a Ga adatom is expected to be ~ 10^6 s^{-1}, covering a region with ~100×100 nm^2 during a 1-second random walk. On the other hand, the jumping frequency of a N atom on is expected to be ~ 10^{-2} s^{-1} even when the temperature reaches 1000 K. Thus, it is expected that Ga adatoms will diffuse along the surfaces but that N adatoms will be relatively immobile even at the highest growth temperature of 720 °C.

3.5 Computed Ga adsorption on nitrided/oxidized silicon surfaces

According to (Equation 2.1, the calculated adsorption energies of a single Ga atom are +1.25, +1.65, -0.31 and +0.54 eV on (2 × 1) reconstructed Si (001) surface with 1 N atom, 1 O atom, 2 N atoms and 2 O atoms in the supercell, respectively, as illustrated in Figure B.**10**. We note that for surface coverage with 1 N or 1 O atom, E_{ads}^{Ga} is positive (i.e., repulsive), indicating a preference for isolated Ga adatoms on a clean Si surface without chemical bonding to the N or O atom. For higher N surface coverage, E_{ads}^{Ga} is negative (i.e., attractive), indicating that Ga adatoms prefer to bond to N atoms on the Si surface. However, for higher O surface coverage E_{ads}^{Ga} is positive (i.e., repulsive), indicating it is not energetically favorable for Ga adatoms to bond to O atoms on the oxidized surface. Since $E_{ads}^{Ga}(N) < E_{ads}^{Ga}(O)$, the Ga-N interactions are stronger than Ga-O interactions. Such stronger Ga-N interactions can impede the diffusion of Ga on the surface

by pinning Ga atoms to N atoms. Consequently, the lateral Ga diffusivity is expected to be slower on the nitrided than on the oxidized silicon surface. Thus, O-rich regions are expected to provide a pathway for enhanced Ga surface diffusion and nucleation/ripening of GaN quantum dots.

3.6 Morphology of GaN QDs on silicon and silica

For each surface, post-growth AFM images of Ga droplet ensembles and GaN QD ensembles nitrided at fixed, moderate, and high temperatures are presented in Figure 3.2(a)-(d) [silica], Figure 3.3(a)-(d) [Si(001)], and Figure 3.4(a)-(d) [Si(111)]. In addition, the corresponding Ga droplet and GaN QD size distributions are fit with Gaussian and/or log-normal functions, in order to extract the most probable droplet and QD diameters, dm, as shown in Figure 3.2(e), Figure 3.3(e), and Figure 3.4(e).

For all the Ga droplet ensembles, the size distributions are best described (i.e., $R^2 > 0.99$) with a log-normal function, consistent with the expected absence of coarsening during liquid-like droplet formation.[30] For Ga droplet ensembles on silica, Si(001), and Si(111) surfaces, d_m values are 27 ± 3 nm, 47 ± 8 nm, and 47 ± 4 nm, with droplet densities of 1.6×10^{10} cm^{-2}, 3.7×10^{9} cm^{-2}, and 5.3×10^{9} cm^{-2}, respectively. The lower values of droplet d_m and the higher values of droplet densities on the silica surface in comparison to those of the silicon surfaces are likely due to the "patchy" vs complete coverage of Si_xN_y, as shown in Figure 3.5(a),(b),(e), and (f), respectively. Presumably, the limited lateral extent of the Si_xN_y patches on the silica surface inhibits Ga droplet nucleation and coalescence, thereby limiting the size of Ga droplets.

For most surfaces (all except silica with a final nitridation temperature of 720 °C), the QD d_m values decrease, while the QD densities increase in comparison to those of the Ga droplets. As illustrated in Figure 3.5(c), for those cases, the dominant QD formation mechanism is Ga out-diffusion, expected to be well-described by a log-normal distribution. Indeed, for most cases, fits

to a log-normal distribution lead to $R^2 > 0.99$. On silicon surfaces, QD nucleation occurs anywhere along the SiN_x, as shown in Figure 3.5(g).

3.7 Mechanism of GaN QD formation during nitridation of Ga droplets

For silica surfaces, due to the limited Ga surface diffusion length, $\boldsymbol{\lambda_{Ga}}$, out-diffusing Ga atoms cannot reach nearby Ga droplets; instead, they nucleate at SiN_x patches between Ga droplets, as shown in Fig. 5(c). On the other hand, following final nitridation of the silica surface at high temperatures, the QD d_m values increase, while the QD densities decrease in comparison to those of the Ga droplets. As illustrated in Fig. 5(d), in this case, the QD formation mechanism includes coarsening, which is well-described by either a Gaussian or Lorentzian distribution. Indeed, fits to a Gaussian distribution lead to $R^2 > 0.99$, but those of a Lorentzian distribution lead to $R^2 \approx 0.96$. Due to the longer $\boldsymbol{\lambda_{Ga}}$ at high final nitridation temperature, out-diffusing Ga atoms are able to reach other Ga droplets, resulting in droplet coarsening, as shown in Figure 3.5(d).

To understand the enhanced Ga surface diffusion on silica surfaces, we consider DFT computed Ga adsorption energies on nitrided and oxidized Si surfaces, as described in Appendix B. Due to the negative values of adsorption energies for Ga on nitrided Si surfaces, surface N is likely to inhibit the diffusion of Ga atoms. On the other hand, for silica surfaces, the initial nitridation leads to incomplete nitrogen surface coverage. Instead, due to the positive values of adsorption energies for Ga on oxidized silicon surfaces, the regions with oxygen may serve as a fast diffusion path for Ga adatoms, thereby facilitating coarsening.

For Si(111) at moderate and Si(001) at high final nitridation temperatures, bimodal QD size distributions are observed. In addition, several of the QDs formed at the highest nitridation temperature exhibit a ring-shaped cluster morphology, as indicated by the arrows in Fig. 3(d) and by the inset in Fig. 4(d). Thus, it is likely that N incorporation, followed by QD nucleation, occurs

at the periphery of the largest Ga droplets.[25] Similar morphologies have been reported in other III–V material systems, such as GaAs/GaAs[31,32] and InGaAs/GaAs,[33] where ring formation is attributed to simultaneous out-diffusion of Ga from the droplet center and arsenic crystallization at the edges. The observation of the ring-morphology with smaller individual QDs, as well as the appearance of a multi-modal QD distribution, as discussed above, suggests that Ga adatoms diffusing outward from the droplet center are able to nucleate as smaller QDs elsewhere on the surface.

Finally, on Si(111) surfaces, for the fixed final nitridation temperature, ~1.5 nm height macrosteps are apparent, as illustrated by the line-cut shown in the inset to the AFM image in Fig. 4(b). Interestingly, QDs are preferentially located at the edges of the macrosteps, consistent with nucleation of both Si_3N_4 and QDs in regions of positive curvature.[34,35]

3.8 Conclusion

In summary, we have examined the formation mechanisms of GaN quantum dots during nitridation of Ga droplets. We consider the temperature- and substrate-dependence of the size distributions of droplets and QDs, as well as the relative roles of Ga/N diffusivity and GaN nucleation rates on QD formation. We report on the selection of ZB GaN QDs on Si(001), WZ GaN QDs on Si(111), and mixed ZB/WZ GaN QDs on silica surfaces. We also report on two competing mechanisms mediated by Ga surface diffusion, namely, QD formation at or away from pre-existing Ga droplets. On silica surfaces, coarsening-dominant growth leads to coalescence of Ga droplets and, consequently, larger hemispherically-shaped QDs at high nitridation temperature. At low temperature, due to the limited Ga diffusion length, QDs form between Ga droplets. On Si(001) and Si(111) surfaces, nucleation-dominant growth leads to smaller QDs as GaN QDs can

nucleate anywhere on the surface. These insights provide an opportunity for tailoring QD size distributions and polytype selection for a wide range of III-N semiconductor QDs.

3.9 Figures

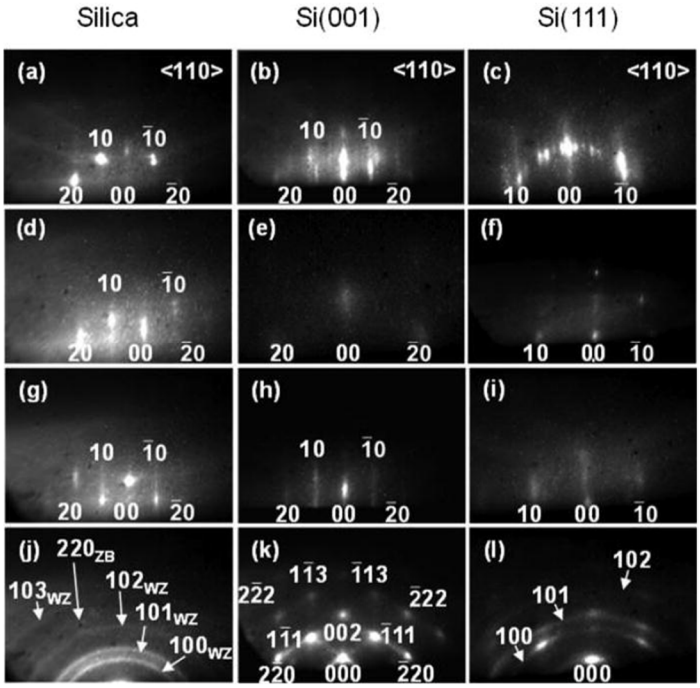

Figure 3.1 Reflection high-energy electron diffraction (RHEED) patterns collected along the [110] axis for silica [(a), (d), (g), and (j)], Si(001) [(b), (e), (h), and (k)], and Si(111) [(c), (f), (i), and (l)] surfaces. In the first row, following surface preparation, streaky patterns corresponding to diffraction from the (a) silica, (b) Si(001), and (c) Si(111) surfaces are apparent. In the second row, during the first nitridation step, streaky patterns on (d) silica reveal incomplete nitrogen surface coverage. Diffuse patterns on (e) Si(001) and (f) Si(111) indicate the formation of an amorphous layer of Si_xN_y. In the third row, during Ga deposition, the RHEED patterns on (g) silica, (h) Si(001), and (i) Si(111) reveal the formation of Ga droplets. In the fourth row, during the final nitridation step, the RHEED patterns reveal transitions to (j) polycrystalline GaN on silica, (k) zincblende GaN on Si(001), and (l) wurtzite GaN on Si(111). Reprinted figure with permission from Ref 36 (Copyright 2020, AIP Publishing).

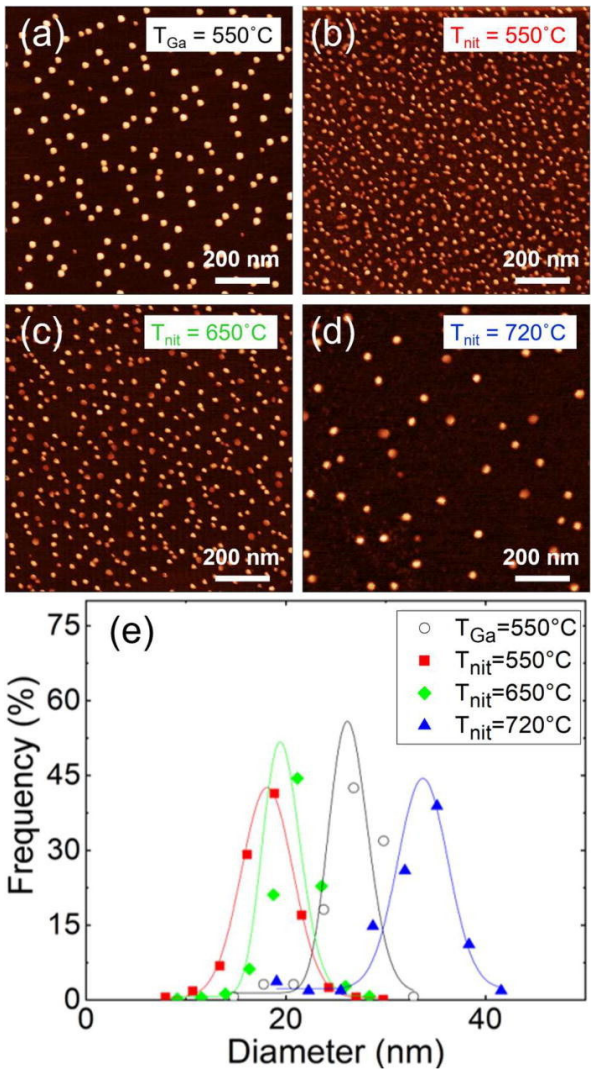

Figure 3.2 Atomic-force microscopy (AFM) images of the Ga droplet and GaN QD ensembles grown on silica: (a) Ga deposition at 550 °C, followed by final nitridation at (b) 550 °C, (c) 650 °C, and (d) 720 °C. The color-scale ranges displayed are (a) 24.8 nm, (b) 17.6 nm, (c) 19.3 nm, and (d) 18.2 nm. The corresponding size distributions from images (a)–(d) are shown in (e), and the frequency is the percentage of QDs with diameters within a specified range. For Ga droplets, the d_m value is 27 ± 3 nm with a density of 1.6×10^{10} cm^{-2}. For GaN QDs with final nitridation at 550, 650, and 720 °C, the d_m values (densities) are 18 ± 3 nm (8.3×10^{10} cm^{-2}), 21 ± 2 nm (4.0×10^{10} cm^{-2}), and 34 ± 4 nm (5.4×10^{9} cm^{-2}) respectively. (a)–(c) are fitted with a log-normal distribution where $R^2 > 0.99$, and (d) is fitted using a Gaussian distribution with $R^2 > 0.99$. Reprinted figure with permission from Ref 36 (Copyright 2020, AIP Publishing).

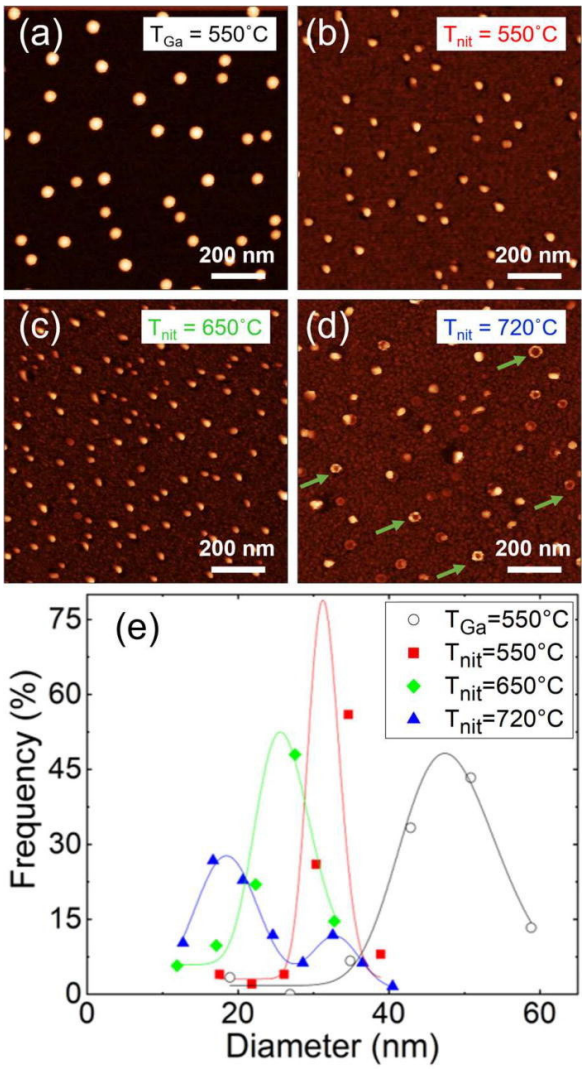

Figure 3.3 Atomic-force microscopy (AFM) images of the Ga droplet and GaN QD ensembles grown on Si(001): (a) Ga deposition at 550 °C, followed by final nitridation at (b) 550 °C, (c) 650 °C, and (d) 720 °C. The color-scale ranges displayed are (a) 32.0 nm, (b) 17.7 nm, (c) 18.0 nm, and (d) 33.8 nm. The corresponding size distributions from images (a)–(d) are shown in (e), and the frequency is the percentage of QDs with diameters within a specified range. For Ga droplets, the dm value is 47 ± 8 nm and the density is 3.7×10^9 cm^{-2}. For GaN QDs with final nitridation at 550, 650, and 720 °C, the dm values (densities) are 31 ± 4 nm (5.0×10^9 cm^{-2}), 26 ± 5 nm (1.2×10^{10} cm^{-2}), and multimodal with 18 ± 8 nm and 33 ± 8 nm (1.7×10^{10} cm^{-2}) respectively. (a)–(d) are fitted using a lognormal distribution with $R^2 > 0.99$. Reprinted figure with permission from Ref 36 (Copyright 2020, AIP Publishing).

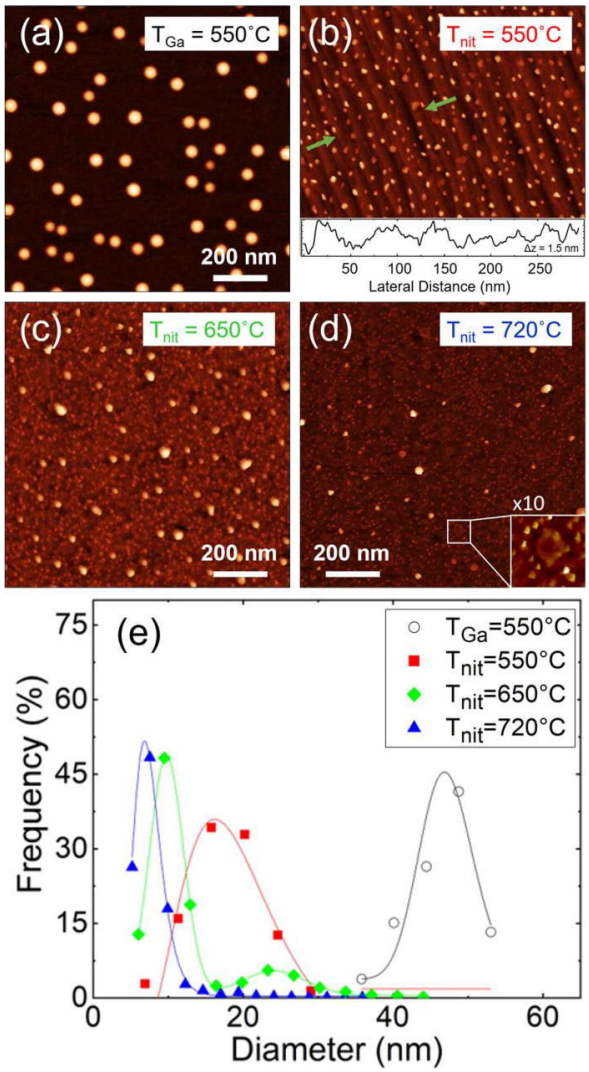

Figure 3.4 Atomic-force microscopy (AFM) images of the Ga droplet and GaN QD ensembles grown on Si(001): (a) Ga deposition at 550 °C, followed by final nitridation at (b) 550 °C, (c) 650 °C, and (d) 720 °C. The color-scale ranges displayed are (a) 32.0 nm, (b) 17.7 nm, (c) 18.0 nm, and (d) 33.8 nm. The corresponding size distributions from images (a)–(d) are shown in (e), and the frequency is the percentage of QDs with diameters within a specified range. For Ga droplets, the dm value is 47 ± 8 nm and the density is 3.7×10^9 cm^{-2}. For GaN QDs with final nitridation at 550, 650, and 720 °C, the dm values (densities) are 31 ± 4 nm (5.0×10^9 cm^{-2}), 26 ± 5 nm (1.2×10^{10} cm^{-2}), and multimodal with 18 ± 8 nm and 33 ± 8 nm (1.7×10^{10} cm^{-2}) respectively. (a)–(d) are fitted using a lognormal distribution with $R^2 > 0.99$. Reprinted figure with permission from Ref 36 (Copyright 2020, AIP Publishing).

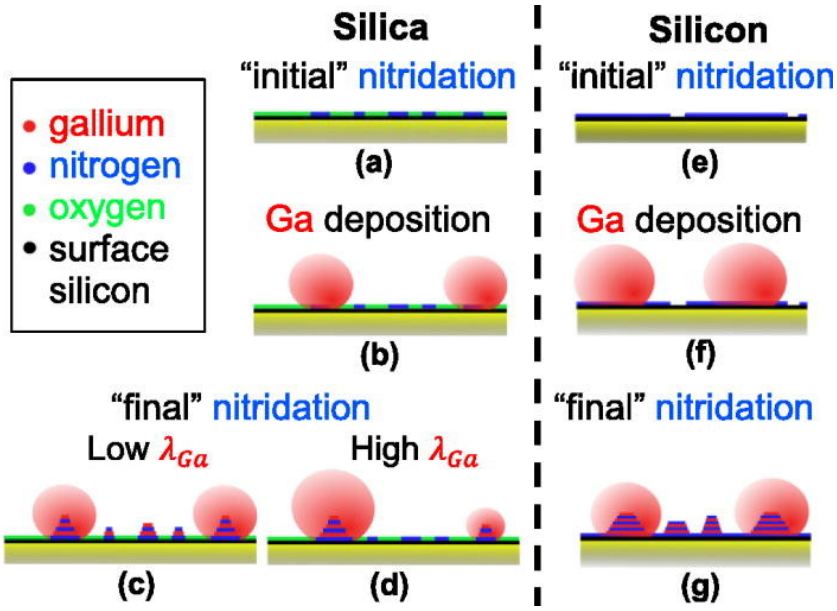

Figure 3.5 Illustrations of QD nucleation and growth mechanisms on silica and silicon surfaces. In both steps are shown: (a) and (e) initial nitridation; (b) and (f) Ga deposition; (c), (d), and (g) final nitridation. On the silica surface, (a) the initial nitridation induces nanoscale surface roughening, which subsequently enables Ga droplet formation during (b) the Ga deposition step. During the final nitridation step, nitrogen impinges upon the droplets, resulting in QD nucleation. When (c) the final nitridation substrate temperature is lower (550 °C and 650 °C), the Ga diffusion length, λ_{Ga}, is much smaller than the Ga droplet separation distance, and Ga out-diffusion leads to QD nucleation in between Ga droplets. When the final nitridation substrate temperature is increased to 720 °C, the Ga diffusion length, λ_{Ga}, is (d) comparable to the Ga droplet separation, and Ga out-diffusion leads to Ga droplet coarsening. On the silicon surfaces, during (e) the initial nitridation step, impinging nitrogen atoms form patches of surface Si_xN_y layers, which act as droplet nucleation sites during (f) the Ga deposition step. During (g) the final nitridation step, nitrogen impinges upon the droplets and the regions of the bare silicon surface, enabling QD nucleation at both Ga droplets and Si_xN_y patches. When the final nitridation substrate temperature is increased, the Ga diffusion length, λ_{Ga}, is comparable to the nucleation site separation, and a bimodal distribution of QD sizes is apparent. Reprinted figure with permission from Ref 36 (Copyright 2020, AIP Publishing).

3.10 References

[1] L. Sang, M. Liao, Q. Liang, M. Takeguchi, B. Dierre, B. Shen, T. Sekiguchi, Y. Koide, and M. Sumiya, "A multilevel intermediate-band solar cell by InGaN/GaN quantum dots with a strain-modulated structure", Adv. Mater. 26, 1414 (2014).

[2] Q. Deng, X. Wang, C. Yang, H. Xiao, C. Wang, H. Yin, Q. Hou, J. Li, Z. Wang, and X. Hou, "Theoretical study on InxGa1−xN/GaN quantum dots solar cell", Physica B 406, 73 (2011).

[3] B. Damilano, N. Grandjean, J. Semond, J. Massies, and M. Leroux, "From visible to white light emission by GaN quantum dots on Si(111) substrate", Appl. Phys. Lett. 75, 962 (1999).

[4] T. Egawa, B. Zhang, and H. Ishikawa, "High performance of InGaN LEDs on (111) silicon substrates grown by MOCVD", IEEE Electron Device Lett. 26, 169 (2005).

[5] M. Zhang, P. Bhattacharya, and W. Guo, "InGaN/GaN self-organized quantum dot green light emitting diodes with reduced efficiency droop", Appl. Phys. Lett. 97, 011103 (2010).

[6] T. Frost, A. Banerjee, K. Sun, S.L. Chuang, and P. Bhattacharya, "Red and Near-Infrared III-Nitride Quantum Dot Lasers", IEEE J. Quantum Electron. 49, 923 (2013).

[7] M. Zhang, A. Banerjee, C.-S. Lee, J.M. Hinckley, and P. Bhattacharya, "A InGaN/GaN quantum dot green (λ=524 nm) laser", Appl. Phys. Lett. 98, 221104 (2011).

[8] S. Kako, C. Santori, K. Hoshino, S. Götzinger, Y. Yamamoto, and Y. Arakawa, "A gallium nitride single-photon source operating at 200 K", Nat. Mater. **5**, 887 (2006).

[9] S. Kremling, C. Tessarek, H. Dartsch, S. Figge, S. Höfling, L. Worschech, C. Kruse, D. Hommel, and A. Forchel, Appl. Phys. Lett. "Single photon emission from InGaN/GaN quantum dots up to 50 K", **100**, 061115 (2012).

[10] E.T. Yu, X.Z. Dang, P.M. Asbeck, S.S. Lau, and G.J. Sullivan, "Spontaneous and piezoelectric polarization effects in III–V nitride heterostructures", J. Vac. Sci. Technol. B 17, 1742 (1999).

[11] C.W. Wu, A. Bell, F.A. Ponce, D.J. Smith, and I.S.T. Tsong, "Growth of self-assembled GaN quantum dots via the vapor–liquid–solid mechanism", Appl. Phys. Lett. 81, 3236 (2002).

[12] T. Kondo, K. Saitoh, Y. Yamamoto, T. Maruyama, and S. Naritsuka, "Fabrication of GaN dot structures on Si substrates by droplet epitaxy", Phys. Status Solidi A 203, 1700 (2006).

[13] R.K. Debnath, T. Stoica, A. Besmehn, K. Jeganathan, E. Sutter, R. Meijers, H. Lüth, and R. Calarco, "Formation of GaN nanodots on Si (1 1 1) by droplet nitridation", J. Cryst. Growth 311, 3389 (2009).

[14] Y.-Z. Su and I.-S. Yu, "Crystal Structures of GaN Nanodots by Nitrogen Plasma Treatment on Ga Metal Droplets", Metals 8, 419 (2018).

[15] S. Naritsuka, T. Kondo, H. Otsubo, K. Saitoh, Y. Yamamoto, and T. Maruyama, "In situ annealing of GaN dot structures grown by droplet epitaxy on (1 1 1) Si substrates", J. Cryst. Growth 300, 118 (2007).

[16] H. Otsubo, T. Kondo, Y. Yamamoto, T. Maruyama, and S. Naritsuka, "Effect of substrate surface on GaN dot structure grown on Si(111) by droplet epitaxy", Phys. Status Solidi C 4, 2322 (2007).

[17] K. Kawasaki, D. Yamazaki, A. Kinoshita, H. Hirayama, K. Tsutsui, and Y. Aoyagi, "GaN quantum-dot formation by self-assembling droplet epitaxy and application to single-electron transistors", Appl. Phys. Lett. 79, 2243 (2001).

[18] Y. Wang, A.S. Özcan, C. Sangborn, K.F. Ludwig, A. Bhattacharyya, R. Chandrasekaran, T.D. Moustakas, L. Zhou, and D.J. Smith, "Real-time x-ray studies of gallium nitride nanodot formation by droplet heteroepitaxy", J. Appl. Phys. 102, 073522 (2007).

[19] T. Schupp, T. Meisch, B. Neuschl, M. Feneberg, K. Thonke, K. Lischka, and D.J. As, "Molecular beam epitaxy based growth of cubic GaN quantum dots", Phys. Status Solidi C 8, 1495 (2011).

[20] T.D. Moustakas and A. Bhattacharyya, "(Invited) Experimental Evidence that the Plasma-Assisted MBE Growth of Nitride Alloys is a Liquid Phase Epitaxy Process" ECS Trans. 35, 63 (2011).

[21] T.F. Kuech, *Handbook of Crystal Growth: Thin Films and Epitaxy: Basic Techniques* (Elsevier, Burlington, 2014), p. 281.

[22] T.D. Moustakas and A. Bhattacharyya, "The role of liquid phase epitaxy during growth of AlGaN by MBE", Phys. Status Solidi C 9, 580 (2012).

[23] J. Wu and Z.M. Wang, "Droplet epitaxy for advanced optoelectronic materials and devices", J. Phys. D: Appl. Phys. 47, 173001 (2014).

[24] M. Gherasimova, G. Cui, S.-R. Jeon, Z. Ren, D. Martos, J. Han, Y. He, and A.V. Nurmikko, "Droplet heteroepitaxy of GaN quantum dots by metal-organic chemical vapor deposition", Appl. Phys. Lett. 85, 2346 (2004).

[25] T. Kawamura, H. Hayashi, T. Miki, Y. Suzuki, Y. Kangawa, and K. Kakimoto, "Molecular beam epitaxy growth of GaN under Ga-rich conditions investigated by molecular dynamics simulation", Jpn. J. Appl. Phys. 53, 05FL08 (2014).

[26] S. Hasegawa, in *Characterization of Materials*, edited by E.N. Kaufmann (John Wiley & Sons, NY, 2003), pp. 1925–1938.

[27] Y. Enta, T. Nagai, T. Yoshida, N. Ujiie, and H. Nakazawa, "Decomposition kinetics of silicon oxide layers on silicon substrates during annealing in vacuum", J. Appl. Phys. 114, 114104 (2013).

[28] M.A.L. Johnson, Z. Yu, C. Boney, W.C. Hughes, J.W. Cook, J.F. Schetzina, H. Zhao, B.J. Skromme, and J.A. Edmond, "Reactive MBE Growth of GaN and GaN:H on GaN/SiC Substrates", Mater. Res. Soc. Symp. Proc. 449, 215 (1997).

[29] M. Pérez-Caro, M. Ramírez-López, Sergio, Hernandez-Mendez, B. A., G. Rodríguez, Y. L. Casallas-Moreno, S. Gallardo-Hernández, M. López-López, "Optical studies of nitrogen plasma for molecular beam epitaxy of InN". J. Appl. Phys. 128, 215304 (2020).

[30] R.B. Bergmann and B. Andreas, "On the origin of logarithmic-normal distributions: An analytical derivation, and its application to nucleation and growth processes", J. Cryst. Growth 310, 3135 (2008).

[31] K. Reyes, P. Smereka, D. Nothern, J.M. Millunchick, S. Bietti, C. Somaschini, and S. Sanguinetti, "Unified model of droplet epitaxy for compound semiconductor nanostructures: Experiments and theory", Phys. Rev. B 87, 165406 (2013).

[32] S. Bietti, C. Somaschini, L. Esposito, A. Fedorov, and S. Sanguinetti, "Gallium surface diffusion on GaAs (001) surfaces measured by crystallization dynamics of Ga droplets", J. Appl. Phys. 116, 114311 (2014).

[33] T. Mano, K. Wantanabe, S. Tsukamoto, H. Fujioka, M. Oshima, and N. Koguchi, "Fabrication of InGaAs quantum dots on GaAs(001) by droplet epitaxy", J. Cryst. Growth 209, 504 (2000).

[34] S. Gangopadhyay, T. Schmidt, and J. Falta, "Initial stage of silicon nitride nucleation on Si(111) by rf plasma-assisted growth", e-J. Surf. Sci. Nanotechnol. 4, 84 (2006).

[35] D. DelGaudio, L.K. Aagesen, S. Huang, T.M. Johnson, B.D. Faeth, H. Lu, R.M. Ziff, and R.S. Goldman, "Influence of surface nano-patterning on the placement of InAs quantum dots", J. Appl. Phys. 124, 115307 (2018).

[36] H. Lu, C. Reese, S. Jeon, A. Sundar, Y. Fan, E. Rizzi, Y. Zhuo, L. Qi, and R.S. Goldman, "Mechanisms of GaN quantum dot formation during nitridation of Ga droplets", Appl. Phys. Lett. 116, 062107 (2020).

Chapter 4

Environmental Transmission Electron Microscopy Study of Nitridation of In Droplets

4.1 Overview

In this chapter we present our investigation of environmental transmission electron microscopy (ETEM) studies of nitridation of In droplets. In this work, we report the In droplet deposition via MBE on Si(001) single crystal TEM film and the subsequent nitridation of In droplets in ETEM. The details of the sample preparation and growths are described in Section 2.3.2 and 2.6.2. In ETEM, we observed temperature-dependent size change of the observed nanoparticles, discussed in Section 4.3. Two types of moiré patterns, namely 1D moiré fringes (1D MF) and 2D moiré fringes (2D MF), were observed in ETEM. From the observation of moiré patterns in ETEM and the crystal lattice spacings examined under TEM, we conclude that at lower nitridation temperatures, smaller particles were observed and more of them showed 2D MF related to InN ZB formation. At higher nitridation temperature, larger particles were observed and fewer of them exhibited 2D MF. We hypothesize that there is a higher probability of ZB nucleation from smaller particles and WZ nucleation from larger particles, with unintentional In_2O_3 formation on InN, as discussed in Section 4.4. This observation can provide insight into the transformation of indium nanoparticles into InN. Conclusion and discussion of further suggestions are described in Section 4.5 and Section 7.2.2.

4.2 Background and motivation

InN is a direct band gap semiconductor that belongs to the III−V family and an interesting and potentially important semiconductor material with superior electronic transport properties.[1,2,3] InN has high electron mobility (∼4000−5000 $cm^2/(Vs)$)[4,5] and low electron effective mass (∼0.1 m_{e0}).[6] Therefore, such a material with a narrow band gap has been broadly applied in the fields of high-speed electronic devices, high efficiency solar cells, infrared light emitting diodes, and laser diodes.[7,8] The room temperature bandgap of WZ InN was reported to be 0.7-0.9 eV,[42,9] which makes InN an exciting material for near infrared LED applications. Notably, these reports disagree with older studies that found the bandgap of InN to be 1.7-1.8 eV.[10,11] Bandgap widening in with higher oxygen impurity concentrations has been demonstrated in WZ InN,[12] leading to the hypothesis that older bandgap measurements were higher than modern reports because of oxygen incorporation. Conversely, the bandgap of zinc-blende (ZB) InN is predicted to be 0.58 eV,[13] offering an appealing possibility to further extend the available ranges of low wavelength LED devices.

Recently, semiconductor NPs have received increased interest for enhancing the performance of optoelectronic devices such as photodetectors and thin film solar cells.[14,15,16,17] Unlike metal NPs, semiconductor nanoparticles can absorb higher energy photons and emit photons of lower energy. This downshift property (the ability to emit low energy photons out of high energy photons) of InN make this material advantageous in solar cell performance applications.[18,19,20] In the specific case of InN QDs, the bandgap of WZ InN QDs was shown to increase from 0.67 eV to 0.85 eV as QD diameters decreased from 32 nm to 4.5 nm.[21] Considering the lower bandgap of ZB InN, control over WZ/ZB polytype selection could further expand low energy tunability for light collection and emission by InN QDs. While polytype selection between

WZ and ZB in bulk materials is thermodynamically governed,[22,23] substrate/droplet contact angles,[24,25] surface/interfacial energies,[26] and surface diffusivities[27] are predicted to determine WZ/ZB polytype selection in processes such as QD formation. InN QDs have also been demonstrated to be suitable for plasmonic applications due to their localized surface plasmon resonance across a window covering the mid- and far-infrared.[28]

To date, well-controlled and precisely understood methods for InN QDs fabrication remain a huge challenge. To date, the method of indium droplet formation and nitridation to grow InN nanostructures has been employed to fabricate InN quantum dots on Si(111),[29,30] SiN_x/Si(111),[29,31] AlN/Si(111),[31] Ge(100),[31] rough (rms≈10 nm) $In_{0.3}Ga_{0.7}N$/Si(111),[32] and sapphire.[33] Most of the studies involve a pre-nitridation step prior to indium deposition, resulting in the formation SiNx interlayer between the substrate and polycrystalline InN islands.[32,34,35,36] Furthermore, post DE annealing was required to form single crystal WZ InN QDs. [32] To-date, real-time studies of InN QD formation have not been limited to qualitative RHEED studies.[34]

The formation of indium oxide (In_2O_3) during or after the formation of InN has also been considered. For example, intentional oxidation has been reported for on InN NWs grown on Si(111), where InN/In_2O_3 core/shell structures were formed by rapid thermal oxidation processes[37] and hydrogen plasma treatment.[38] On WZ InN(0001) thin films, cyclic rapid thermal annealing has been used to form In_2O_3(111).[39] Unintentional oxidation of InN has been reported on InN NWs grown by MBE on Si(111) [40] and within InN QDs grown by MBE on p-Si(001) substrates, where it is argued that the In_2O_3 was initiated on the InN surface and advanced inward.[41] Unintentionally oxidized InN QDs from the natural aging process at ambient conditions by oxygen incorporation have also been reported on uncapped InN nanostructures. During such a process, there is a gradual transformation of the InN from its original hexagonal arrangement (WZ) to cubic stacking in stable

In_2O_3 where metastable zinc blende InN domains rich in oxygen.[42] However, these studies of unintentional oxidation of InN often report In_2O_3 following prolonged aging in an ambient environment after the prolonged aging process. In our study of InN droplet epitaxy in ETEM, our observation of the moiré pattern formation during suggested unintentional In_2O_3 formation on InN within ETEM during growth, which has not been reported.

Here, we aim to bridge this gap in the scientific literature by using in-situ ETEM at BNL to develop a detailed fundamental understanding of the nitridation of In droplets during the reaction with ammonia (NH_3). For Si(001) substrate, we employ state-of-the-art single crystal pure Si(001) TEM grid by SiMPore. Such TEM grids can act as robust substrates on which to deposit materials or grow nanoparticles. The In deposition on Si(001) TEM grid is described in Section 2.3.2.

ETEM allows observation of the full nitridation process, providing insight into the NP size change and epitaxial development.[43] Nevertheless, ETEM has not been applied to observe the formation of InN and their mechanisms during growth. In addition to size distributions and evolution during ETEM, we use the moiré pattern observed in ETEM video captures and the lattice spacings observed under conventional TEM to analyze the crystal structures and polytypes within the nanoparticles. Combining the size distributions and crystal/polytype structure analysis, we hypothesize that there is a higher probability of ZB InN nucleation from smaller particles and WZ nucleation from larger particles formed in ETEM through In droplet nitridation. Given that the purity of ammonia used is >99.5% with ammonium hydroxide <0.5% and no filters in the gas lines to filter out oxygen, we also hypothesize that In_2O_3 form on InN formed in ETEM, based on observations of the moiré fringe spacings in ETEM.

4.3 Nanoparticle size evolution in ETEM

To gain insight into the mechanisms for of the nitridation of indium nanoparticles, the evolution of the crystallite sizes with temperature in the ETEM chamber was investigated. For this purpose, the distribution of nanoparticle sizes was quantified using analysis of several frames from in-situ ETEM video captures, such as those shown in Figure 4.7. The crystallite size distribution analysis procedure is described in Appendix C. Figure 4.1 shows the distribution of crystallite sizes, determined from several frames from ETEM video capture, and fit with Gaussian distributions. The normalized size distribution is shown in Figure 4.2. The frequency, f, is the number of nanoparticles with a diameter within one standard deviation; d is the nanoparticle diameter; and d_m is the most probable nanoparticle diameter.

With increasing temperature, the most probable diameter of observed particles initially decreased trend with a slight decrease from 2.9 ± 0.1 nm to 2.7 ± 0.1 nm, then to 2.3 ± 0.1 nm, while the particle density increased from 2×10^{11} cm^{-2} to 11×10^{11} cm^{-2} and 10×10^{11} cm^{-2}. After 415℃, a significant increase in most probable diameter from 2.3 ± 0.1 nm to 14 ± 0.3 nm was observed with a significant decrease in density from 1×10^{12} cm^{-2} to 1×10^{10} cm^{-2}. For the calculation of density, overlapping areas between analyzed frames were excluded. The process and algorithm for calculating the overlapping area are described in Appendix D. It appears that the growth of larger precipitates might occur at the expense of smaller ones. Therefore, to consider Ostwald ripening with atomic diffusion between participates,[44] we examine the self-similarity of the normalized size distributions. In the normalized size distribution, the y-axis is the product of the mean nanoparticle diameter and the frequency of crystallites with diameters within a specific range (defined by the center of such range), while the x-axis is the specific diameter range (defined by the center of such range) over the mean nanoparticle diameter. However, as shown in Figure 4.2,

the plots are not self-similar; thus, the nanoparticle formation process during nitridation was likely not governed by Ostwald ripening.[45]

4.4 Moiré fringe and lattice spacing analysis nanoparticles

4.4.1 Moiré fringes and analysis of ETEM videos captures

In the ETEM video captures, moiré fringes begin to appear about 6 minutes after nitridation and temperature ramping from 400°C. After the temperature reached 430°C, 1D and 2D moiré pattern with periodicity 3.4 ± 0.4 nm was observed in some particles (Figure 4.7), further indicating that crystal structures with different lattice spacings from the underlying substrate had formed within the nanoparticle. Moiré patterns can be observed by TEM from superposed crystals that differ slightly in either orientation or lattice parameter (or both) produce moiré fringes.[46,47] Two types of moiré patterns, namely 1D MF and 2D MF, were observed in ETEM. Examples are shown in Figure 4.7(a). Since four-fold symmetry is only possible for cubic (ZB InN) but not hexagonal (WZ InN), we consider 2D MF as an indication of cubic crystallinity within nanoparticles. On the other hand, since two-fold symmetry is possible for both hexagonal and cubic structures, 1D MF may be due to either WZ or ZB InN. Among the 25 particles that exhibited moiré fringes (either 1D MF or 2D MF), 12 out of 16 particles exhibited 2D MF for temperature < 520°C, with a 14.0 ± 0.3 nm average particle diameter. For temperature in the range of 520 to 550°C, only 3 out of 9 particles exhibited 2D MF patterns, with a 19.4 nm ± 0.2 nm average particle diameter. Thus, at lower temperatures, smaller particles that more frequently exhibit 2D MF patterns, are observed, while at higher temperatures, larger particles, that rarely exhibiting 2D MF are apparent. Since the fourfold symmetrical 2D MF indicates cubic-on-cubic structure, we hypothesize that there is a higher probability of ZB nucleation from small particles and WZ nucleation from larger particles. A summary of observed nanoparticles is included in Table 4.2.

Under the experimental conditions used in this study, the formation of ZB InN, WZ InN, and In_2O_3 crystallites may occur. Therefore, in order to determine the most likely combinations of lattice spacings that resulted in the observed moiré observed in the ETEM video capture, the expected moiré fringe spacings were calculated using the following equation:[48]

$$D = \frac{d_1 d_2}{|d_1 - d_2|} \qquad \text{(Equation 4.1)}$$

where D is the distance between moiré fringes and d_1 and d_2 are the interplanar distances. The lattice spacings of crystal planes for WZ InN, ZB InN, In_2O_3, including silicon crystal planes, were used in calculations and listed in Table F.3. For instance, using (Equation 4.1, the expected MF spacings resulted from an overlap between ZB InN(001) and Si(001) is

$$D = \frac{4.35 \times 5.47}{|4.35 - 5.47|} = 21.25 \text{ Å} = 2.13 \text{ nm} \qquad \text{(Equation 4.2)}$$

Since our observed MF spacing is 3.4 ± 0.4 nm (Figure 4.7), in the lattice and strain analysis discussed in the next section (section 4.4.2), we look for combinations of lattice plane spacings in Table F.3 that result in expected MF spacings closest to 3.4 nm.

To understand the composition of the nanoparticles observed in ETEM, we also performed EELS in ETEM. The main EELS edges expected in our sample are silicon at 99eV, indium at 443 eV, oxygen at 532 eV, and nitrogen at 401 eV.[49] However, as shown in Figure 4.8, within energy loss range of 75 eV – 450 eV, only silicon edges Si-L_{23} and Si-L_1 are present only silicon edges are present, likely from the TEM grid support. It is often difficult to distinguish the indium peak because its M edges are delayed and overlap with its N and K edges, and in case as well as oxygen peaks.[49,50] To further identify the composition of the nanoparticles studied in this thesis, energy-dispersive X-ray spectroscopy may be considered.

4.4.2 Lattice spacing and strain analysis from TEM images

The nitridated In droplet samples was further investigated under 300 kV FEI Tecnai TEM at Michigan Ion Beam Lab. Real space lattice spacings were identified and estimated using measurements between spots in Fast Fourier Transform (FFT). The procedure of identifying lattice spacings using FFT is described in **C.3**. Within particles with sizes of 9 ± 1 nm, lattice spacings of 0.25 nm most likely associated with ZB InN(111) ($d_{\mathrm{ZB\ InN(111)}}$ = 0.262 nm), WZ InN($10\bar{1}0$) ($d_{\mathrm{WZ\ InN(10\bar{1}0)}}$ = 3.0 Å), and In_2O_3(400) ($d_{\mathrm{In_2O_3(400)}}$= 0.253 nm) were observed (Figure 4.3). Within particles with sizes of 10 ± 2 nm, lattice spacings of 0.30 nm most likely associated with WZ InN($10\bar{1}0$) ($d_{\mathrm{WZ\ InN(10\bar{1}0)}}$ = 0.306 nm) and In_2O_3(222) ($d_{\mathrm{In_2O_3(222)}}$= 0.292 nm) were observed (Figure 4.4). Within particles with sizes of 6 ± 1 nm, lattice spacings of 0.42 nm most likely associated with ZB InN(001) ($d_{\mathrm{ZB\ InN(001)}}$ = 0.453 nm) and In_2O_3(220) ($d_{\mathrm{In_2O_3(220)}}$= 0.357 nm) were observed (Figure 4.5). Within non-nanostructure regions, lattice spacings of 0.20 nm most likely associated with Si(220) ($d_{\mathrm{Si(220)}}$ = 0.192 nm) were observed.[48,51,52] A TEM and full image FFT with identified lattice spacings from ZB InN(111), WZ InN ($10\bar{1}0$), In_2O_3(222) and (400), an Si(220) is shown in Figure 4.6. Thus, we observed from the TEM and FFT a size-dependent polytype selection, where ZB InN is observed in smaller sized particles (Figure 4.5); WZ InN structure is observed in larger sized particle (Figure 4.4). In medium sized particle (Figure 4.3) both WZ and ZB InN were observed.

Combining the information obtained from the analysis of moiré fringe spacings from ETEM and lattice spacings from conventional TEM, we can consider the possible combinations of overlapping planes with different lattice spacings that could result in the observed moiré fringe spacings. We first consider the moiré fringes originated from overlapping between Si(220) observed in non-nanoparticle regions and InN WZ and/or ZB observed in nanoparticles. However,

as defined in (Equation 4.1, the moiré fringes are very sensitive to misfit increase between two overlapping lattices. Any observed lattice spacing 0.25 nm (Figure 4.3), 0.30 nm (Figure 4.4), and 0.42 nm (Figure 4.5), combined with $d_{\mathrm{Si}(220)}$ = 0.192 nm, will result in moiré fringe lattice spacings of 0.83 nm, 0.53 nm, and 0.35 nm, respectively, which are all more than 76% smaller than the observed moiré fringe spacings of 3.4 nm. This observation suggests that the combinations of overlapping lattices that resulted in the moiré fringes we observed in ETEM (Figure 4.7) are not likely coming from InN ZB or WZ with Si(220), but with some lattice planes with lattice spacings closer to InN ZB and/or WZ.

Considering that the lattice spacings observed in conventional TEM are likely coming from the major component of the QDs, we consider the combinations that resulted in the observed moiré fringe spacings coming from InN ZB (or WZ) and In_2O_3, with In_2O_3 being an unintentional oxidation layer formed during ETEM experiment. For the observed 0.25 nm lattice spacings within particles with diameter 9 ± 1 nm, the most likely combination of overlapping lattice spacings is between ZB InN(111) and In_2O_3(400), with a 12% compression in In_2O_3(400) (Figure 4.9(a)). For the observed 0.30 nm lattice spacings within particles with diameter 10 ± 2 nm, the most likely combination of overlapping lattice spacings is between WZ InN($10\bar{1}0$) and In_2O_3(222), with a 13% tension in In_2O_3(222) (Figure 4.9(b)). For the observed 0.42 nm lattice spacings within particles with diameter 7 ± 1 nm, the most likely combination of overlapping lattice spacings is between ZB InN(001) and In_2O_3(220), with a 5% tension in In_2O_3(222) (Figure 4.9(c)). The calculation of strain within QDs is described in Appendix C.3.3. The full analysis of strains expected from different combinations of possible lattice planes is listed in Table C.1.

4.5 Conclusion

In summary, the formation of InN quantum dots during nitridation of In droplets was examined. The size evolution and distribution of nanoparticle from in-situ ETEM video captures was studied using MountainsSPIP® software and fitting with Gaussian as shown in Figure 4.1 and Figure 4.2. For nitridation temperature > 430°C, an increase in nanoparticle size and decrease in nanoparticle density is observed with moiré pattern formation suggesting the formation of a consistently strained interface. The epitaxial relationship between NP and substrate was examined using TEM, and the evolution of the particles was observed using ETEM. Inverse FFT was used to estimate lattice spacing in the TEM images. The observation of size-dependent preference for nucleation of ZB vs. WZ in nitride NPs is also consistent with previous experimental studies on nitride nanostructures synthesized by nitrogen ion implantation into GaAs, followed by thermal annealing.[53,54] These observations suggest that InN QDs via DE through ETEM with ammonia source is achievable, and that polytype selection maybe achieved by tailoring the sizes of InN semiconductor QDs. From the observation of moiré patterns in ETEM and the crystal lattice spacings examined under TEM, we conclude that at lower nitridation temperatures, smaller particles were observed and more of them showed 2D MF related to InN ZB formation. On the other hand, at higher nitridation temperature, larger particles were observed and fewer of them exhibited 2D MF. We hypothesize that there is a higher probability of ZB nucleation from smaller particles and WZ nucleation from larger particles, with unintentional In_2O_3 formation on InN. In addition, we discussed that under different combinations of lattice planes, 12% compression, 13% tension, and 5% tension can be expected within indium oxide. The suggestions for future work following this study are described in Section 7.2.2.

4.6 Tables

Temperature	Most probable diameter	# of nanoparticles analyzed	Overlapping area between frames (nm^2)	Total area analyzed (nm^2)	Nanoparticle density ($x10^{11}$ cm^{-2})
~390°C, before ammonia	2.9 ± 0.1 nm	223	3.20E4	1.06E5	2
400°C; ammonia	2.7 ± 0.1 nm	849	2.4E5	7.8E4	11
415°C	2.3 ± 0.1 nm	94	1.9E4	9.1E4	10
485±60°C	14 ± 0.3 nm	38	4.3E3	7.6E5	0.1

Table 4.1 Table of most probable diameter, number of particles, overlapping area between frames analyzed, total area analyzed for each temperature range, and density of nanoparticles for each temperature (range) before and after nitridation, determined from an analysis of frames from in-situ ETEM video captures.

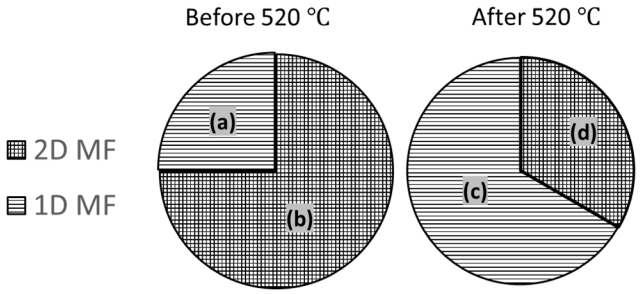

	# of particles	Moire fringe (MF) type	Average diameter [nm]
(a)	4	1D	11.2
(b)	12	2D	14.0
(c)	6	1D	16.2
(d)	3	2D	19.4

Table 4.2 Summary of particles with moiré lattice fringes observed in ETEM. Among the 25 particles that exhibited moiré fringes (either 2D MF or 1D MF), 12 out of 16 particles exhibited 2D MF patterns before 520°C, with 14.0 nm average particle diameter. Between 520-550°C, only 3 out of 9 particles exhibited 2D MF, with 19.4 nm average particle diameter. In the pie charts, grids represent 2D MF moiré patterns and horizontal stripes represent 1D MF patterns. For each section of the pie charts, the details are listed in the corresponding rows of the table on the right.

4.7 Figures

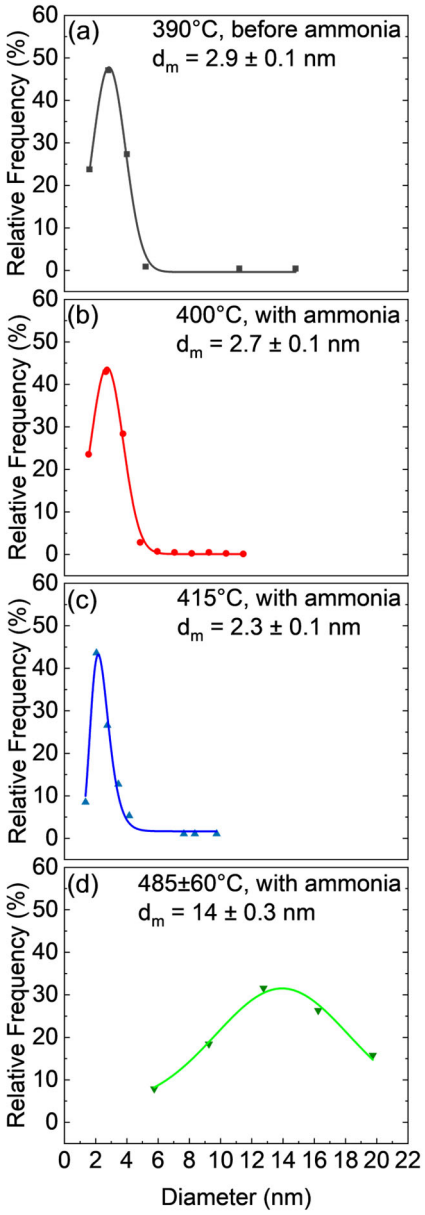

Figure 4.1 Size distribution of nanoparticles before and after nitridation, determined from an analysis of frames from in-situ ETEM video captures. (a), (b), and (d) are fitted using a gaussian distribution with $R^2 > 0.99$. (c) is fitted with a lognormal distribution with $R^2 = 0.99$. The frequency, f, is the percentage of nanoparticles with diameters within a specific range (one standard deviation); and d_m is the mean nanoparticle diameter.

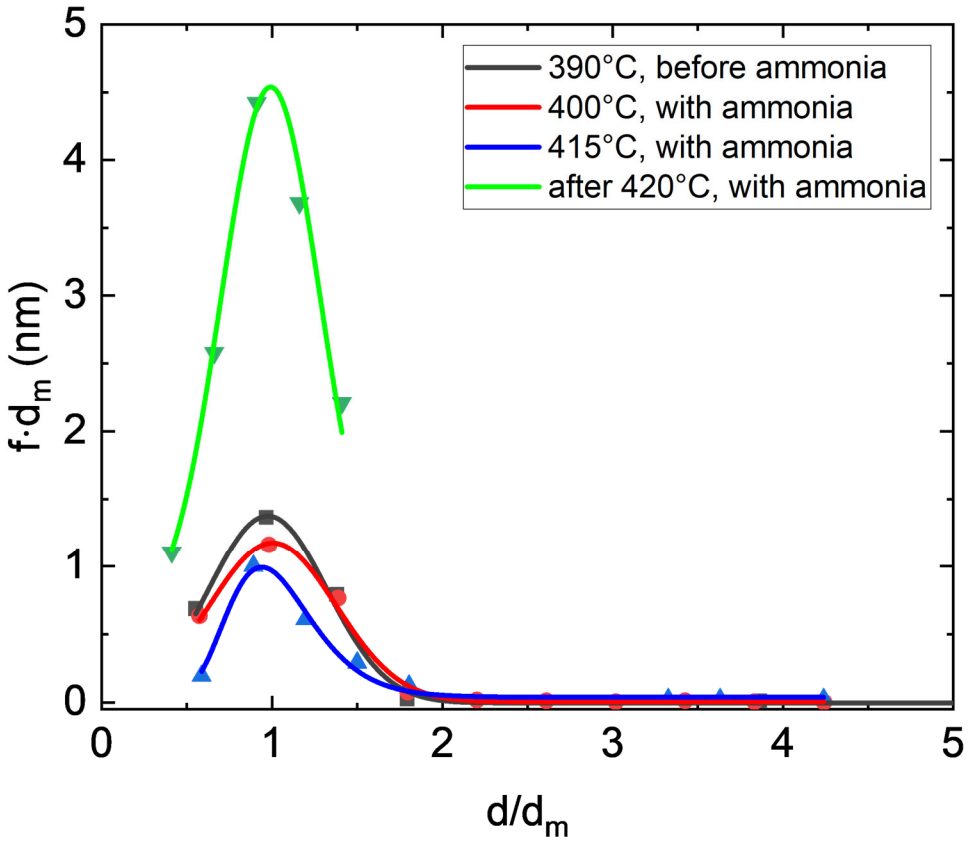

Figure 4.2 Normalized size distribution of nanoparticles before and after nitridation, determined from an analysis of frames from in-situ ETEM video captures. The frequency, *f*, is the percentage of crystallites with diameters within a specific range; *d* is the nanoparticle diameter; and d_m is the mean nanoparticle diameter.

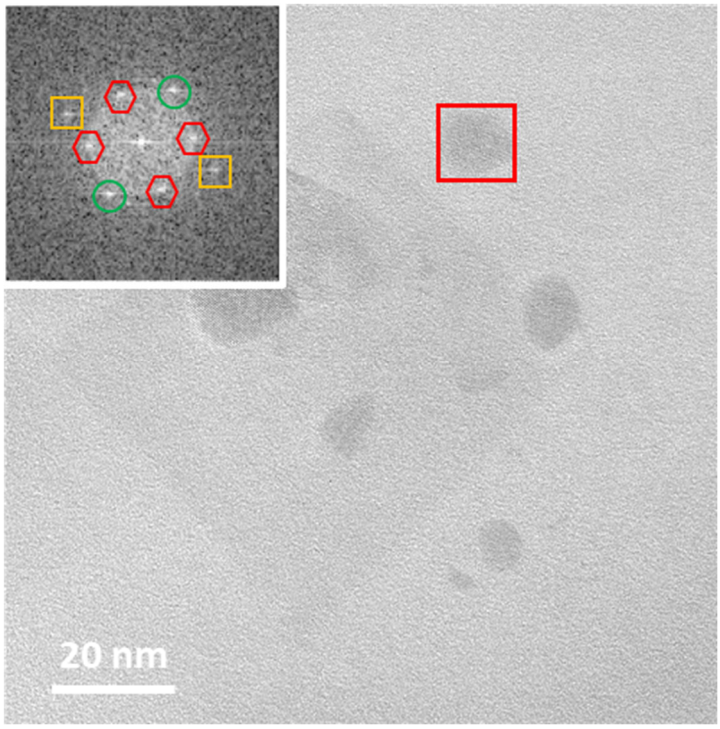

Figure 4.3 Particles observed under 300 kV FEI Tecnai TEM at the Michigan Ion Beam Lab. For the nanoparticles with diameter ~ 9 nm, the FFT of the boxed area is shown in the inset. Within such particle: diffraction spots from background Si(220) corresponding to d = 2.0 Å is indicated by yellow squares (□); diffraction spots from ZB-InN(111) corresponding to d = 2.5 Å is indicated by green circles (○); diffraction spots from WZ-InN($10\bar{1}0$) corresponding to d = 3.0 Å is indicated by red hexagons (⬡) . The TEM images were taken by Abby Liu in Prof. Goldman's research group.

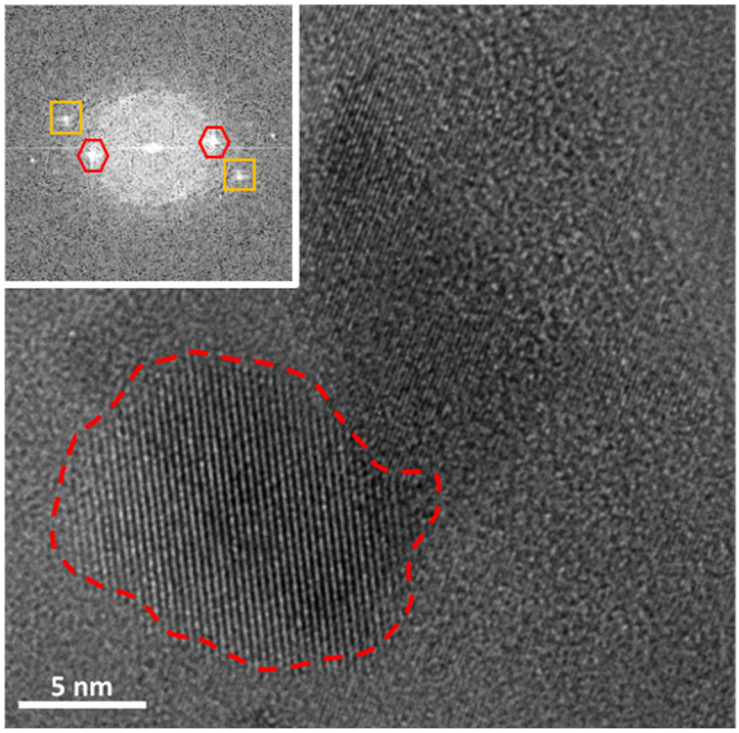

Figure 4.4 Particles observed under 300 kV FEI Tecnai TEM at Michigan Ion Beam Lab. TEM of particles with diameter ~15 nm, outlined in red with FFT shown in the inset. FFT of area outlined in red and a pair of spots corresponding to the lattice spacings in the larger particle circled in red. Diffraction spots from WZ-InN($10\bar{1}0$) corresponding to d = 3.0 Å is indicated by red hexagons (⬡) . Diffraction spots from background Si(220) corresponding to d = 2.0 Å is indicated by yellow squares (□). The TEM images were taken by Abby Liu in Prof. Goldman's research group.

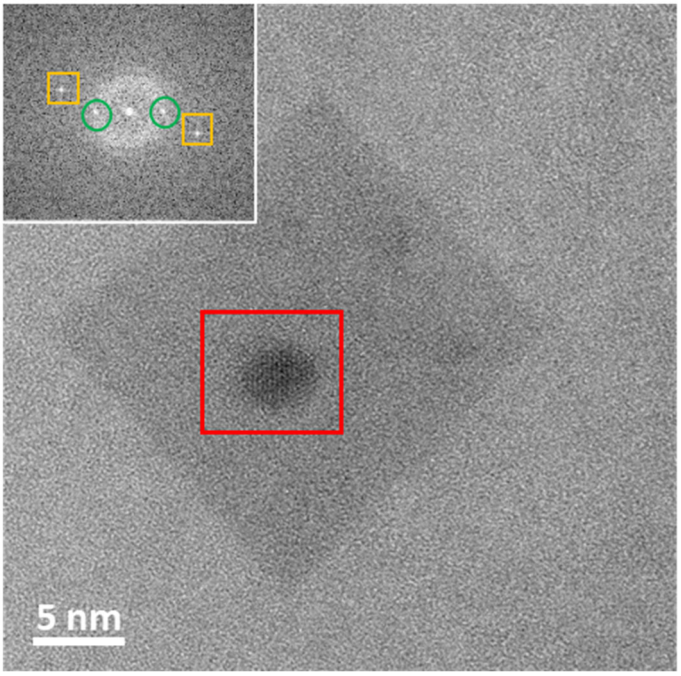

Figure 4.5 Particles observed under 300 kV FEI Tecnai TEM at Michigan Ion Beam Lab. TEM of particles with diameter ~6 nm. The FFT of the boxed area in the inset with the pair of FFT spots analyzed circled in red. Diffraction spots from background Si(220) corresponding to d = 2.0 Å is indicated by yellow squares (□). Diffraction spots from background Si(220) corresponding to d = 4.2 Å is indicated by yellow squares (○). The TEM images were taken by Abby Liu in Prof. Goldman's research group.

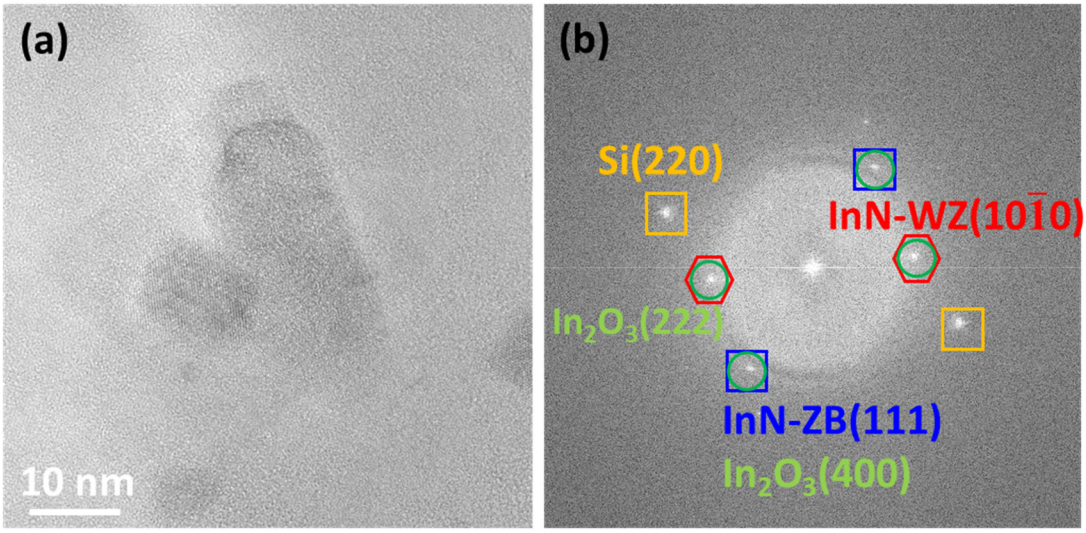

Figure 4.6 Particles observed under 300 kV FEI Tecnai TEM at Michigan Ion Beam Lab. (a) TEM and (b) Full image FFT with identified lattices spacings from ZB InN(111), WZ InN (10$\bar{1}$0), In_2O_3(222) and (400), and Si(220), with yellow squares (□) representing silicon planes diffraction spots, green circles (○) representing In_2O_3 diffraction spots, blue squares (□) representing ZB-InN planes diffraction spots, and red hexagons (⬡) representing WZ-InN planes diffraction spots.

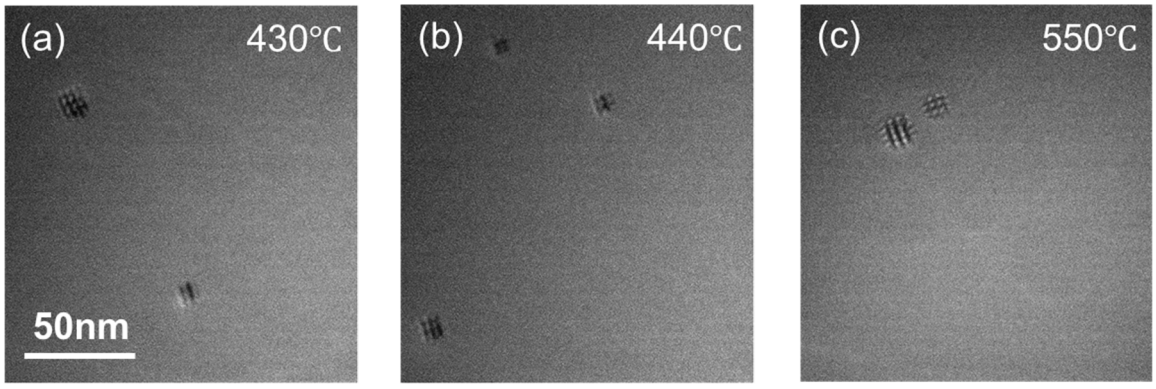

Figure 4.7 Representative frames from ETEM video captures taken at different sample heater temperatures: (a) 430°C, (b) 440°C, and (c) 550°C. Moiré patterns were observed in ETEM video captures after 430°C. Both 2D MF and 1D MF types of moiré pattern are present in (a). Despite the observed increase in sizes of the nanoparticles, the observed periodicity of the moiré pattern remained the same at 3.4 ± 0.4 nm.

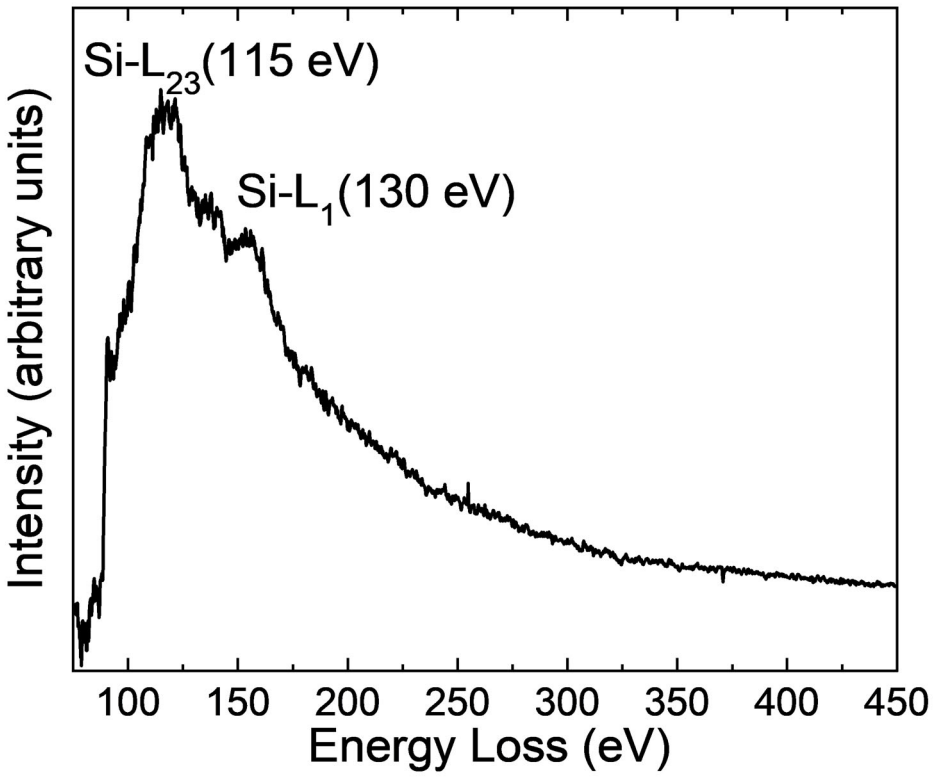

Figure 4.8 The energy loss edges of nanoparticle sample examined using EELS equipped on Titan 80-300 TEM. Within the energy loss range of 75 eV – 450 eV, only silicon edges Si-L_{23} and Si-L_1 are present, likely from the TEM grid support. The main EELS edges for indium at 443 eV and nitrogen at 401 eV are not observed.

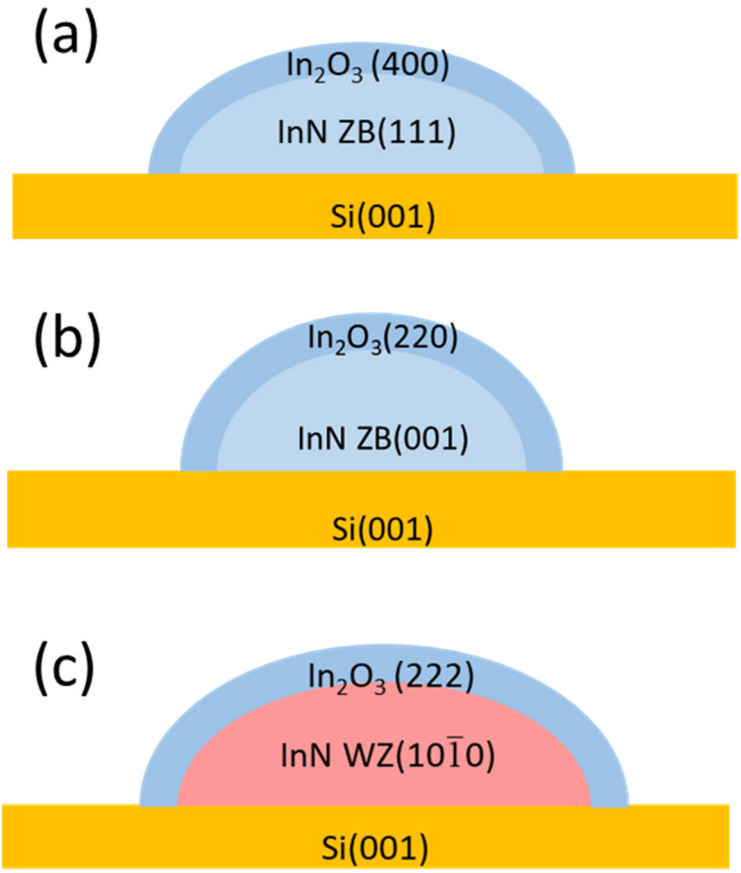

Figure 4.9 Schematics of QD structures and lattice plane combinations that result in observed moiré fringe spacings. (a) In nanoparticles with diameter 9 ± 1 nm with observed 0.25 nm lattice spacings, the most likely combination of overlapping lattice spacings is between ZB InN(111) and In_2O_3(400), with a 12% compression in In_2O_3 layer. (b) In nanoparticles with diameter 7 ± 1 nm with observed 0.40 nm lattice spacings, the most likely combination of overlapping lattice spacings is between ZB InN(001) and In_2O_3(220), with a 5% tension in In_2O_3 (222). (c) In nanoparticles with diameter 10 ± 2 nm and observed 0.30 nm lattice spacings, the most likely combination of overlapping lattice spacings is between WZ InN(10$\bar{1}$0) and In_2O_3 (222), with a 13% tension in In_2O_3 layer. In the schematics, cubic structures such as ZB InN and In_2O_3 are shaded in blue, and hexagonal structures such as WZ InN are shaded in red. The calculation of strain within QDs is described in Appendix C.3.3. The full analysis of strains expected from different combinations of possible lattice planes is listed in Table C.1.

4.8 References

[1] A.G. Bhuiyan, A. Hashimoto, and A. Yamamoto, "Indium nitride (InN): A review on growth, characterization, and properties", J. Appl. Phys. 94, 2779 (2003).

[2] J. Wu, W. Walukiewicz, K.M. Yu, J.W. Ager III, E.E. Haller, H. Lu, W.J. Schaff, Y. Saito, and Y. Nanishi, "Unusual properties of the fundamental band gap of InN", Appl. Phys. Lett. 80, 3967 (2002).

[3] T. Matsuoka, H. Okamoto, M. Nakao, H. Harima, and E. Kurimoto, "Optical bandgap energy of wurtzite InN", Appl. Phys. Lett. 81, 1246 (2002).

[4] V.W.L. Chin, T.L. Tansley, and T. Osotchan, "Electron Mobilities in Gallium, Indium, and Aluminum Nitrides", J. Appl. Phys. 75, 7365 (1994).

[5] B.R. Nag, "Electron Mobility in Indium Nitride", J. Cryst. Growth, 269, 35 (2004).

[6] P. Carrier and S.-H. Wei, "Theoretical Study of the Band-Gap Anomaly of InN", J. Appl. Phys. 97, 033707 (2005).

[7] C.E. Reilly, C. Lund, S. Nakamura, U.K. Mishra, S.P. DenBaars, and S. Keller, "Infrared luminescence from N-polar InN quantum dots and thin films grown by metal organic chemical vapor deposition", Appl. Phys. Lett. 114 241103 (2019).

[8] Y. Zhao, H. Wang, X. Li, J. Li, Z. Shi, G. Wu, S. Zhuang, C. Yin, and F. Yang. "Parametric study on the well-oriented growth of $In_xAl_{1-x}N$ nanodots by magnetron sputtering", Mater. Sci. Semicond. Process. 102, 104583 (2019).

[9] V.Y. Davydov, A.A. Klochikhin, R.P. Seisyan, V.V. Emtsev, S.V. Ivanov, F. Bechstedt, J. Furthmuller, H. Harima, A. Mudryi, J. Aderhold, O. Semchinova, and J. Graul, "Absorption and Emission of Hexagonal InN. Evidence of Narrow Fundamental Band Gap", Phys. Stat. Sol. (b). 229, r1 (2002).

[10] N. Puychevrier, and M. Menoret, "Synthesis of III–V Semiconductor Nitrides by Reactive Cathodic Sputtering", Thin Solid Films. 36, 141 (1976).

[11] K.L. Westra, and M.J. Brett, "Near IR Optical Properties of Sputtered InN Films". Thin Solid Films. 192, 227 (1990).

[12] Y. Uesaka, A. Yamamoto, and A. Hashimoto, "Band Gap Widening of MBE Grown InN Layers by Impurity Incorporation", J. Cryst. Growth, 278 402 (2005).

[13] F. Bechstedt, J. Furthmüller, M. Ferhat, L.K. Teles, L.M.R. Scolfaro, J.R. Leite, V.Y. Davydov, O. Ambacher, and R. Goldhahn, "Energy Gap and Optical Properties of $In_xGa_{1-X}N$. Physica Status Solidi (a) 195, 628 (2003).

[14] M. Stupca, M. Alsalhi, T. Al Saud, A. Almuhanna, and M. Nayfeh, "Enhancement of polycrystalline silicon solar cells using ultrathin films of silicon nanoparticle", Appl. Phys. Lett. 91, 063107 (2007).

[15] S. Alkis, A.K. Okyay, and B. Ortaç, "Post-Treatment of Silicon Nanocrystals Produced by Ultra-Short Pulsed Laser Ablation in Liquid: Toward Blue Luminescent Nanocrystal Generation", J. Phys. Chem. C, 116, 3432 (2012).

[16] S. Alkis, F.B. Oruç, B. Ortaç, A.C. Kosger, and A.K. Okyay, "A plasmonic enhanced photodetector based on silicon nanocrystals obtained through laser ablation", J. Opt. 14, 125001 (2012).

[17] S. Alkis, T. Öztas, L. Aygün, F. Bozkurt, A. Okyay, and B. Ortaç, "Thin film MoS2 nanocrystal based ultraviolet photodetector", Opt. Express, 20, 21815 (2012).

[18] M. Buegler, M. Alevli, R. Atalay, G. Durkaya, I. Senevirathna, M. Jamil, I. Ferguson, and N. Dietz. "Optical and structural properties of InN grown by HPCVD", Proc. SPIE. 7422 742218 (2009).

[19] S. Alkis, F.I. Chowdhury, M. Alevli, N. Dietz, B. Yalızay, S. Aktürk, A. Nayfeh, and A.K. Okyay, "Enhancement of polycrystalline silicon solar cells efficiency using indium nitride particles", J. Opt. 17, 105903 (2015).

[20] F.I. Chowdhury, K. Islam, S. Alkis, B. Ortaç, M. Alevli, N. Dietz, A. Okyay, and A. Nayfeh, "Enhanced Light Scattering with Energy Downshifting Using 16 Nm Indium Nitride Nanoparticles for Improved Thin-Film a-Si N-I-P Solar Cells", Meet. Abstr. MA2015-01 2259 (2015).

[21] M. Kumar, M.K. Rajpalke, T.N. Bhat, B. Roul, A.T. Kalghatgi, and S.B. Krupanidhi, "Size Dependent Bandgap of Molecular Beam Epitaxy Grown InN Quantum Dots Measured by Scanning Tunneling Spectroscopy", J. Appl. Phys. 110, 114317 (2011).

[22] C.Y. Yeh, Z.W. Lu, S. Froyen, and A. Zunger, "Zinc-Blende–Wurtzite Polytypism in Semiconductors", Phys. Rev. 46, 10086 (1992).

[23] T. Ito, "Simple Criterion for Wurtzite-Zinc-Blende Polytypism in Semiconductors", Jpn. J. Appl. Phys. 37, L1217 (1998).

[24] D. Jacobsson, F. Panciera, J. Tersoff, M.C. Reuter, S. Lehmann, S. Hofmann, K.A. Dick, and F.M. Ross, "Interface Dynamics and Crystal Phase Switching in GaAs Nanowires", Nature, 531, 317 (2016).

[25] V.G. Dubrovskii, N.V. Sibirev, N.N. Halder, and D. Ritter, "Classification of the Morphologies and Related Crystal Phases of III–V Nanowires Based on the Surface Energy Analysis". J. Phys. Chem. C. 123, 18693 (2019).

[26] F. Glas, J.C. Harmand, and G. Patriarche, "Why Does Wurtzite Form in Nanowires of III-V Zinc Blende Semiconductors?" Phys. Rev. Lett. 99, 146101 (2007).

[27] V. Pankoke, S. Sakong, and P. Kratzer, "Role of Sidewall Diffusion in GaAs Nanowire Growth: A First-Principles Study", Phys. Rev. B. 86, 085425 (2012).

[28] N.B. Uner, D.M. Niedzwiedzki, and E. Thimsen, "Nonequilibrium Plasma Aerotaxy of InN Nanocrystals and Their Photonic Properties", J. Phys. Chem. C. 123, 30613 (2019).

[29] M. Kumar, B. Roul, T. N. Bhat, M.K. Rajpalke, and S.B. Krupanidhi, "Substrate impact on the grown of InN nanostructures by droplet epitaxy", Phys. Status Solidi C. 10, 409 (2013).

[30] B. Qi, S. Olafsson, M. Gothelid, H.P. Gislason, and B. Agnarrson, "Photoemission and low energy electron microscopy study on the formation and nitridation of indium droplets on Si (111)7 × 7 surfaces", Thin Solid Films 531, 61 (2013).

[31] M. Kumar, B. Roul, A. Shetty, M.K. Rajpalke, T.N. Bhat, A.T. Kalghatgi, and S.B. Krupanidhi, "Temperature dependent transport studies in InN quantum dots grown by droplet epitaxy on silicon nitride/Si substrate", Appl. Phys. Lett. 99, 153114 (2011).

[32] P. Aseev, Z. Gacevic, J.M. Mánuel, J.J. Jiménez, R. García, F.M. Morales, and E. Calleja, "Formation mechanisms of single-crystalline InN quantum dots fabricated via droplet epitaxy", J. Cryst. Growth 493, 65 (2018).

[33] Z. Zhang, J. Li, Y. Zhou, H. Fu, Z. Zhang, G. Xiang, Y. Zhao, S. Zhuang, F. Yang, and H. Wang, "Effect of Sputtering Power on the Structural and Optical Properties of Inn Nanodots on Al_2O_3 by Magnetron Sputtering", Mat. Res. 22, e20190380 (2019).

[34] H. J-Y. Chen, D-L Yang, T-W Huang, and I-S Yu, "Formation and Temperature Effect of InN Nanodots by PA-MBE via Droplet Epitaxy Technique", Nanoscale Res Lett. 11, 241 (2016).

[35] I. Choi, H. Lee, C.-R Lee, K-U Jeong, and J.S. Kim, "Formation of spherical-shaped GaN and InN quantum dots on curved SiN/Si surface", Nanotechnology, 29, 315603 (2018).

[36] H. J-Y Chen, Y-Z Su, D-L Yang, T-W Huang, and I-S Yu, "Effects of substrate pre-nitridation and post-nitridation processes on InN quantum dots with crystallinity by droplet epitaxy", Surf. Coat. Technol. 324, 491 (2017).

[37] H.B. Ahn, Y.H. Kim, M.D. Kim, C.S. Kim, and J.Y. Lee, "Formation and Microstructural Characterization of In_2O_3 Sheath Layer on InN Nanostructures", Chem. Phys. Lett. 499, 131 (2010).

[38] B-G Park, M. Reddeppa, Y.H. Kim, S-G Kim, and M-D Kim, "Hydrogen-produced In_2O_3/InN Core-shell Nanorod and its Effect on NO_2 Gas Sensing Behavior", Nanotechnology. 31, 335503 (2020).

[39] H.F. Liu, D.Z. Chi, and W. Liu, "Layer-by-layer Oxidation of InN(0001) Thin Films into Body-center Cubic In_2O_3(111) by cycle rapid thermal annealing", CrystEngComm, 14, 7140 (2012).

[40] E. Luna, J. Grandal, E. Gallardo, J.M. Celleja, M.A. Sanchez-Garcia, E. Callejia, and A. Trampert, "Investigation of III-V Nanowires by Plan-View Transmission Electron Microscopy: InN Case Study", Microsc. Microanal. 20, 1471 (2014).

[41] T.N. Bhat, M.K. Rajpalke, B. Roul, M. Kumar, S.B. Krupanidhi, and N. Shiha, "Evidence for ambient oxidation of indium nitride quantum dots", Phys. Status. Solidi. 248, 2853 (2011).

[42] D. Gonzalez, J. G. Lozano, H. Herrera, F. M. Morales, S. Ruffenach, O. Briot, and R. Garcia, "Phase Mapping of Aging Process in InN Nanostructures: Oxygen Incorporation and the Role of the Zinc blende Phase", Nanotechnology. 21, 185706 (2010).

[43] R.E. Diaz, R. Sharma, K. Jarvis, Q. Zhang, and S. Mahajan. 2012. "Direct observation of nucleation and early stages of growth of GaN nanowires." J. Cryst. Growth 341:1.

[44] P.W. Voorhees, "The theory of Ostwald ripening", J. Stat. Phys. 38, 231 (1985).

[45] Y. Masuda and R. Watanabe, Sintering Processes, Materials Science Research, Vol. 13 (Plenum, New York, 1979).

[46] S. Amelinckx and J.V. Landuyt, "Transmission Electron Microscopy" in Encyclopedia of Physical Science and Technology (Third Edition), 2003.

[47] I. Amidror, *The Theory of the Moiré Phenomenon*; Kluwer Academic: Dordrecht; Boston, 2000.

[48] F. Komarov, L. Vlasukova, W. Wesch, A. Kamarou, O. Milchanin, S. Grechnyi, A. Mudryi, and A. Ivaniukovich, "Formation of InAs nanocrystals in Si by high-fluence ion implementation", Nucl. Instrum. Methods Phys. Res. B. 266, 3557 (2008).

[49] D.H. Anjum, I.A. Qattan, S. Patole, E.M. Diallo, N. Wei, and H. Heidbreder, "Nano-characterization of silicon-based multilayers using the technique of STEM-EELS spectrum-imaging", Mater. Today Commun. 25, 101209 (2020).

[50] S. Joseph and S. Berger, "A study of crystallographic phases in non-stoichiometric (oxygen deficiency) indium oxide thin films", J. Mater. Sci. 52 1988 (2017).

[51] M. De Seta, G. Capellini, F. Evangelisti, and C. Spinella, "Intermixing-promoted scaling of Ge/Si(100) island sizes", J. Appl. Phys. 92, 614 (2002).

[52] M. Wu, A. Trampert, T. Al-Zoubi, M. Benyoucef, and J.P. Reithmaier, "Interface structure and strain state of InAs nano-clusters embedded in silicon", Acta Mater. 90, 133 (2015).

[53] A.W. Wood, X. Weng, Y.Q. Wang, and R.S. Goldman, "Formation mechanisms of embedded wurtzite and zincblende indium nitride nanocrystals", Appl. Phys. Lett. 99, 093108 (2011).

[54] A.W. Wood, R.R. Collino, P.T. Wang, Y.Q. Wang, and R.S. Goldman, "Formation and transformation of embedded GaN nanocrystals", Appl. Phys. Lett. 100, 203113 (2012).

Chapter 5

Influence of Gallium Surface Saturation on GaN Nanowire Polytype Selection During Molecular-Beam Epitaxy

5.1 Overview

In this chapter, we present the study of the influence of gallium surface saturation of GaN nanowire polytype selection during molecular beam epitaxy. The background of this study is discussed in Section 5.2. The experimental details of the synthesis of film and NWs are described in Section 2.3.3. The growth process involves two steps: Ga pre-deposition followed by GaN growth. For the discussion of mechanisms, we first discuss the mechanism of morphological selection - i.e., the selection between nanowire and film. We discuss the influence of Ga flux during the GaN growth stage on NW to film transition in Section 5.3. We then discussed the mechanism of polytype selection in GaN. We discuss the influence of Ga surface saturation from Ga pre-deposition step in Section 5.4. Last, we discuss a post-mortem study of GaN NW and film THEED patterns at various stages of growth and suggestions for future growth in Section 5.5.

5.2 Background

Gallium nitride (GaN) nanowires have shown significant potential for a wide range of optical and electronic applications.[1] Although much progress has been made in GaN-based multi-quantum well light emitters, their efficiency is often limited by misfit strain-induced polarization, which leads to the spatial separation of electrons and holes.[2] Alternatively, in nanowires (NWs),

the strain-induced polarization is reduced due to an increase in the surface-to-volume ratio relative to those of bulk films.[3] On Si substrates, GaN NWs typically exhibit the WZ structure, with a spontaneous polarization that also leads to electron–hole spatial separation.[4] On the other hand, the zinc blende (ZB) polytype of GaN, which lacks a spontaneous polarization, is an ideal candidate for high-efficiency visible optoelectronics.[5,6] Thus, the epitaxial growth of ZB GaN NWs on Si(001) is a crucial step toward the monolithic integration of solid-state light-emitters with CMOS via direct-wafer-bonding.[7] On Si(001), WZ GaN NWs,[8,9] ZB GaN nanopyramids,[10] and monolayer-height ZB inclusions in WZ GaN NWs[11,12,13] have been demonstrated. In addition, the nucleation of vertical NWs on Si_xN_y/Si(111) has been attributed to polarity-driven[14,15,16] and surface energy anisotropy-driven [17] transitions from spherical cap-shaped islands to NW. Furthermore, the growth of GaN NWs directly on Si(111) has been attributed to sidewall diffusion.[18,19] However, a framework for GaN polytype and morphology (i.e., film vs NW) selection on Si(001) has yet to emerge. In addition, although a staggered type-II band-offset has been reported for a case with multiple ZB inclusions within a WZ matrix,[11] the band-offset between adjacent WZ and ZB GaN phases has not been reported. Here, we examine the influence of Ga surface saturation on GaN nanowire polytype selection during molecular-beam epitaxy (MBE) on CMOS-compatible Si(001). We discussed the interplay between surface and step-edge diffusion barriers governing the NW-to-film transition and revealed the influence of Si_xN_y interlayer formation on the selection of the ZB vs WZ polytype. In addition, distinct exciton emissions associated with ZB and WZ GaN suggest a type-I WZ/ZB GaN band-offset. These findings are expected to be applicable to a wide range of III-nitride alloys and heterostructures.

5.3 Influence of Ga flux on NW to film selection

As shown in Figure 5.1 and Figure 5.2, the structures consist of pure WZ GaN NWs as well as ZB GaN NWs and films that transform to the WZ polytype at a finite height. For the pure WZ NWs, the RHEED patterns reveal the WZ polytype during the early [Figure 5.1 (b)] and late [Figure 5.1 (c) and Figure 5.1 (d)] stages of growth, similar to literature reports;[20,21] post-growth XRD spectra [Figure 5.2(b)] exhibit peaks at $2\theta = 34.7°$, corresponding to WZ-GaN (002). On the other hand, a layer-thickness-dependent transition from ZB to WZ is revealed by the RHEED patterns in Figure 5.1 (f)–(h) for films and in Figure 5.1 (j)–(l) for NWs. As shown in the tilted SEM image in Figure 5.2, the GaN morphology consists of vertically oriented NWs and film with a height of 180 ± 10 nm. The ZB to WZ polytype transition is supported by post-growth LIBAD. For the most shallow incidence angles, θ_i, the XRD spectra in Figure 5.2(d) and Figure 5.2(f) exhibit peaks at $2\theta = 34.7°$ and 37.1°, corresponding to WZ-GaN(002) and WZ-GaN(101), revealing WZ GaN near the surface. As the incidence angle is increased, an additional peak at $2\theta = 40.0°$, corresponding to ZB-GaN(200), reveals the presence of ZB GaN near the substrate/layer interface. For $\theta_i = 1°$, 5°, and 8°, the information depths[22] are 131, 145, and 148 nm; thus, both GaN films and NWs consist of a WZ-on-ZB structure, with ZB-WZ transition at a height of approximately 20 ± 2 nm. Similar size-dependent ZB to WZ polytype transitions have been reported for GaN and other materials whose thermodynamically stable form is the WZ polytype.[23,24,25,26,27,28]

A map of the Ga-flux-dependence of the NW vs film and ZB vs WZ polytype selection is shown in Figure 5.3(c), a plot of $T_{substrate}$ vs Ga BEP, with the N/Ga flux ratio shown on the top x-axis. Each position on the plot represents the conditions for pre-deposition and nitridation steps, with the circle or square designation representing the film vs NW formation for fixed fluxes only.

For example, low Ga flux during pre-deposition and nitridation, i.e., "low–low," leads to WZ NW formation, as shown schematically in Figure 5.3(b). On the other hand, high Ga flux during pre-deposition and nitridation, i.e., "high–high," leads to the formation of WZ-on-ZB films, as shown in Figure 5.3(d). Finally, high Ga flux during pre-deposition, followed by low Ga flux during nitridation, i.e., "high–low," illustrated by the blue circles surrounding two positions on the plot, leads to the formation of WZ-on-ZB NWs, as shown in Figure 5.3(a). We hypothesize that the high Ga flux during pre-deposition enables the epitaxy of ZB GaN on silicon, while the subsequent low Ga flux during nitridation facilitates nanowire formation.

To explain the NW-to-film transition at both high Ga-flux and high substrate temperature, we consider the relative roles of lateral (surface) and vertical (step-edge) diffusion.[29] Since the diffusivity of N is expected to be several orders of magnitude lower than that of Ga,[30] we focus on the lateral Ga surface diffusion length, λ_{Ga}, which depends on the Ga surface diffusivity, D_{Ga}, and the Ga-flux, F_{Ga}, as follows:[31]

$$\lambda_{Ga} \cong \left(\frac{D_{Ga}}{F_{Ga}}\right)^{\frac{1}{6}} \qquad \text{(Equation 5.1)}$$

At step-edges, the downward diffusion of adatoms is hindered by the Ehrlich–Schwoebel step-edge barrier, E_e.[32,33] Thus, there is a critical island lateral size, R_c, beyond which additional layers nucleate on top of the first-floor islands, leading to the formation of NWs. For the low Ga flux, the higher λ_{Ga} leads to an island separation, L_D, greater than R_c. Thus, adatoms are unable to overcome E_e; instead, they nucleate on top of the first-floor islands, eventually forming GaN NWs. This process might also involve a strain-induced shape transition as described by Consonni et al.[17] We note that Ga droplets are not observed at our NW tips, consistent with literature reports on MBE-grown GaN NWs.[18,34] For the high Ga-flux, the lower λ_{Ga} leads to $L_D < R_c$; thus, the islands coalesce, leading to the formation of GaN films.

5.4 Influence of Ga surface saturation on ZB vs. WZ polytype selection

We now discuss polytype selection in films and NWs. We hypothesize that the high Ga-flux during Ga pre-deposition has hindered Si_xN_y formation, allowing epitaxy of ZB GaN on silicon, similar to the predictions of a recent report.[35] During the nitridation step, the low Ga-flux results in a high surface diffusivity with island separations exceeding Rc, leading to nucleation on top of first-floor islands and the formation of GaN NWs. It is interesting to note that the transformation from ZB to WZ occurs after ~1 h of growth for both films and NWs. Therefore, the transformation is likely not due to a random event but instead may be due to the heating of the growth surface by the gallium furnace or the N plasma source.[36] Further work is in progress to determine the role of surface temperature on ZB-WZ polytype transformations during epitaxy of GaN NWs[37] and films.

To determine the effective bandgaps and band-offsets at the WZ/ZB GaN interfaces, we compare the low-temperature PL spectra in Figure 5.4(a) with the nanoscale geometries from Figure 5.1. Since the NW diameters are comparable to the de Broglie wavelength of GaN (~20 nm),[38] quantum confinement in two dimensions is expected. The estimated effective bandgaps are

$$E_{g,\,effective}^{ZB/WZ} = E_g^{ZB/WZ} + \hbar^2\pi^2\left(\frac{1}{m_e^*}+\frac{1}{m_h^*}\right)\left(\frac{2}{d}\right)^2 \qquad \text{(Equation 5.2)}$$

where d is the diameter of the NW; $E_g^{ZB/WZ}$ is the temperature dependent energy bandgap for bulk WZ and ZB GaN; the electron effective masses, m_e^*, are $0.13m_0$ (ZB) and $0.2m_0$ (WZ); and the hole effective masses, m_h^*, are $1.3m_o$ (ZB) and $1.6m_o$ (WZ).[39] The computed effective band gaps at 10 K for WZ and ZB are 3.47 and 3.32 eV, respectively, which match the peaks in the PL spectra shown in Figure 5.4(a). For the WZ NWs, the 3.47 emission is associated with WZ excitonic transitions.[40] For the WZ-on-ZB NWs, the 3.17 eV emission due to the ZB DAP is apparent.[41] For

the WZ-on-ZB NWs, emissions at 3.47 and 3.42 eV are attributed to the excitonic[42] and donor-acceptor-pair (DAP) transitions[43] of WZ GaN, respectively, while the emissions at 3.34 and 3.16 eV are related to the excitonic[44] and DAP transitions[45] of ZB GaN, respectively. Since our GaN is unintentionally doped,[46] the presence of the DAP emission is anticipated.[47]

To explain the presence and absence of the WZ GaN emission for the WZ-on-ZB NWs and the WZ-on-ZB films, we consider a nested type-I band-offset at the WZ/ZB interface, as shown in Figure 5.4(b) and Figure 5.4(c). Due to the high interfacial area for the WZ-on-ZB films, it is hypothesized that electrons from the WZ conduction band (CB) relax into the ZB CB, subsequently recombining radiatively with holes in the ZB valence band (VB), leading to the prominent ZB emission peak, shown in the PL spectra in Figure 5.4(a). On the other hand, due to the reduced WZ/ZB interfacial area for the WZ-on-ZB NWs, limited relaxation of electrons from the WZ to ZB CB occurs. Given the ~60 μm laser spot diameter, the ~20 nm NW diameter, and the $\sim 6 \times 10^{10}$ cm^{-2} NW density, the WZ/ZB NW fraction of interfacial area is 10^{-7} for a single NW and ~0.2 for an ensemble of NWs. In both cases, the NW interfacial areas are reduced compared to those of the films. Together, these findings suggest a nested type-I band-offset at the WZ/ZB GaN interface, consistent with predictions of the quasiparticle electronic-structure theory.[48,49] Further studies are needed to elucidate the origins of the emission peaks.

5.5 RHEED study of NW RHEED and film growth of GaN

Growth details and XRD of GaN NWs growth attempt after the replacement of Veeco plasma source is described in Section 2.3.3 and Appendix A. Following growths, dendrites were observed on the surface of the sample (via SEM) but these dendrites were removed using a cleaning process described in Appendix A. XRD scans ranges from 32.9°–33.0°, 33.6°–34.7°, 36.7°–37.2°, and 39.8°–40.3° were used to verify the presence of WZ($10\bar{1}0$), WZ(0002), WZ($10\bar{1}1$), and

ZB(200), respectively, in the sample. From the XRD scans, only WZ GaN($10\bar{1}0$) were observed, as shown in Figure A.2. A chart of d-spacing and 2 theta for GaN XRD is included in Table F.1 and Table F.2. To re-establish ZB/WZ NW growth condition using Addon plasma source, and examine the effect of surface charging by the electron beam from the RHEED, specific growth approach and plan is described in Chapter 7.2.1 and Table 7.1. In the growth map plotted in Figure 5.3, for all samples, nitrogen flux is kept the same and plasma was ignited using 400W with a flow rate of 1 sccm using the Veeco plasma source, while Ga flux is varied. It has been shown in our current study that N/Ga≈33 results in NW formation. Since the Addon plasma has not been fully test for nitride growth, the suggested growths in Table 7.1 intend to explore different values of nitrogen flux, while keeping N/Ga≈33 to establish desired nitrogen plasma source condition.

An interesting observation of the WZ to ZB transition in both films and NWs is that the transition from ZB to WZ occurs at approximately the same depth. Therefore, the transition is not likely due to a random event but may instead be due to heating and/or electrostatic charging of the growth surface by the gallium furnace, the N plasma source, and/or the RHEED source. RHEED can be used to qualitatively review the surface morphology during the growth process. It can also be used to quantitatively study the crystal orientations during growth. To do so requires detailed and precise identification of the spots and their location. However, RHEED diffraction captured on the fluorescent screen is usually a limited view (above shadow edge) of the entire diffraction pattern, and the spots can vary greatly in brightness. Simple post extraction based on single threshold applied to the entire image will overlook most of the spots that are not in the center. To overcome this issue, I developed a script that can extract RHEED patterns across the whole image. The approach is described in A.3. Looking carefully at the RHEED pattern collected from different stages of the growths, we observed some additional features and spots in RHEED patterns. Some

of the additional features indicate the appearance of potential facets of planes, identified using approaches described **in Appendix C.** RHEED is traditionally and commonly used to monitor the growth in MBE qualitatively, only to estimate growth rate and observe surface morphology during growth. However, RHEED as electron diffraction patterns can provide more information about crystal structure and orientations quantitatively, just as with TEM diffraction patterns. This investigation together with the developed script and algorithm (Appendix C.2.2) suggests an approach and method to analyze information in RHEED patterns qualitatively.

5.6 Conclusion

In summary, we have examined the influence of Ga surface saturation on the polytype selection of GaN NW ensembles during MBE on CMOS-compatible Si(001). We report on a GaN polytype selection mechanism for WZ-on-ZB NW ensembles in which high Ga surface saturation enables nucleation of ZB GaN on Si (001). We also elucidate the relative roles of Ga surface and step-edge diffusion on GaN film vs NW selection. In addition, low-temperature photoluminescence spectroscopy shows distinct excitonic transitions related to both ZB and WZ GaN, supporting a type-I ZB/WZ offset. This work provides a crucial step toward the realization of polarization-free, CMOS-compatible GaN-based optoelectronics. Further studies will focus on the structure of individual NWs as well as the influence of a wider range of growth conditions. Suggestions for future growth, with an emphasis on RHEED measurements to explore electron-beam-induced surface charging effect on ZB to WZ will be discussed in Chapter 7.2.1.

5.7 Figures

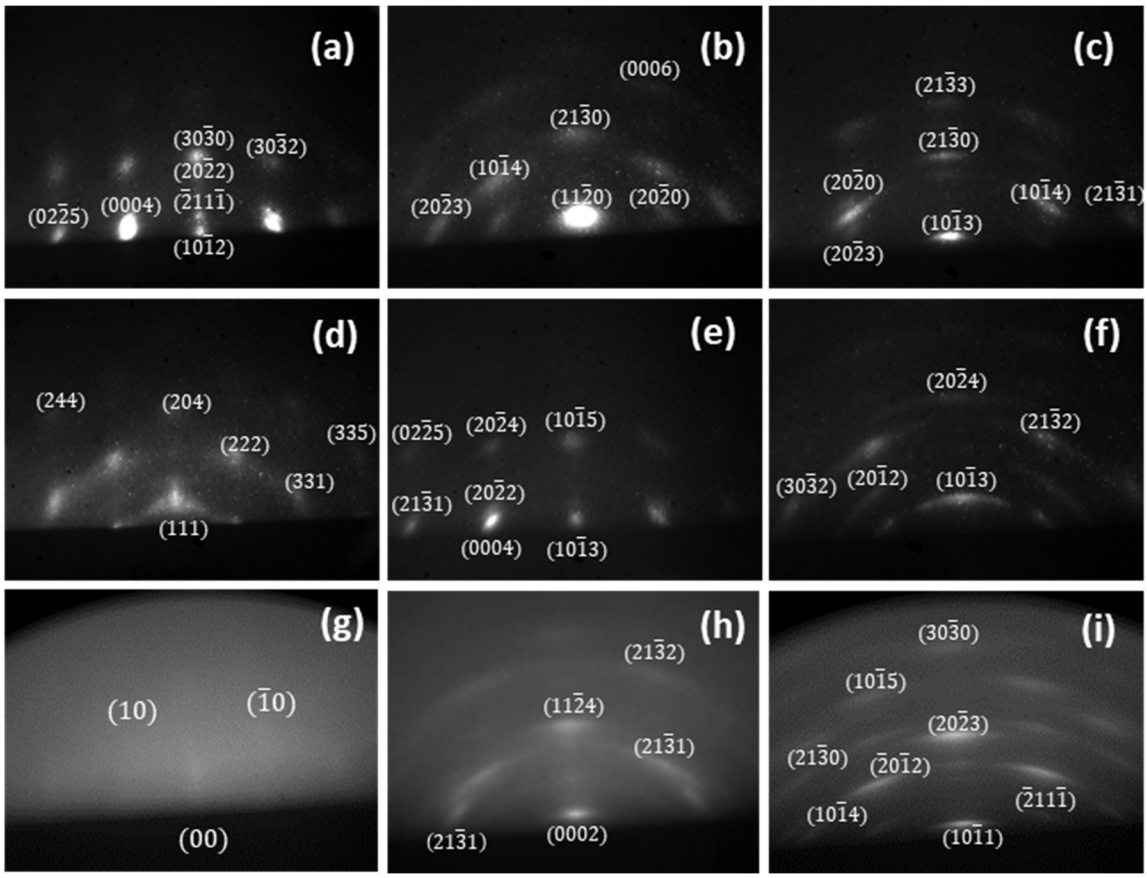

Figure 5.1 Example reflection high-energy electron diffraction (RHEED) patterns collected along the $[110]_{Si}$, $[1100]_{WZ}$, or $[110]_{ZB}$ axis for "low-low" [(a)-(c)], "high-high" [(d)-(f)], and "high-low" [(g)-(i)] series. (a)-(c) were taken 10 mins, 1hr, and 2hr into GaN growth, respectively. 4-axis Miller-Bravais indices were used for the identified hexagonal planes. (d)-(f) were taken 15 mins, 30 mins, and 2 hrs into GaN growth, respectively. 3-axis Miller indices were used for the identified cubic planes. (g)-(i) were taken 5 mins, 20 mins, and 2.5 hr into GaN. The hazy RHEED with faint Si streaks in (g) indicates Ga surface saturation and that the GaN nucleation has not taken place. 4-axis Miller-Bravais indices were used for the identified hexagonal planes of the broken rings observed in (h) and (i). (This figure is a correction to Fig 1 in Ref 50. The subfigures in Fig 1 of Ref 50 contain RHEED images with incorrect samples for intermediate stage low-low RHEED, nucleation stage high-high RHEED, and high-low RHEED patterns, which is correct in this Figure 5.1. In this figure, RHEED for RMBE 1102, RMBE 1099, RMBE 1100 are used for (a), (b), and (c) respectively to represent low-low series. RHEED for RMBE 1090, RMBE 1089, and RMBE 1095 are used for (d), (e), and (f) respectively. RHEED for RMBE 1141 is used for (g) and (i) for high-low, and RMBE 1142 is used for (h) for high-low. The list of samples details is in Table E.4.)

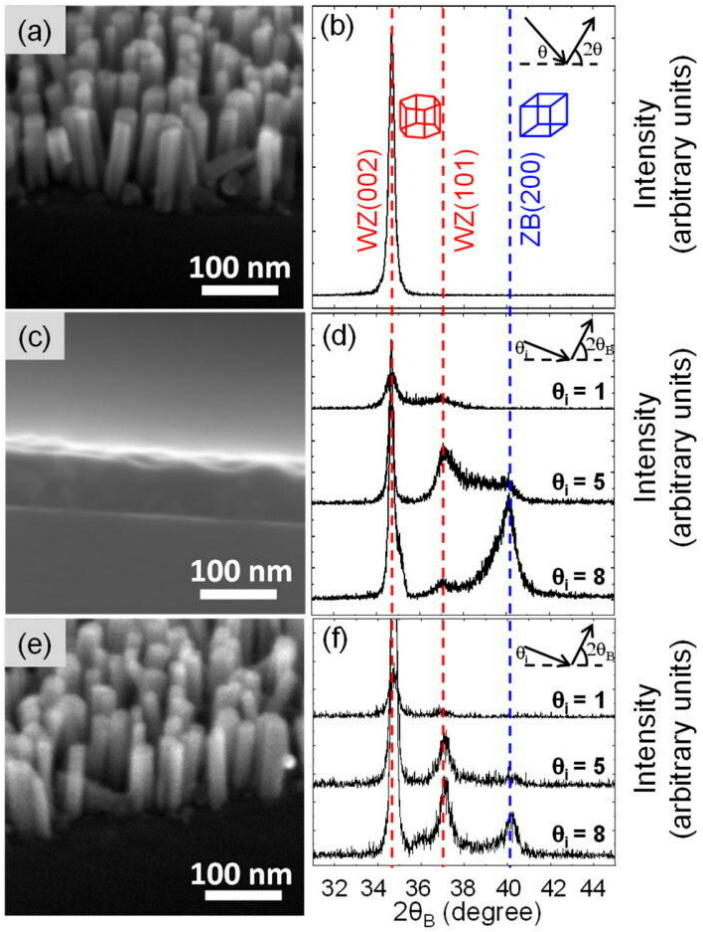

Figure 5.2 Scanning electron microscopy (SEM) images (column 1) and x-ray diffraction (XRD) spectra (column 2) for pure wurtzite (WZ) NWs [(a) and (b)], WZ-on-zinc blende (ZB) films [(c) and (d)], and WZ-on-ZB NWs [(e) and (f)]. The SEM images in (a) and (e) reveal height-independent NW diameters for the WZ and WZ-on-ZB NWs. The XRD spectra in (b) reveal the formation of pure WZ NWs, while the low-incident-beam-angle diffraction (LIBAD) spectra in (d) and (f), with incident angle $\theta_i = 1°$, 5°, and 8° corresponding to the information depths of 131, 145, and 148 nm, reveal a ZB to WZ transition at a height of 20 ± 2 nm. Reprinted figure with permission from Ref 12 (Copyright 2021, AIP Publishing).

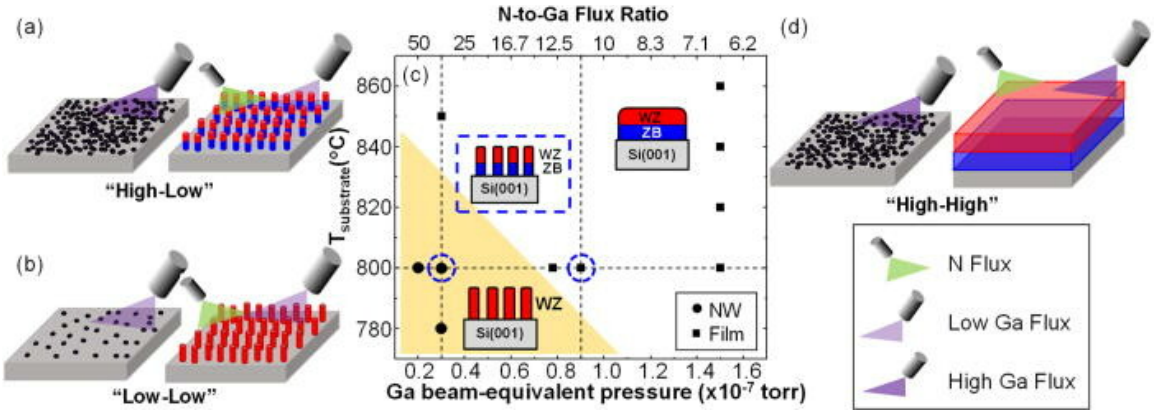

Figure 5.3 Map of GaN nanowire (NW) vs film and wurtzite (WZ) vs zinc blende (ZB) polytype selection: (c) substrate temperature vs Ga beam-equivalent pressure (with the N-to-Ga flux ratio shown on top x-axis). Schematics surrounding the plot in (c) illustrate the pre-deposition and nitridation steps for (a) WZ-on-ZB NWs, (b) WZ NWs, and (d) WZ-on-ZB films. Each position on the map represents the conditions for pre-deposition and nitridation steps, with the circle or square designation representing the film vs NW formation for fixed fluxes only. The yellow region is a guide to the eye, showing a window of conditions that are dominated by the formation of NWs. To illustrate the process for the formation of WZ-on-ZB NWs, the high and low Ga fluxes used for the pre-deposition and nitridation steps are indicated by the blue circles surrounding two positions, with the high Ga flux corresponding to that used for the pre-deposition and the low Ga flux corresponding to that used for nitridation. We hypothesize that the high Ga flux during pre-deposition enables epitaxy of ZB GaN on silicon, while the subsequent low Ga flux during nitridation facilitates nanowire formation. Reprinted figure with permission from Ref 12 (Copyright 2021, AIP Publishing).

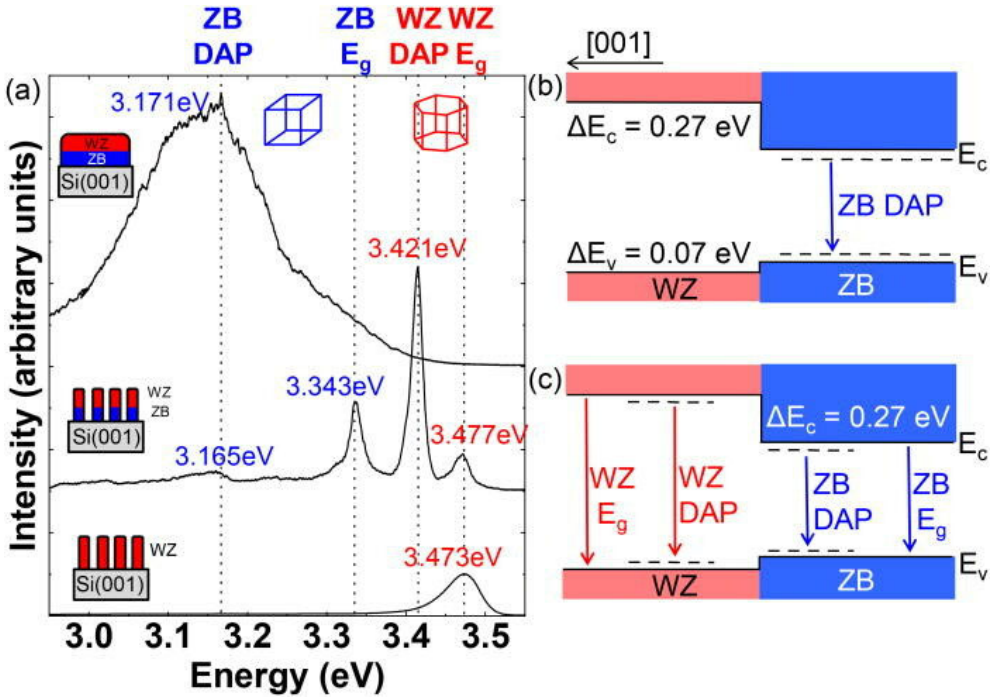

Figure 5.4 Optical properties of GaN NWs and films. (a) Photoluminescence (PL) spectra collected at 10 K for WZ GaN NWs, WZ-on-ZB GaN NWs, and WZ-on-ZB GaN films, revealing excitonic (E_g) and donor–acceptor pair (DAP) emissions for ZB and WZ GaN. The proposed type-I WZ/ZB GaN band alignment for (b) films and (c) NWs. Reprinted figure with permission from Ref 12 (Copyright 2021, AIP Publishing).

5.8 References

[1] C. Zhao, N. Alfaraj, R.C. Subedi, J.W. Liang, A.A. Alatawi, A.A. Alhamoud, M. Ebaid, M.S. Alias, T.K. Ng, and B.S. Ooi, "III-nitride nanowires on unconventional substrates: From materials to optoelectronic device applications", Prog, Quantum Electron. 61, 1 (2018).

[2] A.E. Romanov, T.J. Baker, S. Nakamura, and J.S. Speck, "Strain-induced polarization in wurtzite III-nitride semipolar layers", J. Appl. Phys. 100, 023522 (2006).

[3] S.R. Routray and T.R. Lenka, "Effect of degree of strain relaxation on polarization charges of GaN/InGaN/GaN hexagonal and triangular nanowire solar cells", Solid State Electron. 159, 142 (2019).

[4] G. Naresh-Kumar, J. Bruckbauer, A. Winkelmann, X. Yu, B. Hourahine, P.R. Edwards, T. Wang, C. Trager-Cowan, and R.W. Martin, "Determining GaN Nanowire Polarity and its Influence on Light Emission in the Scanning Electron Microscope", Nano Lett. 19, 3863 (2019).

[5] S.-H. Park and S.-L. Chuang, "Comparison of zinc-blende and wurtzite GaN semiconductors with spontaneous polarization and piezoelectric field effects", J. Appl. Phys. 87, 353 (2000).

[6] F. Bernardini, V. Fiorentini, and D. Vanderbilt, "Spontaneous polarization and piezoelectric constants of III-V nitrides", Phys. Rev. B 56, R10024 (1997).

[7] K.H. Lee, Y. Wang, B. Wang, L. Zhang, W.A. Sasangka, S.C. Goh, S. Bao, K.E. Lee, E.A. Fitzgerald, and C.S. Tan, "Monolithic Integration of Si-CMOS and III-V-on-Si Through Direct Wafer Bonding Process", IEEE J. Electron Devices Soc. 6, 571 (2018).

[8] W. Guo, M. Zhang, A. Banerjee, and P. Bhattacharya, "Catalyst-Free InGaN/GaN Nanowire Light Emitting Diodes Grown on (001) Silicon by Molecular Beam Epitaxy", Nano Lett. 10, 3355 (2010).

[9] L. Cerutti, J. Ristić, S. Fernández-Garrido, E. Calleja, A. Trampert, K.H. Ploog, S. Lazic, and J.M. Calleja, "Wurtzite GaN nanocolumns grown on Si(001) by molecular beam epitaxy", Appl. Phys. Lett. 88, 213114 (2006).

[10] J. Borysiuk, Z.R. Zytkiewicz, M. Sobanska, A. Wierzbicka, K. Klosek, K.P. Korona, P.S. Perkowska, and A. Reszka, "Growth by molecular beam epitaxy and properties of inclined GaN nanowires on Si(001) substrate", Nanotechnology 25, 135610 (2014).

[11] T. Kouno, M. Sakai, K. Kishino, and K. Hara, "Hexagonal GaN microdisk with wurtzite/zinc-blende GaN crystal phase nano-heterostructures and high quality zinc-blende GaN crystal layer", Jpn. J. Appl. Phys., Part 1 53, 068001 (2014).

[12] G. Jacopin, L. Rigutti, L. Largeau, F. Fortuna, F. Furtmayr, F.H. Julien, M. Eickhoff, and M. Tchernycheva, "Optical properties of wurtzite/zinc-blende heterostructures in GaN nanowires", J. Appl. Phys. 110, 064313 (2011).

[13] H.Y. Xu, Z. Liu, Y. Liang, Y.Y. Rao, X.T. Zhang, and S.K. Hark, "Structure and photoluminescence of wurtzite/zinc-blende heterostructure GaN nanorods", Appl. Phys. Lett. 95, 133108 (2009).

[14] K. Hestroffer, C. Leclere, C. Bougerol, H. Renevier, and B. Daudin, "Polarity of GaN nanowires grown by plasma-assisted molecular beam epitaxy on Si(111)", Phys. Rev. B 84, 245302 (2011).

[15] S. Fernández-Garrido, X. Kong, T. Gotschke, R. Calarco, L. Geelhaar, A. Trampert, and O. Brandt, "Spontaneous Nucleation and Growth of GaN Nanowires: The Fundamental Role of Crystal Polarity", Nano Lett. 12, 6119 (2012).

[16] M. de la Mata, R.R. Zamani, S. Martí-Sánchez, M. Eickhoff, Q. Xiong, A. Fontcuberta i Morral, P. Caroff, and J. Arbiol, "The Role of Polarity in Nonplanar Semiconductor Nanostructures", Nano Lett. 19, 3396 (2019).

[17] V. Consonni, M. Hanke, M. Knelangen, L. Geelhaar, A. Trampert, and H. Riechert, "Nucleation mechanisms of self-induced GaN nanowires grown on an amorphous interlayer", Phys. Rev. B 83, 035310 (2011).

[18] R.K. Debnath, R. Meijers, T. Richter, T. Stoica, R. Calarco, and H. Lüth, "Mechanism of molecular beam epitaxy growth of GaN nanowires on Si(111)", Appl. Phys. Lett. 90, 123117 (2007).

[19] V. Consonni, V.G. Dubrovskii, A. Trampert, L. Geelhaar, and H. Riechert, "Quantitative description for the growth rate of self-induced GaN nanowires", Phys. Rev. B 85, 155313 (2012).

[20] C. Chèze, L. Geelhaar, A. Trampert, and H. Riechert, "In situ investigation of self-induced GaN nanowire nucleation on Si", Appl. Phys. Lett. 97, 043101 (2010).

[21] L. Geelhaar, C. Chèze, B. Jenichen, O. Brandt, C. Pfüller, S. Münch, R. Rothemund, S. Reitzenstein, A. Forchel, T. Kehagias, P. Komninou, G.P. Dimitrakopulos, T. Karakostas, L. Lari, P.R. Chalker, M.H. Gass, and H. Riechert, "Properties of GaN Nanowires Grown by Molecular Beam Epitaxy", IEEE J. Sel. Top. Quantum Electron. 17, 878 (2011).

[22] M. Birkholz, *Thin Film Analysis by X-Ray Scattering* (Wiley-VCH, Weinheim, 2006), Chap. 4, pp. 155–158.

[23] N.S. Karan, Y. Chen, Z. Liu, and R. Beaulac, "Solution–Liquid–Solid Approach to Colloidal Indium Nitride Nanoparticles from Simple Alkylamide Precursors", Chem. Mater. 28, 5601 (2016).

[24] A. Upcher, V. Ezersky, A. Berman, and Y. Golan, "Nanometer size effects in nucleation, growth and characterization of templated CdS nanocrystal assemblies", Nanoscale 4, 7655 (2012).

[25] S.B. Lee, S.J. Yoo, K. Kim, Y.-S. Kim, Y.-M. Kim, J.-G. Kim, and H.N. Han, "Stabilization of a Ga-adlayer structure with the zincblende stacking sequence in the GaN(000−1) surface at the nanoscale", Nanoscale 9, 2596 (2017).

[26] A.W. Wood, X. Weng, Y.Q. Wang, and R.S. Goldman, "Formation mechanisms of embedded wurtzite and zincblende indium nitride nanocrystals", Appl. Phys. Lett. 99, 093108 (2011).

[27] A.W. Wood, R.R. Collino, P.T. Wang, Y.Q. Wang, and R.S. Goldman, "Formation and transformation of embedded GaN nanocrystals", Appl. Phys. Lett. 100, 203113 (2012).

[28] R. Banerjee, R. Jayakrishnan, R. Banerjee, and P. Ayyub, "Effect of the size-induced structural transformation on the band gap in CdS nanoparticles", J. Phys. Condens. Matter 12, 10647 (2000).

[29] M. Reason, N.G. Rudawski, H.A. McKay, X. Weng, W. Ye, and R.S. Goldman, "Mechanisms of GaAsN growth: Surface and step-edge diffusion", J. Appl. Phys. 101, 083520 (2007).

[30] H. Lu, C. Reese, S. Jeon, A. Sundar, Y. Fan, E. Rizzi, Y. Zhuo, L. Qi, and R.S. Goldman, "Mechanisms of GaN quantum dot formation during nitridation of Ga droplets", Appl. Phys. Lett. 116, 062107 (2020).

[31] A. Pimpinelli and J. Villain, in *Physics of Crystal Growth*, edited by C. Godréche (Cambridge University Press, Cambridge, UK, 1998), pp. 181–200.

[32] G. Ehrlich and F.G. Hudda, "Atomic View of Surface Self-Diffusion: Tungsten on Tungsten", J. Chem. Phys. 44, 1039 (1966).

[33] R.L. Schwoebel and E.J. Shipsey, "Step Motion on Crystal Surfaces", J. Appl. Phys. 37, 3682 (1966).

[34] R.K. Debnath, R. Meijers, T. Richter, T. Stoica, R. Calarco, and H. Lüth, "GaN-nanowhiskers: MBE-growth conditions and optical properties", Appl. Phys. Lett. 90, 123117 (2007).

[35] A. Wierzbicka, G. Tchutchulashvili, M. Sobanska, K. Klosek, R. Minikayev, J.Z. Domagala, J. Borysiuk, and Z.R. Zytkiewicz, "Arrangement of GaN nanowires on Si(001) substrates studied by X-ray diffraction: Importance of silicon nitride interlayer", Appl. Surf. Sci. 425, 1014 (2017).

[36] W.E. Hoke, D. Barlett, T.D. Kennedy, B. Wissman, and J.J. Mosca, "Short wavelength band edge thermometry during molecular beam epitaxial growth of GaN on SiC substrates and detected adatom self-heating effects", J. Vac. Sci. Technol. B 28, C3F5 (2010).

[37] D. Das, A. Aiello, W. Guo, and P. Bhattacharya, "InGaN/GaN Quantum Dots on Silicon with Coalesced Nanowire Buffer Layers: A Potential Technology for Visible Silicon Photonics", IEEE Trans Nanotechnol. 19, 571 (2020).

[38] V.V. Mitin, V A. Kochelap, and M.A. Stroscio, in *Quantum Heterostructures: Microelectronic and Optoelectronics* (Cambridge University Press, Cambridge, UK, 1999), Chapter 2.3, pp 15–20.

[39] M. Leszczynski, H. Teisseyre, T. Suski, I. Grzegory, M. Bockowski, J. Jun, S. Porowski, K. Pakula, J.M. Baranowski, C.T. Coxon, and T.S. Cheng, "Lattice parameters of gallium nitride", Appl. Phys. Lett. 69, 73 (1996).

[40] M.A. Reshchikov, D. Huang, F. Yun, L. He, H. Morkoç, D.C. Reynolds, S.S. Park, and K.Y. Lee, "Photoluminescence of GaN grown by molecular-beam epitaxy on a freestanding GaN template", Appl. Phys. Lett. 79, 3779 (2001).

[41] S.V. Novikov, C.T. Foxon, and A.J. Kent, "Zinc-blende (cubic) GaN bulk crystals grown by molecular beam epitaxy", Phys. Status Solidi C 8, 1439 (2011).

[42] H.-Y. Chen, H.-W. Lin, C.-H. Shen, and S. Gwo, "Structure and photoluminescence properties of epitaxially oriented GaN nanorods grown on Si(111) by plasma-assisted molecular-beam epitaxy", Appl. Phys. Lett. 89, 243105 (2006).

[43] S. Fischer, C. Wetzel, W. Walukiewicz, and E.E. Haller, in *Symposium AAA – Gallium Nitride and Related Materials: The First International Symp.*, edited by R. D. Dupuis, J. A. Edmond, S. Nakamura, and F. A. Ponce (Mater. Res. Soc. Symp. Proc., 1995), Vol. **395**, pp. 571–576.

[44] M.A. Reshchikov and H. Morkoç, "Luminescence properties of defects in GaN", J. Appl. Phys. 97, 061301 (2005).

[45] U. Strauss, H. Tews, H. Riechert, R. Averbeck, M. Schienle, B. Jobst, D. Volm, T. Streibl, B.K. Meyer, and M.W. Rühle, "Identification of a Cubic Phase in Epitaxial Layers of Predominantly Hexagonal GaN", MRS Internet J. Nitride Semicond. Res. 1, 44 (1996).

[46] T. Tingberg, T. Ive, and A. Larsson, "Investigation of Si and O Donor Impurities in Unintentionally Doped MBE-Grown GaN on SiC(0001) Substrate", J. Electron. Mater. 46, 4898 (2017).

[47] J.A. Freitas, Jr., "Pervasive Shallow Donor Impurities in GaN", ECS J. Solid State Sci. Technol. 9, 015009 (2020).

[48] A. Belabbes, L.C. de Carvalho, A. Schleife, and F. Bechstedt, "Cubic inclusions in hexagonal AlN, GaN, and InN: Electronic states", Phys. Rev. B 84, 125108 (2011).

[49] S. Ke, K. Zhang, and X. Xie, "Band line-ups and band-gap behaviour of new-type superlattices (3C-BN)/(2H-BN), (3C-GaN)/(2H-GaN) and (3C-SiC)/(2H-SiC)", J. Phys.: Condens. Matter 8, 10209 (1996).

[50] H. Lu, S. Moniri, C. Reese, S. Jeon, A. Katcher, T. Hill, H. Deng, and R.S. Goldman, "Influence of gallium surface saturation on GaN nanowire polytype selection during molecular-beam epitaxy", Appl. Phys. Lett. 119, 031601 (2021).

Chapter 6

Writing-To-Learn in Introductory Materials Science and Engineering ‡

6.1 Overview

In this chapter, we examine the impact of writing-to-learn (WTL) on promoting conceptual understanding of introductory materials science and engineering, including crystal structures, stress–strain behavior, phase diagrams, and corrosion. The background of this study is discussed in Section 6.2. The research methods are described in Section 6.3. The writing to learn implementation is described in detail in Section 6.3.1. For this study, we use writing assignments together with pre/post concept-inventory-style assessments, described in Section 6.3.2 and Section 6.3.3 respectively. The analysis for the writing products and their impact on conceptual knowledge are discussed in Section 6.4 and Section 6.5. Lastly, before summary and outlook in Section 6.7. we also examined students' perception of writing-to-learn in Section 6.6 based on students' feedbacks provided to course staff at midpoint and end of the term.

‡ This chapter is a reproduction of "Writing-to-learn in introductory materials science and engineering" (https://doi.org/10.1557/s43579-021-00114-z) by L. Marks, H. Lu, T. Chambers & R. S. Goldman. The article is licensed under a CC-BY 4.0 license (https://creativecommons.org/licenses/by/4.0/).

6.2 Background

Writing has long been used to support learning across a range of contexts and disciplines.[1,2,3] One such writing-based instructional practice, writing-to-learn (WTL), has been incorporated into classrooms in forms spanning reflective writing to long, scaffolded writing assignments. Across disciplines, WTL has been used to support instructional goals such as developing both disciplinary thinking and conceptual learning.[4,5] Within science education, WTL assignments have been used to support the development of scientific argumentation, metacognition, and conceptual understanding by students.[5,6,7] These goals are further represented in the writing assignments described in the engineering education literature.[8,9,10,11] However, only a few studies of WTL in materials science have been reported to date.[10,12] In one case, the effect of shorter in-class writing assignments on student learning within an introductory materials science course was explored.[10] In another case, we examined student responses to a context-based WTL assignment that consisted of a draft, peer review, and revision cycle, emphasizing its usage and efficacy of supporting conceptual learning of polymer properties within an introductory materials science course.[12] Here, we expand upon our prior work by considering student responses across a comprehensive set of WTL assignments spanning materials classes and functionalities. Our aim is to investigate student gains in comprehension and application of course content across a term and to inform future use of WTL in introductory materials science and engineering.

For these studies, we use a WTL process in which students apply content knowledge to "real world" situations by writing a response to a prompt conveying an authentic scenario, performing and receiving content-focused peer review, and finally revising their initial response.[13] This three-step WTL process incorporates the key elements for effective WTL assignments identified by meta-analyses of WTL literature, namely clearly defined and interactive writing

expectations that incorporate meaning-making tasks and support metacognition.[6,14,15] This WTL process also aligns with cognitive theories of learning such as social constructivism,[1,6,10,14,15] which posits that students learn within their individual social environments by restructuring existing knowledge to incorporate new knowledge.[14,15] Indeed, research has shown that this WTL process has enabled students to constructively engage with the peer review and revision processes,[16,17] thereby supporting them in learning challenging content in a wide range of introductory STEM courses, including biology, chemistry, and statistics.[12,18,19,20,21,22] Our WTL implementation also follows the principles for designing effective "writing to communicate" experiences in engineering, with writing assignments that include an authentic investigation and audience, are tied to the technical course content, and provide useful practice for engineering careers, while not being overly burdensome for the engineering faculty instructor.[23]

The core objective of an introductory materials science and engineering course is to introduce the principles of engineering materials, with an emphasis on understanding fundamental relationships between internal structure, properties, processing, and performance of materials that are essential for understanding the role of materials in the design of engineering systems.[24] Typically, these principles are framed in the context of materials classes (metals, ceramics, polymers, semiconductors, and composites), each with their characteristic chemistry and internal structure. The role of materials processing is described in terms of thermodynamics (via phase diagrams) and kinetics (via diffusion). Finally, materials functionality is introduced, with an emphasis on understanding connections between internal structure (microstructure and defects) and macroscopic properties/performance.

Here, we examine the influence of WTL assignments that incorporate both an authentic scenario and social elements in the form of peer review and revision, on student understanding of

key concepts in introductory materials science and engineering (MSE). With an emphasis on key MSE concepts, including crystal structures, stress–strain behavior, phase diagrams, and corrosion, the study is guided by the following research questions:

1. Do students' descriptions of the WTL-assignment-targeted content improve between their drafts and revisions?
2. Do students develop more robust understandings of the WTL-assignment-targeted content?
3. Which MSE learning goals are best supported by the WTL assignment design?

6.3 Methods

6.3.1 Writing to learn implementation in introductory materials science and engineering

For this study, we use two main sources of data: (1) draft and revision responses to the WTL assignments, numerically scored using a rubric generated by the research team, and (2) responses to an MSE concept-inventory-style assessment external to the required coursework given at both the beginning and the end of the course, which we term the "pre" and "post" assessments, respectively. To examine the contributions of peer review and revision to improvements in students' conceptual descriptions from draft to revision, we employed qualitative and quantitative analyses of student writing. We also used quantitative analysis of the concept-inventory-style assessment responses to compare the learning gains of students who participated in WTL with those who instead participated in a guided-group discussion intended to offer comparable content exposure. In a given term, all students completed at least two of the four WTL assignments.

This study was conducted at a midwestern university in a lower-level MSE course during three separate terms. The course consists of lecture and recitation sections with coursework

including traditional problem sets, bi-weekly reflective writing, and WTL assignments. Prerequisite courses include either general chemistry or introductory organic chemistry. The textbook for the course is "Materials Science and Engineering" by Callister and Rethwisch.[25] Across the three terms (Winter 2017, Winter 2018, and Winter 2019), the course participants consisted of 151 students who ranged from sophomores to seniors, as well as two graduate students auditing the course. Most of the students were enrolled in the College of Engineering, with more than fifty percent intending to major in Biomedical Engineering. Amongst the 120 students who completed the WTL assignments and the pre- and post- external assessments, 38 self-identified as female, 23 as non-US born, and 13 as first-generation college students.

The WTL assignments focus on concepts identified to be the most challenging for students of introductory materials science.[26,27,28,29] Each WTL assignment consists of an initial written response to a prompt ("draft"), anonymous open-response peer review performed by 2–3 randomly selected students ("peer review"), and a revision of the draft ("revision"). Peer review is guided by content-focused rubrics, as shown in the supplemental materials of Ref 30 For each WTL assignment, one week is given for the initial response and half a week for both the peer review and revision, respectively. For the draft and peer review, student scores are based upon completion, with a cursory check to verify that all prompt requirements are addressed. For the revision, student scores are based upon alignment of student responses with assignment-specific rubric criteria. Throughout each term, additional support for students is provided by two peer tutors ("Writing Fellows") familiar with introductory materials science through prior enrollment in this course or its equivalent. The writing fellows are trained to help students approach the writing assignments while learning content; they are available to facilitate the peer review process and answer both writing and content questions.

6.3.2 Writing analysis: rubrics and statistical significance

We analyzed draft and revision WTL submissions using rubrics designed to evaluate conceptual understanding by probing student ability to describe relevant course content, as shown in the supplemental materials of **Ref 30** For each WTL assignment, a rubric consisting of at least two content-specific criteria, each scored from 0 (lowest) to 4 (highest), was iteratively developed. In addition, the understandability for an audience with minimal scientific background was evaluated as an additional rubric criterion. For the rubric development process, we initially examined ~ 10% of total submissions in order to gain a general understanding of student responses, as well as to identify common mistakes and patterns in student writing and understanding. Using this analysis to develop initial rubric criteria, 20% of the student drafts and revisions were randomly selected for scoring by 3 experienced graders to determine inter-rater reliability (IRR) via percent agreement. Since a rubric with IRR $\geq$0.75 is considered to be reliable for observational data, we used an iterative process of refining the rubrics, scoring a random selection of student submissions, and re-calculation of IRR until 0.75 was achieved.[31] Once all rubrics met this reliability standard, the scoring system was considered finalized. We note that many of the rubric criteria achieved reliability of IRR $\geq$0.85, which is considered very reliable for textual analysis.[32] For subsequent analysis, every individual assignment was scored by an experienced researcher using the finalized rubric scoring system. Finally, the statistical validity of this "writing score" analysis was examined. For each rubric criteria, the draft and revision scores were fit to a normal distribution, yielding most R^2 values in excess of 0.8,[33] as shown in Table 6.1.

To quantify the statistical significance of improvements in student writing from draft to revision, we performed t-tests with a significance threshold of $\alpha = 0.05$.[34] For those criteria with $p<\alpha$, we then used Cohen's d statistic as a measure of effect size to quantify improvements in

student writing. Cohen's d is a measure of the difference in two quantities relative to their variability in the population of interest.[35] For our data, we calculated

$$d = \frac{\bar{x}_r - \bar{x}_d}{\sigma_x} \qquad \text{(Equation 6.1)}$$

where $\bar{x}_d$ and $\bar{x}_r$ are the mean draft and revision scores for a given rubric criterion, and

$$\sigma_x = \sqrt{\frac{(\sigma_r^2 + \sigma_d^2)}{2}} \qquad \text{(Equation 6.2)}$$

(where σ_r and σ_d are the standard deviations of draft and revision scores for each rubric) is the pooled standard deviation of the scores for that rubric. For each rubric criterion, the value of d is attributed to the combined effects of the peer review and revision processes. For the present analysis, we consider $d \leq 0.5$, $0.5 < d \leq 1.0$, and $d > 1.0$ to be small, medium, and large effect sizes, respectively.[35]

6.3.3 Content knowledge assessment

To probe student gains in conceptual understanding, we developed and administered an MSE concept-inventory-style assessment. Similar to the WTL assignments described above, the assessment questions focus on concepts identified to be the most challenging for students of introductory materials science.[27,28,29] Drawing from the Materials Concept Inventory,[36] the Crystal Spatial Visualization Survey,[37] and other published assessments for introductory materials science,[27] we compiled a set of candidate questions. A team of course instructors and other subject matter experts then selected items with the greatest content validity relative to course and WTL assignment topics.[38] Four of the assessment topics were also represented in WTL assignments (crystal structures, stress–strain, phase diagrams, and corrosion), while one was not (atomic bonding).

The assessment consisted of eleven three-tiered items including a conceptual question, a short answer prompt to explain reasoning, and a confidence self-rating. For the first-tier questions, the format was either multiple choice or "select all that apply." For several items, the first-tier consisted of questions with multiple parts; in our analysis, each part was scored as a separate question, resulting in 19 total conceptual questions. Preliminary analysis of second-tier responses revealed that student explanations were too brief or sporadic to inform our research; thus, these were not included in the data set. In the third tier, students were prompted to report their confidence on a 1–5 Likert scale (with 1 corresponding to the lowest confidence, and 5, the highest). Finally, during the writing of this manuscript, it was discovered that appropriate answers were not available for one of the items that consisted of 4 conceptual questions. Therefore, this paper focuses on the analysis of first-tier student responses for 15 conceptual questions.

For the analysis, we considered only the responses from students who completed both the pre- and post-assessments, including 120 students across three terms. The resulting assessment data were then categorized into three groups based on population and topic, as follows:

- **WTL Group:** students who completed the assessments and the associated WTL assignment.
- **Non-WTL Group:** students who completed the assessments but did not complete the associated WTL assignment.
- **WTL-Free Group:** all students who completed the assessments for atomic bonding and the water phase diagram (part of the phase diagrams assessment topic), which do not have an associated WTL assignment.

For both the pre- and post-assessments, the fractions of correct responses were calculated individually for each first-tier question (separated into parts, when applicable) and collectively by

assessment topic. To quantify the compounded effects on content knowledge of WTL assignments plus instruction vs. instruction alone, we calculated the statistical significance of the differences in mean fraction of correct answers from the pre- and post-assessments and the learning gains from the pre- to post-assessment. Statistical significance was calculated using McNemar's test, which is appropriate for paired dichotomous data such as before-and-after responses categorized as either correct or incorrect. The test statistic has a χ^2 distribution with one degree of freedom, enabling determination of p-values using a χ^2 table.

To gauge the efficacy of WTL in promoting conceptual understanding, we also compare the ratio of the average gain achieved by each population (WTL vs. non-WTL groups) to their maximum possible gain, i.e., the normalized gain $\langle g \rangle$[39]:

$$\langle g \rangle = \frac{\bar{x}_f - \bar{x}_i}{1 - \bar{x}_i} \qquad \text{(Equation 6.3)}$$

where $\bar{x}_i$ and $\bar{x}_f$ are the fractions of correct responses for the pre- and post-assessments, respectively. On most concept inventories, $\langle g \rangle < 0.3$ is generally considered small, $0.3 \leq \langle g \rangle < 0.7$ medium, and $\langle g \rangle \geq 0.7$ large; in traditional lecture-based courses, $\langle g \rangle < 0.3$ is typical.[39]

As part of the course, students responded to short, reflective writing questions throughout the term. The mid-term and end-of-term reflective writing questions solicited feedback on the structure of the course, including the WTL assignments. The portion of the responses specifically about the WTL assignments were examined thematically to characterize self-reported student attitudes about the assignments.[40] In total, 252 responses were examined across the three terms.

6.4 Analysis of writing products

In this section, we present the analyses of the writing products for the WTL assignments, emphasizing student performance on drafts and revisions. To identify the content knowledge and

skills for which WTL is an effective pedagogy in the context of MSE, we consider the analyses of the writing products both individually and collectively. Figure 6.1 presents bar charts of average writing scores achieved on rubric criteria for the (a) crystal structures, (b) stress–strain, (c) phase diagram, and (d) corrosion WTL assignments. For all rubric criteria, the increases between draft and revision scores are statistically significant; for most criteria, the revision scores, $\bar{x}_r > 3$ on a scale of 0–4. The consistent improvement in student responses coupled with high revision scores suggests that the peer review and revision processes guide students toward a robust level of content understanding. To further probe the role of the WTL process on student content understanding, we examine the Cohen's effect size, d.[35] As shown in Figure 6.1(a)–(d), $d > 0.5$ for all rubric criteria across WTL assignments, indicating that the peer review and revision processes contribute meaningfully to overall student understanding of course content.

For the crystal structure WTL, shown in Figure 6.1(a), medium effect sizes in the range $0.75 \leq d \leq 0.96$ are observed for all rubric criteria. The highest effect sizes are apparent for the "atomic packing" and "slip stability" rubric criteria, which emphasize the relationship between tightly packed spheres (oranges) and crystal structures, and the mechanical stability of stacked planes of spheres (oranges), respectively. The "atomic packing" rubric criterion assesses student crystal structure visualization ability, a critical skill for understanding the role of atomistic structure on macroscopic properties. The "slip stability" rubric criterion also assesses crystal structure visualization ability, while further probing student ability to recognize the differences in the distribution of forces for atoms vs. oranges.[41] It is interesting to note that the "understandability" rubric criterion, which probes the accessibility of each writing product to an audience with minimal scientific background, exhibits the lowest effect size for the crystal structure WTL. This rubric

criterion differs from the others in that it defines success by quality of communication rather than demonstrated application of technical course content.

For the stress–strain WTL, shown in Figure 6.1(b), medium-to-large effect sizes in the range $0.70 \leq d \leq 1.48$ are observed. In this case, the "macro-/micro- load response" and "$\sigma - \varepsilon$ curve before/after recycling" rubric criteria exhibit the highest effect sizes, with $d = 1.48$ and $d = 1.16$, respectively. It is interesting to note that the "macro-/micro- load response" rubric criterion assesses student ability to link polymer macroscopic properties with the microscopic configurations of their constituent molecules. Since learning to connect microscopic and macroscopic phenomena is a primary objective of many introductory materials science courses,[26] these findings motivate further implementation of this WTL assignment in such courses. Meanwhile, the "σ–ε curve before/after recycling" rubric criterion evaluates student ability to synthesize literature data into quantitative formats, namely, to construct stress–strain curves based upon numerical values of key physical parameters. Since the construction of stress–strain curves has been identified as a difficult skill for students at the introductory level,[26] these findings reveal the broad benefit of this WTL assignment to early career undergraduates. Finally, for the stress–strain WTL, the "understandability" rubric criterion once again exhibits the lowest effect size. Across WTL assignments, the emerging trend of comparatively lower effect sizes for the "understandability" rubric criterion reveals that student growth in conceptual knowledge exceeds student growth in writing ability during the revision process.

For the phase diagrams WTL, shown in Figure 6.1(c), medium effect sizes in the range $0.52 \leq d \leq 0.80$ are apparent. The "discipline-specific terminology" and "microstructure-performance relationship" rubric criteria exhibit the highest effect sizes, with $d = 0.77$ and $d = 0.80$, respectively. The medium effect size for the "discipline-specific terminology" rubric criterion,

which analyzes student ability to accurately incorporate discipline-specific terminology into writing products, reveals the benefits of applying verbal reasoning to the WTL process. Indeed, requiring students to use and explain expert-like language helps them to establish familiarity and fluency with relevant terms and concepts, leading to the development of a robust discipline-specific vocabulary. Similar to the large effect size for the "macro-/micro-load response" rubric criterion for the stress–strain WTL described above, the medium effect size for the "microstructure-performance relationship" rubric criterion, which targets student ability to relate the microstructure of solder to its macroscopic performance, further supports the implementation of WTL in introductory materials science courses. Due to these medium-to-high effect sizes, we hypothesize that the WTL process facilitates student growth in connecting microscopic structure to macroscopic properties and performance. Finally, for phase diagrams WTL, the lowest effect size is observed for the "understandability" rubric criterion, consistent with the lower student growth in writing ability during the revision process discussed above.

For the corrosion WTL, shown in Figure 6.1(d), low-to-medium effect sizes in the range $0.48 \leq d \leq 0.64$ are observed. In this case, the "understandability" rubric criterion exhibits the highest effect size amongst all WTL assignments. Furthermore, for the content-focused rubric criteria, "corrosion chemistry," "water system corrosion," and "water system upgrades," minimal variation between draft and revision scores are apparent, resulting in effect sizes of $d = 0.50$, 0.50, and 0.48, respectively. In comparison with the other WTL assignments, the relatively high effect size for the "understandability" criterion, coupled with the relatively low effect sizes for the content-focused rubric criteria, is likely due to the emphasis on declarative knowledge rather than quantitative problem-solving and micro-/macroscopic linkage. As will be discussed below, we suggest that

future iterations of the Corrosion WTL assignment include opportunities for students to make quantitative correlations between microstructure and properties.

For most WTL assignments, the lower effect sizes for the "understandability" rubric criterion provides evidence that the primary learning outcome from the WTL process is in conceptual learning and discipline-specific thinking rather than refined prose. Indeed, by committing to a concrete verbalization of thoughts during the writing and editing of drafts, and by interacting with peers during the peer review process, students are led to metacognitively engage with course content through evaluation and revision of writing products. This process enables solidification of student comprehension by enabling them to identify and address their mistakes, in alignment with the overall goals of WTL as a form of pedagogy and curriculum. To optimize these outcomes, we suggest that future WTL assignments mimic the structure of the prompts that demonstrated high effect sizes on content-focused rubric criteria (i.e., the crystal structures, stress–strain, and phase diagrams prompts) by providing guidance within assignments to help students link concepts and quantitative reasoning.

6.5 Impact of WTL on conceptual knowledge

We now present the analysis of the concept-inventory-style content assessment that was administered at the beginning and end of each term. To individually and collectively examine the normalized gains in conceptual knowledge, we consider 15 conceptual assessment items grouped by topic. As shown in Figure 6.2, the assessment topics include (a) atomic bonding, (b) crystal structures, (c) stress–strain, (d) phase diagrams, and (e) corrosion. To distinguish the datasets based upon population, the bar charts are color-coded to indicate their response group, i.e., WTL Group, Non-WTL Group, and WTL-Free Group, as described above. The comparison of scores and normalized gains, $\langle g \rangle$, across the WTL, Non-WTL, and WTL-Free Groups provides information

about the relative roles of the WTL revision process vs. other course learning opportunities in enhancing conceptual learning.

We first consider the atomic bonding topic, shown in Figure 6.2(a), which is not currently represented by a corresponding WTL assignment. For this topic, the relationships between the shape of potential energy curves and materials properties are probed. As shown in the bar chart in Figure 6.2(a), small-to-medium statistically significant gains of $\langle g \rangle \geq 0.20$ are apparent for all four bonding items. The highest gains were obtained for "melting point," "elastic modulus," and "lattice parameter" items with $\langle g \rangle = 0.51$, 0.44, and 0.40, respectively, exceeding gains of $\langle g \rangle = 0.30$ anticipated for traditional lecture-based courses.[39]

For the crystal structures topic, all students completed the associated WTL assignment. As shown in the bar chart in Figure 6.2(b), for three of the four crystal structure items, small-to medium gains of $\langle g \rangle \geq 0.29$ are apparent. The highest gains were obtained for the "identify (100) FCC plane" and "identify (110) FCC plane" items, with $\langle g \rangle = 0.59$ and 0.38, respectively, both exceeding expectations for traditional lecture-based courses. On the other hand, lower gains—albeit statistically significant—were obtained for the "selection of close-packed plane" item, namely $\langle g \rangle = 0.29$, within the expected gains for a traditional lecture-based course. Finally, for the "identifying (111) FCC plane" item, gains of $\langle g \rangle = 0.09$ were observed. These findings are consistent with earlier reports revealing student misconceptions about the atomic configurations within the (111) FCC plane.[42] Interestingly, in an earlier study of learning gains in a traditional introductory MSE course (without WTL), the "identifying (111) FCC plane" item yielded $\langle g \rangle = 0.02$, approximately one-fourth of our gain.[37] While our data set is not large enough to establish statistical significance for the difference in these gains, the comparison suggests that WTL is effective in helping students overcome stubborn misconceptions about planes in FCC structures.

Next, we consider the stress–strain topic, with "polymer stress–strain" and "metal yield strength" shown in the bar chart in Figure 6.2(c). For the stress–strain topic, small-to medium gains of $\langle g \rangle \geq 0.29$ are apparent for the WTL group, while statistically insignificant gains of $\langle g \rangle \leq 0.13$ are observed for the non-WTL group. As discussed above, the stress–strain WTL requires students to link polymer macroscopic properties with the microscopic behavior of their constituent molecules. The stress–strain WTL also requires students to distill tabulated stress–strain data into quantitative stress–strain plots. Since the ability to interpret quantitative and qualitative stress–strain data was critical for the "polymer stress–strain" and "metal yield strength" items, the reinforcement of these skills through the stress–strain WTL has evidently led to higher scores for the WTL group. As will be further illustrated for the corrosion topic below, the difference in gains between the WTL and non-WTL groups indicate that WTL assignments have enhanced student abilities to extrapolate and critically apply course content beyond the capabilities acquired from a traditional lecture-based course in isolation. This is likely not simply a function of time-on-task, as non-WTL groups covered the same content in discussion sections instead of completing WTL assignments.

Figure 6.2(d) presents the average scores for the phase diagrams topic, including the "label phase," "identify liquidus," and water phase diagram" items. For the "water phase diagram" item, which is not represented by a corresponding WTL assignment, negligible gains are observed. Although pressure–volume phase diagrams are briefly discussed in lectures and readings, they are not included in conventional homework; therefore, the negligible gains are not surprising. For the "label phase diagram" and "identify liquidus" items, both the WTL and non-WTL groups achieved statistically significant normalized gains, all with $\langle g \rangle > 0.55$, as shown in Figure 6.2(d). We attribute this result to robust classroom instruction and rigorous (non-writing) homework assignments on binary phase diagrams. These high gains may also be explained by the extended emphasis on

binary phase diagrams, with an allocation of approximately 1.5 weeks during a 14-week term. The similarity of these gains may also be attributed to the content of the two binary phase diagrams assessment items, which both emphasize declarative knowledge rather than deep microstructural analysis skills developed throughout the WTL process. Therefore, for future assessment iterations, we suggest an added emphasis on microstructure-focused analysis of binary phase diagrams in order to better understand the efficacy of the binary phase diagrams WTL assignment in enhancing conceptual learning.

Finally, for the corrosion topic, the average scores of the "corrosion reaction" and "corrosion prevention" items are shown in the bar charts in Figure 6.2(e). In this case, small-to-medium gains are observed for the WTL group, while negligible gains are apparent for the non-WTL group. For the "corrosion reaction" item, which emphasizes equation recognition and manipulation, the WTL group achieved a medium gain of $\langle g \rangle = 0.50$, while for the "corrosion prevention" item, which emphasizes declarative knowledge, the WTL group achieved a small gain of $\langle g \rangle = 0.16$. The relatively low pre-test score for the "corrosion reaction" item ($\bar{x}_i = 0.31$) suggests that students had limited pre-course familiarity with the relationships between oxidation, reduction, and corrosion. Subsequent student exposure to oxidation and reduction reactions from lectures, readings, and conventional homework, combined with the interpretation of the reactions in the corrosion WTL assignment, likely provided sufficient time-on-task for recall. Finally, the lower gains for the "corrosion prevention" item reveals that further student growth may require the corrosion WTL assignment to facilitate more extensive connections between microstructure and macroscopic properties.

Across assessment topics, the normalized gains for the WTL group exceed those of the non-WTL group. This difference in gains implies the presence of an additional source of learning

beyond that of the traditional course components including lectures, recitations, homework, and exams. Given that this course employs traditional didactic pedagogy outside of the WTL component, we attribute the large gains to the learning acquired by engaging with the WTL process. In particular, we hypothesize that student ability to extrapolate and critically apply course content has been enhanced by participation in the entire WTL process, including draft writing, peer review, and revision.

6.6 Student perceptions of writing-to-learn

To examine student perceptions of WTL, we gathered feedback about all course elements, including the WTL assignments, at the midpoint and end of the term. For this analysis, we characterized self-reported textual input on learning and attitudes. Approximately half of the students report that the WTL assignments enhanced their learning, ranging from gaining a better understanding of the content to developing their writing ability. Over a third of the students discussed the benefits of the WTL assignments in supporting their conceptual understanding. While most of the responses were general, some students specified that the assignments reinforced, solidified, or deepened their understanding of both fundamental and complex concepts. Students identified that having to explain the targeted concepts allowed them to assess their own understanding and think more deeply about the content.

Many students discussed the role of the authentic scenarios of the WTL assignments in supporting their learning. In particular, many students mentioned that the authentic scenarios allowed them to apply the concepts they were learning in class, which in turn supported both their understanding of the material and its importance. Additionally, authentic scenarios may play a role in the affective aspects of learning, as evidenced by some students who discussed how it made the content more interesting and made them feel like engineers.

A small subset of the responses touched upon incorporating writing into a materials science course. In these responses, students demonstrated mixed attitudes towards writing, but the majority discussed appreciating the opportunity to develop their writing skills in the context of the WTL assignments. Similarly, student responses were mixed with respect to the peer review and revision elements of the assignments, which some students identified as helpful components and others did not.

Overall, student feedback responses provide additional evidence that the WTL assignments supported student learning. Broadly, students reported perceived learning gains from the WTL assignments, including the draft, peer review, and revision components. The authentic context successfully engaged students and led them to think more deeply about the targeted content. Additionally, for a subset of students, peer review and revision were perceived to be beneficial. These findings align with prior research on WTL in organic chemistry,[17,43] for which students similarly reported perceived learning benefits from engaging in writing, in particular discussing the beneficial roles of authentic contexts and peer review in supporting their learning.

6.7 Summary and outlook

In summary, we have evaluated the effectiveness of WTL assignments and their impact on student learning of foundational concepts in introductory MSE, especially those identified to be the most challenging. Using analyses of writing products in comparison with concept-inventory-style assessments, we addressed the following research questions: (1) do student descriptions of the targeted concepts improve from WTL assignment draft to revision? (2) do students develop a more robust understanding of those concepts? and (3) which learning goals are best supported by the WTL approach? For all WTL topics, student concept descriptions improved from draft to revision, while students also developed a more robust understanding of those concepts. To identify

the learning goals that are best supported by the WTL approach, we compare the WTL effect sizes and assessment normalized gains across topics.

For the stress-strain and phase diagram WTL assignments that require students to synthesize qualitative data into quantitative formats while emphasizing the connection between microscopic structure and macroscopic performance, the highest WTL effect sizes and medium-to-high gains on the corresponding assessment topics are observed. On the other hand, for the crystal structure and corrosion WTL assignments that emphasize crystal structure visualization and declarative knowledge, respectively, medium WTL effect sizes and low-to-medium gains on the corresponding assessment topics are apparent. Since crystal structure visualization is a critical skill for understanding the influence of atomistic structure on macroscopic properties and the microstructure of materials plays a central role in corrosion mitigation, we suggest that future iterations of these and other WTL assignments resemble the stress–strain and phase diagram WTL assignments by including opportunities for students to identify meaningful structure–property correlations while providing a rigorous problem-solving scaffolding for processing and contextualizing quantitative data.

Our findings suggest that WTL pedagogies enhance student learning of concepts across multiple length-scales, including correlations between microscopic structure and macroscopic performance. Such multi-scale structure–property correlations are critical for several MSE-related fields, including chemistry, physics, mechanical engineering, and civil engineering. Our findings also indicate that WTL pedagogies enhance the ability of students to synthesize qualitative data into quantitative formats, a critical skill for STEM-related fields and beyond. Taken together, these findings suggest that WTL pedagogies are likely to enhance student learning in STEM-related fields and beyond.

Finally, during recent course offerings (Winter 2020, Spring 2020, Winter 2021, and Spring 2021) not included in this study, an additional intervention from the Writing Fellows was added. For all draft submissions (following the peer review stage), Writing Fellows provide rigorous written feedback to the students. This additional intervention provides a scaffolded review process in which students receive directed feedback and reinforcement on how to better align with assignment expectations and goals. The effects of this additional intervention on student learning are currently under investigation.

6.8 Tables

Topic and rubric	N	$\bar{x}_d$	σ_d	R_d^2	$\bar{x}_r$	σ_r	R_r^2
Crystal Structure	140						
Slip Stability		2.26	0.94	0.81	2.89	0.75	0.67
Atomic Packing		2.00	1.01	0.92	3.21	0.87	0.84
Understandability		1.34	1.14	0.93	2.30	0.80	0.97
Stress-Strain	125						
Macro-/Micro-load response		2.70	0.89	0.94	3.28	0.70	0.94
Curve before/after recycling		2.84	0.79	0.97	3.35	0.63	0.95
Argument for recycled HDPE		2.71	0.81	0.94	3.47	0.53	0.99
Accurate Summary		2.74	0.79	0.99	3.54	0.55	0.92
Understandability		2.49	1.00	0.99	3.68	0.52	0.92
Phase Diagrams	120						
Microstructure performance		2.43	0.84	0.41	2.85	0.80	0.90
Melting T		2.31	0.71	0.82	2.89	0.82	0.89
Phase fractions		2.11	0.79	0.99	2.72	0.82	0.94
Discipline-specific terminology		2.18	0.87	0.98	2.75	0.88	0.98
Understandability		1.96	1.16	0.95	2.77	0.83	0.98
Corrosion	113						
Water system upgrades		2.13	0.80	0.86	2.65	0.82	0.98
Corrosion Prevention		1.99	0.91	0.99	2.43	0.85	0.94
Corrosion Chemistry		1.95	0.85	0.86	2.35	0.77	0.96
Understandability		2.58	0.97	0.96	3.02	0.87	0.96

Table 6.1 Analysis of writing-score datasets by topics and rubrics. N is the number of participants. Each dataset has been fit to a normal distribution, yielding mean draft and revisions scores ($\bar{x}_d$, $\bar{x}_r$) and standard deviations of the draft and revision scores (σ_d, σ_r), with R^2 values primarily exceeding 0.8.

Topic and Item	N	$\bar{x}_i$	$\bar{x}_f$	χ^2	p	⟨g⟩
WTL group						
Crystal Structure	120					
Identify (100) FCC Plane		0.73	0.89	12.44	<0.05	0.59
Identify (110) FCC Plane		0.17	0.48	28.88	<0.05	0.38
Identify (111) FCC Plane		0.35	0.41	1.00	0.32	0.09
Close-Packed Planes		0.37	0.55	7.12	<0.05	0.29
Stress-Strain	108					
Polymer Stress-Strain		0.45	0.62	7.37	<0.05	0.32
Metal Yield Strength		0.20	0.43	16.00	<0.05	0.29
Phase Diagrams	102					
Label Phase		0.32	0.83	46.00	<0.05	0.75
Identify Liquidus T		0.32	0.70	27.65	<0.05	0.55
Corrosion	102					
Corrosion Reaction		0.31	0.66	22.27	<0.05	0.50
Corrosion Prevention		0.20	0.18	13.76	<0.05	0.16
Non-WTL group						
Stress-Strain	12					
Polymer Stress-Strain		0.27	0.36	0.14	0.71	0.13
Metal Yield Strength		0.09	0.18	1.00	0.32	0.10
Phase Diagrams	18					
Label Phase		0.39	0.94	9.00	<0.05	0.91
Identify Liquidus T		0.33	0.72	3.00	<0.05	0.58
Corrosion	18					
Corrosion Reaction		0.44	0.44	0.00	1.00	0.00
Corrosion Prevention		0.06	0.17	0.33	0.56	0.18
WTL-free group						
Atomic Bonding	12					
Lattice Parameter		0.39	0.63	14.25	<0.05	0.40
Elastic Modulus		0.48	0.71	11.95	<0.05	0.44
Melting Point		0.56	0.78	12.36	<0.05	0.51
Thermal Expansion		0.50	0.60	2.48	<0.05	0.20
Phase Diagrams	18					
Water Phase Diagram		0.53	0.55	2.00	0.16	0.04

Table 6.2 Assessment data by topic and item for the WTL, non-WTL, and WTL-free groups. N is the number of participants for each topic, $\bar{x}_i$ and $\bar{x}_f$ are the mean fraction of correct answers for

each item from the pre- and post- assessments, χ^2 is the McNemar statistic, p indicates the statistical significance of changes from pre- to post- scores, and $\langle g \rangle$ is the normalized gain from pre- to post- scores.

6.9 Figures

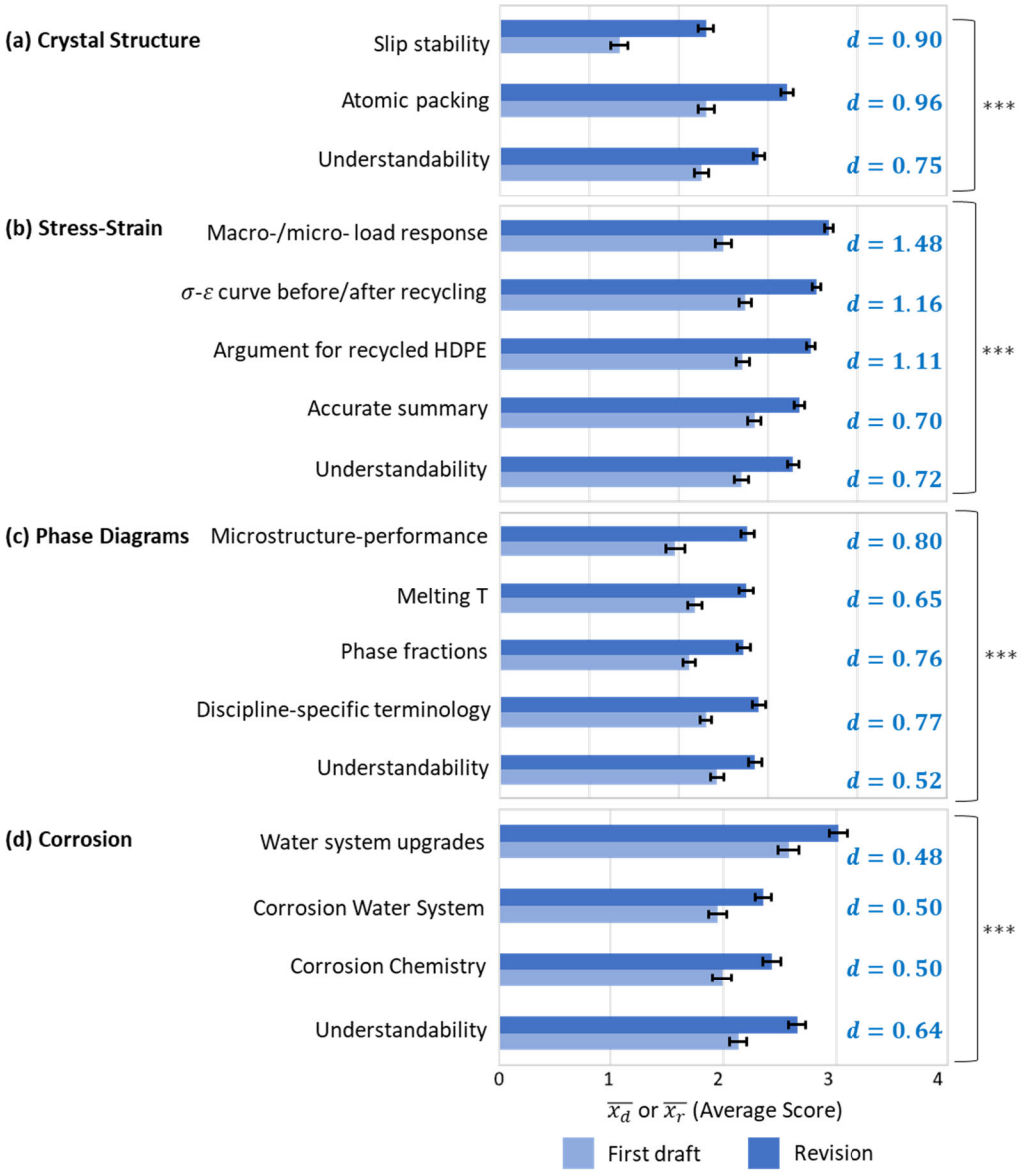

Figure 6.1 Bar charts of mean writing scores on rubric criteria for the (a) crystal structure (N = 140), (b) stress-strain (N = 123), (c) phase diagrams (N = 119), and (d) corrosion (N = 114) WTL prompts. For each rubric criterion, student writing was scored on a scale from 0 (lowest) to 4 (highest). All writing-score data sets were fit to a normal distribution, most with $R^2 > 0.8$, as shown in 0. To quantify improvements in student writing, Cohen's d values were computed; those d-values with a significance threshold of $p<0.05$ are shown next to each item. Error bars represent the standard deviations of the means. *** indicates $p<0.001$.

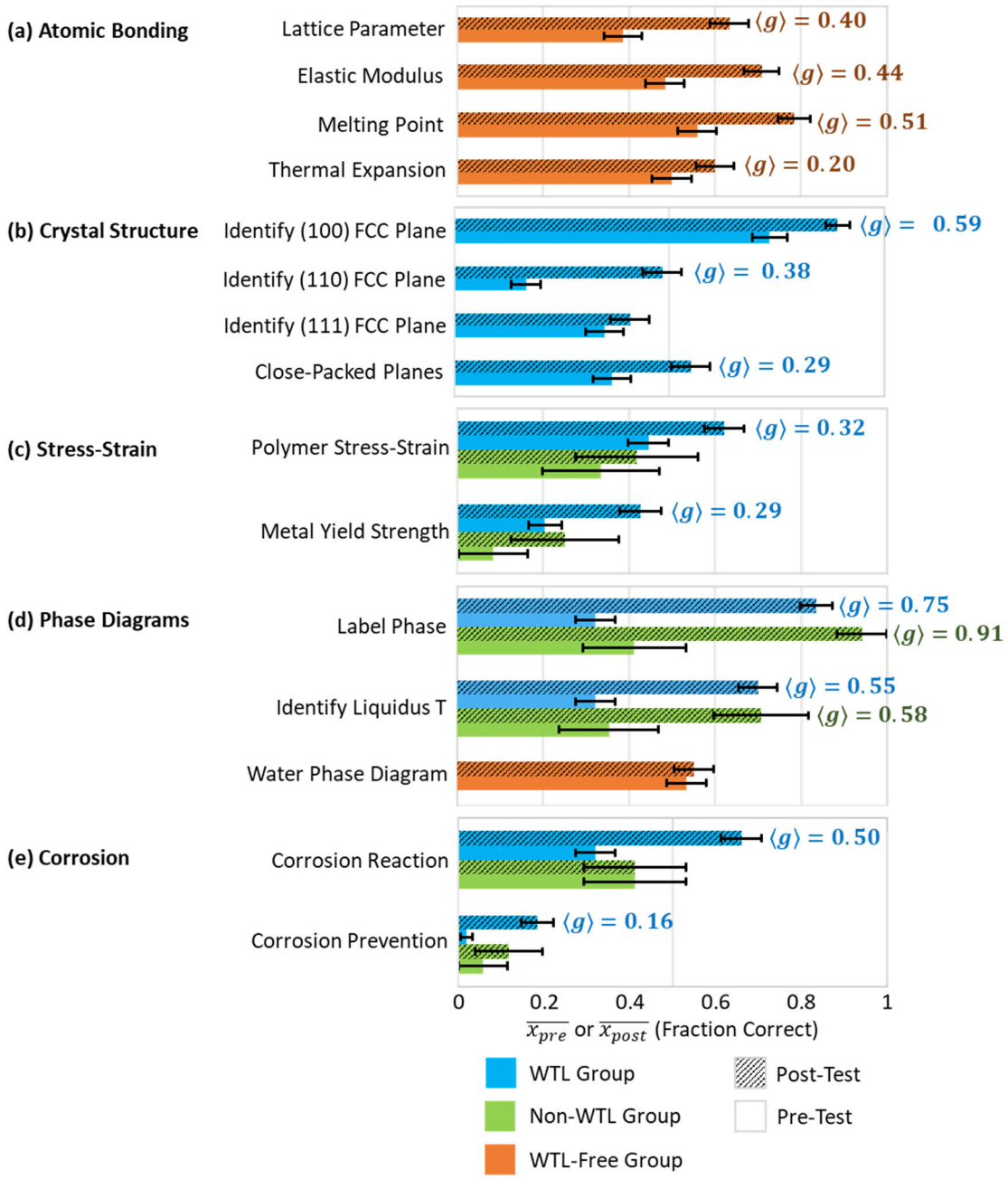

Figure 6.2 Pre- and post-assessment average item scores grouped by student group (WTL vs. non-WTL vs. WTL-free) and by topic: (a) atomic bonding, (b) crystal structure, (c) stress-strain, (d) phase diagrams, and (e) corrosion. Statistically significant ($p<0.05$) normalized gain values, $\langle g \rangle$, i.e., the ratio of the average gain achieved by a population to their maximum possible gain, were used to gauge the efficacy of a WTL in promoting conceptual understanding. Error bars represent standard error in scores. More details on the population and distribution of scores are available in Table 6.2.

6.10 References

[1] P.D. Klein, P. Boscolo, "Trends in research on writing as learning activity", Journal of Writing Research 7, 311 (2016).

[2] J. Emig, "Writing as a mode of learning", Coll. Compos. Commun. 28, 122 (1977).

[3] D. Galbraith, "Conditions for discovery through writing", Instr. Sci. 21, 45 (1992).

[4] P.D. Klein, N. Arcon, S. Baker, in Writing to learn, ed. by C.A. MacArthur, S. Graham, J. Fitzgerald. Handbook of Writing Research, 2nd edn. (The Guilford Press, New York, 2015).

[5] L.P. Rivard, "A review of writing to learn in science: implications for practice and research", J. Res. Sci. Teach. 31, 969 (1994).

[6] A.R. Gere, N. Limlamai, E. Wilson, K. MacDougall Saylor, R. Pugh, "Writing and conceptual learning in science: an analysis of assignments", Writ. Commun. 36, 99 (2019).

[7] J.A. Reynolds, C. Thaiss, W. Katkin, R.J. Thompson, "Writing-to-learn in undergraduate science education: a community-based, conceptually driven approach", CBE Life Sci. Educ. 11, 17 (2012).

[8] J.H. Hanson, J.M. Williams, "Using writing assignments to improve self-assessment and communication skills in an engineering statics course", J. Eng. Educ. 97, 515 (2008).

[9] E. Wheeler, R.L. McDonald, "Writing in engineering courses", J. Eng. Educ. 89, 481 (2000).

[10] D. Ridgway, V.L. Young, and K.J. Sampson, "Applying a writing to learn strategy in a traditional materials science and engineering course", Proceedings of the 2005 American Society for Engineering Education Annual Conference & Exposition, pp. 10.211.1–10.211.7 (2005).

[11] J. Bylander, M. Gustafsson, "Improved content mastery and written communication through a lab-report assignment with peer review: an example from a quantum engineering course", Eur. Phys. Soc. 42, 025701 (2021).

[12] S.A. Finkenstaedt-Quinn, A.S. Halim, T.G. Chambers, A. Moon, R.S. Goldman, A.R. Gere, G.V. Shultz, "Investigation of the influence of a writing-to-learn assignment on student understanding of polymer properties", J. Chem. Educ. 94, 1610 (2017).

[13] S.A. Finkenstaedt-Quinn, M.N. Petterson, A. Gere, G. Shultz, "The Praxis of writing-to-learn: a model for the design and propagation of writing-to-learn in STEM", J. Chem. Educ. 98, 1548 (2021).

[14] R.L. Ferguson, Constructivism and social constructivism. in G.M. Bodner, & M. Orgill (Eds.), Theoretical Frameworks for Research in Chemistry/Science Education, (pp. 28–49, Prentice Hall Series in Educational Innovation) (Pearson Prentice Hall, Upper Saddle River, 2007).

[15] G.M. Bodner, "Constructivism: a theory of knowledge", J. Chem. Educ. 63, 873 (1986).

[16] S.A. Finkenstaedt-Quinn, N. Polakowski, B. Gunderson, G.V. Shultz, A.R. Gere, "Utilizing peer review and revision in STEM to support the development of conceptual knowledge through writing", Writ. Commun. 38, 351 (2021).

[17] T. Gupte, F.M. Watts, J.A. Schmidt-McCormack, I. Zaimi, A.R. Gere, G.V. Shultz, "Students' meaningful learning experiences from participating in organic chemistry writing-to-learn activities", Chem. Educ. Res. Pract. 22, 396–414 (2021).

[18] S.A. Finkenstaedt-Quinn, A.S. Halim, G. Kasner, C.A. Wilhelm, A. Moon, A.R. Gere, G.V. Shultz, "Capturing student conceptions of thermodynamics and kinetics using writing", Chem. Educ. Res. Pract. 21, 922 (2020).

[19] A. Moon, E. Zotos, S. Finkenstaedt-Quinn, A.R. Gere, G. Shultz, "Investigation of the role of writing-to-learn in promoting student understanding of light–matter interactions", Chem. Educ. Res. Pract. 19, 807 (2018).

[20] J.A. Schmidt-McCormack, J.A. Judge, K. Spahr, E. Yang, R. Pugh, A. Karlin, A.R. Gere, G.V. Shultz, "Analysis of the role of a writing-to-learn assignment in student understanding of organic acid–base concepts", Chem. Educ. Res. Pract. 20, 383 (2019).

[21] S.A. Finkenstaedt-Quinn, E.P. Snyder-White, M.C. Connor, A.R. Gere, G.V. Shultz, "Characterizing peer review comments and revision from a writing-to-learn assignment focused on Lewis structures" J. Chem. Educ. 96, 227 (2019).

[22] F.M. Watts, J.A. Schmidt-McCormack, C.A. Wilhelm, A. Karlin, A. Sattar, B.C. Thompson, A.R. Gere, G.V. Shultz, "What students write about when students write about mechanisms: analysis of features present in students' written descriptions of an organic reaction mechanism", Chem. Educ. Res. Pract. 21, 1148 (2020).

[23] S.M. Lord, "Integrating effective 'writing to communicate'' experiences in engineering courses: guidelines and examples", Int. J. Eng. Ed. 25, 196 (2009).

[24] S. Krause, J. Kelly, A. Tasooji, J. Corkins, D. Baker, S. Purzer, "Effect of pedagogy on conceptual change in an introductory materials science course", Int. J. Eng. Ed. 26, 869 (2010).

[25] W.D. Callister, D.G. Rethwisch, Materials Science and Engineering: An Introduction, 9th edn. (Wiley, Hoboken, 2014).

[26] S. Krause, J.C. Decker, J. Niska, T. Alford, Identifying student misconceptions in introductory materials engineering classes. American Society for Engineering Education Annual Conference & Exposition pp. 8.648.1 (2003).

[27] A.F. Heckler, R. Rosenblatt, "Student difficulties with basic concepts in introductory materials science engineering", 2011 Frontiers in Education (FIE) Conference, pp. S2H-1 (2011).

[28] A.F. Heckler, R. Rosenblatt, "Student understanding of atomic bonds and their relation to mechanical properties of metals in an introductory materials science engineering course" in 2020 proceedings of the Annual Conference of the American Society of Engineering Education, pp. 15.1124.1.

[29] R. Rosenblatt, A.F. Heckler, "Student understanding of the mechanical properties of metals in an introductory materials science engineering course" in 2010 Proceedings of the Annual Conference of the American Society of Engineering Education, pp. 15.1126.1.

[30] L. Marks, H. Lu, T. Chambers, and R.S. Goldman, "Writing-to-learn in introductory materials science and engineering", MRS Commun. 12, 1 (2022).

[31] D.V. Cicchetti, "Guidelines, criteria, and rules of thumb for evaluating normed and standardized assessment instruments in psychology", Psychol. Assess. 6, 284 (1994).

[32] K.A. Hallgren, "Computing inter-rater reliability for observational data: an overview and tutorial", Tutor. Quant. Methods Psychol. 8, 23 (2012).

[33] W.W. Chin, B.L. Marcolin, P.R. Newsted, "A partial least squares latent variable modeling approach for measuring interaction effects: results from a monte carlo simulation study and an electronic-mail emotion/adoption study", Inf. Syst. Res. 14, 189 (2003).

[34] C.H. Brase, C.P. Brase, Hypothesis testing. in Understandable Statistics: Concepts and Methods, 10th edn (Brooks/Cole Cengage Learning, Boston, 2012).

[35] J. Cohen, in The effect size index: d. Statistical Power Analysis for the Behavioral Sciences (2nd ed.) (Lawrence Erlbaum Associates, New York, 1988).

[36] J. Corkins, J. Kelly, D. Baker, S. Robinson Kurpius, A. Tasooji, S. Krause, Determining the factor structure of the materials-concept inventory. In 2009 American Society for Engineering Education Annual Conference & Exposition, pp. 14.436.1.

[37] S.J. Krause, A. Sterling, J.E. Kelly, D. Stehlik, O. Isaacs-Sodeye, D.R. Baker, Development of a crystal spatial visualization survey for introductory materials classes. in 2012 American Society for Engineering Education Annual Conference & Exposition, pp. 25.449.1.

[38] S.N. Haynes, D.C.S. Richard, E.S. Kubany, "Content validity in psychological assessments: a functional approach to concepts and methods", Psychol. Assess. 7, 238 (1995).

[39] R.R. Hake, "Interactive-engagement versus traditional methods: a six-thousand-student survey of mechanics test data for introductory physics courses", Am. J. Phys. 66, 64 (1998).

[40] V. Braun, V. Clarke, "Using thematic analysis in psychology", *Qual Res. Psychol*. **3**, 77 (2006).

[41] S. Heitkam, W. Drenckhan, J. Forhlich, "Packing spheres tightly: influence of mechanical stability on close-packed sphere structures", Phys. Rev. Lett. 108, 148302 (2012).

[42] J. Kelley, K. Heinert, J. Triplett, D. Baker, S. Krause, Uncovering and repairing atomic bonding misconceptions with multimodal assessment of student understanding in an introductory materials course. In 2010 American Society for Engineering Education Annual Conference & Exposition, pp. 15.1289.1–15.1289.16.

[43] M.N. Petterson, S.A. Finkenstaedt-Quinn, A.R. Gere, G.V. Shultz, "The role of authentic contexts and social elements in supporting organic chemistry students' interactions with Writing-to-Learn Assignments", Chem. Educ. Res. Pract. 23, 189 (2022).

Chapter 7

Summary and Suggestions for Future Work

7.1 Summary

In this thesis, the mechanisms for nanoscale GaN and InN epitaxy and polytype selection in liquid-metal mediated environments as well as the study of writing-to-learn in Materials Science and Engineering are presented. In this chapter, a summary of the results is presented followed by suggestions for future work.

In Chapter 3, the formation mechanisms of GaN quantum dots during nitridation of Ga droplets was examined. We consider the temperature- and substrate-dependence of the size distributions of droplets and QDs, as well as the relative roles of Ga/N diffusivity and GaN nucleation rates on QD formation. We also report on two competing mechanisms mediated by Ga surface diffusion, namely, QD formation at or away from pre-existing Ga droplets. On silica surfaces, coarsening-dominant growth leads to coalescence of Ga droplets and, consequently, larger hemispherically-shaped QDs at high nitridation temperatures. At low temperatures, due to the limited Ga diffusion length, QDs form between Ga droplets. On Si(001) and Si(111) surfaces, nucleation-dominant growth leads to smaller QDs as GaN QDs can nucleate anywhere on the surface. These insights provide an opportunity for tailoring QD size distributions and polytype selection for a wide range of III-N semiconductor QDs.

In Chapter 4, environmental transmission electron microscopy (ETEM) studies of nitridation of In droplets was investigated. In this work, we report on the In droplet deposition via MBE on Si(001) single crystal TEM film and the subsequent nitridation of In droplets in ETEM. In ETEM, we observed temperature-dependent nanoparticle size increase as well as the formation of moiré pattern, suggesting the nucleation of crystalline materials during the nitridation process. The crystal lattice spacings are further examined using conventional TEM. This observation can provide insight into the transformation of indium nanoparticles into InN.

In Chapter 5, the influence of Ga surface saturation on the polytype selection of GaN NW ensembles during MBE on CMOS-compatible Si(001) was examined. We report on a GaN polytype selection mechanism for WZ-on-ZB NW ensembles in which high Ga surface saturation enables nucleation of ZB GaN on Si (001). We also elucidate the relative roles of Ga surface and step-edge diffusion on GaN film vs NW selection. In addition, low-temperature photoluminescence spectroscopy shows distinct excitonic transitions related to both ZB and WZ GaN, supporting a type-I ZB/WZ offset. This work provides a crucial step toward the realization of polarization-free, CMOS-compatible GaN-based optoelectronics. Further studies will focus on the structure of individual NWs as well as the influence of a wider range of growth conditions.

In Chapter 6, WTL pedagogies were studied. Enhancement in student learning of concepts that span multiple length scales, including correlations between microscopic structure and macroscopic performance, was observed. Such multi-scale structure–property correlations are critical for several MSE-related fields, including chemistry, physics, mechanical engineering, and civil engineering. The findings also indicate that WTL pedagogies enhance the ability of students to synthesize qualitative data into quantitative formats, a critical skill for STEM-related fields and

beyond. Taken together, these findings suggest that WTL pedagogies are likely to enhance student learning in STEM-related fields and beyond.

7.2 Suggestion for future work

7.2.1 Electron-beam-induced surface charging effect on ZB to WZ transition

In Chapter 5, we described the mechanisms for NW to film transition and polytype selection. We also discussed RHEED study of GaN NW grown by Veeco plasma source and GaN growth, although with no nanowire formation, using addon nitrogen plasma source, with the aim to reestablish GaN NW growth conditions. The difference and history of the two plasma sources (Addon and Veeco) are described in Section 2.2.2. We also discussed an approach to examine RHEED patterns in detail. Further work is necessary to GaN NWs with selective NW growth and transformation between ZB and WZ. Here I make growth suggestions for future growth, with an emphasis on using RHEED as both an e-beam source that could potentially induce surface charging effect and quantitative observation for crystal structure transition during growth.

An interesting observation of the WZ to ZB transition in both films and NWs is that the transition from ZB to WZ occurs at approximately the same depth. Therefore, the transition is not likely due to a random event but may instead be due to heating and/or electrostatic charging of the growth surface by the gallium furnace, the N plasma source, and/or the RHEED source. RHEED can be used to qualitatively review the surface morphology during the growth process. It can also be used to quantitatively study the crystal orientations during growth. Appendix E summarizes analyzed RHEED pattern and the corresponding planes of RHEED patterns discussed in Chapter 5, as well as additional RHEED patterns of WZ NWs, WZ-on-ZB films, and WZ-on-ZB NWs.

In our current growths, most of the recorded RHEED were taken during the nucleation stage (first 5 mins of the 3-hour growth). The intention to use RHEED is to observe and confirm

the nucleation of GaN. RHEED is often recorded again around 20 mins of the growth to observe and confirm the further NW growth. After 30 mins, RHEED was collected only sporadically to check on the NW growth. Incidentally, our current observations of ZB to WZ transition are also within the first 30 mins of growths. Electron beam-induced transformations of phase, defects, and morphologies have been reported in perovskite systems such as $CsPbX_3$,[1,2] 2D materials such as single layer $MoTe_2$,[3] and Co NW.[4] To explore further the electron-beam-induced surface charging effect on polytype transitions in MBE, I suggest that future growth begin with involving deliberate exposure of RHEED at specific times during growth and for longer duration. Specifically, longer (> 5 mins) RHEED videos captures can be taken every 15 mins, to observe any changes in polytypes during growth and experiment the effect of electrostatic charging from RHEED of the growth surface on polytype selection. The additional RHEED pattern collected, can also be used to develop machine-learning approach using convolutional neural networks to quantify and classify RHEED patterns.[5] To re-establish ZB/WZ NW growth condition using Riber plasma source, the specific growth plan is described in Table 7.1.

7.2.2 InN nanoparticle droplet epitaxy

In Chapter 4, I presented the study of InN in-situ TEM study of InN under ETEM at the center for functional nanomaterials (CFN) at Brookhaven National Lab. For future work, droplet epitaxy on In NP TEM samples that vary in In NP density and size can be studied further. It is also predicted that ZB polytype may be thermodynamically favored due to its lower surface/interface energies[6] that result from the changes of surface stoichiometry,[7] structures,[8] and polarization.[9,10] We observe a higher number of ZB nucleation from small particles and WZ nucleation from larger particles. Such polytype nucleation observed in large and small nanoparticles can be useful as input for simulation for ultra-small crystallites in Ga/In-rich environments (inside or at solid-liquid

interfaces of liquid Ga/In droplets). In Chapter 4, we also discussed unintentional indium oxide formation on the surface of InN QDs due to the 99.5% purity of ammonia used for the ETEM in our study and the lack of oxygen filters in the gas lines. For future experiments, to suppress oxidation of InN QDs, we can consider using higher ammonia purity (99.999%) if available or with an addition of oxygen filters in the gas lines.

7.2.3 RHEED video and pattern analysis

A detailed analysis approach is described in Chapter 5. The complete script and walkthrough are included in A.3. This approach can be used to refine growth plan by including the RHEED exposure time (when it is taken) and duration (for how long the electron was exposed to the substate) to consider the effect of electrostatic charging of the growth surface on the polytype selection. Furthermore, we can develop a machine-learning approach to quantify and classify RHEED patterns using this detailed analysis method. Last but not least, we can also make the script more user friendly and efficient by including the following user interface features:

- Drag box of region of interest (around a spot)
- A drag-bar to adjust brightness threshold.
- List of distances and ratio-square table
- Easy interactive comparison between the measured list and theoretical table

7.2.4 Nextnano simulations WZ/ZB/WZ band offset

Nextnano is a Schrödinger-Poisson-current solver and simulates quantum wells, quantum wires, and quantum dots. The conduction/valance band edge energy is taken from a material database provided by nextnano. Nextnano allows user to define variables either from the database provided by nextnano or use user-defined variables. A typical nextnano input file contains the

following components: variable definition, setup for simulation methods, setup for simulation regions and materials (within user defined region), setup for simulation model, and setup for output folders and files.

An illustration of the conduction and valence band offsets at the GaN WZ/ZB and ZB/WZ interfaces using band parameters and conduction and valence band offset for ZB[11] and WZ[12,13] in the nextnano database as plotted in Figure 7.1. To improve the accuracy of calculated bandgap values at room temperatures, Varshni fitting parameters, β and γ, were added, which describe the temperature-dependence of the conduction and valence band edges given in the following equation:[14]

$$\mathrm{E_g}(T) = E_g(0) - \frac{\gamma T^2}{T + \beta} \qquad \text{(Equation 7.1)}$$

A list of parameters and their references used to plot Figure 7.1 is in Table E.7. For future work regarding nextnano simulation, we can expand simulations of the band structure to include Schrödinger-Poisson simulations based upon the 8-band k·p approximation and incorporate findings from ongoing TEM by colleagues and future GaN and InN TEM study into Nextnano simulation.

7.2.5 Incorporation of boron in GaN

The alloys of BN with Al, In, or Ga provide an opportunity to adjust the lattice parameters and simultaneously change the electronic bandgap, as well as the integration of 2D materials, into classical semiconductor technology, in combination with metal and oxide to form of complementary metal-oxide-semiconductors (CMOS). To date, we have developed system design of the precursor borazine ($H_6B_3N_3$), a colorless liquid with an evaporation point below 0°C.[15] The design involves a small (5ml to 10ml) glass tube with an attached UHV flange to be mounted

directly to an existing UHV system and will be equipped with a detachable Peltier-cooler (to be identified) to keep molecules refrigerated for storage. The gaseous precursor borazine will be dosed to the UHV chamber via a leak valve. For future work and goals after finalizing and implementing the system design, we can use iterative feedback between growth,[16,17] structure,[18] and optical properties[19] to examine growth of B(Al)GaN alloys using plasma-assisted molecular-beam epitaxy with a borazine source for B. Furthermore, we can identify suitable growth conditions for planar alloys, with feedback from x-ray diffraction and ion beam analysis, using the combined computational-experimental approach.[20]

7.2.6 Carburization of aluminum-titanium alloy

There is an urgent need for a lightweight, thermally stable material that can be produced economically with minimal disruptions to existing manufacturing infrastructure[21]. Aluminum alloys are used extensively in the automotive and aerospace industries to meet this need, mainly because of their high strength-to-weight ratio. Further strength improvements can be achieved through the incorporation of nanosized particles in the aluminum matrix, i.e., the formation of an aluminum nanocomposite.[22,23] For example, the samples have been prepared with mini-melter using gas bubbled into the melt with a rotating impeller.[24,25]

$$N_2 + \text{melted Al} \rightarrow \text{AlN}$$

$$CH_4 + \text{melted Al (pre-alloy with Ti)} \rightarrow \text{TiC}$$

The advantage of such a process is its uniform distribution and clean interface, with no additional process for fabricating nanoparticles. However, the optimization of the process parameters involves consideration of the effect from temperature, gas flow rate, and impeller rotating speed, as well as the size, morphology, crystallinity, and distribution of the crystals. Thus, the

fundamentals of such effects need to be understood. The goal of studying this is to elucidate the role of Al_3Ti in the reaction. For this purpose, MBE, a deposition technique in a temperature-controlled, high-purity nitrogen atmosphere, is an excellent tool for studying the fundamentals of nucleation and growth. In addition, with RHEED, in-situ monitoring of crystallite nucleation and growth at an interface is possible, because the diffraction pattern shows the evolving crystal structure. For example, As shown in Figure 7.2(b), the diffuse RHEED signal observed during heating of the Al-5wt%Li alloy suggests the presence of an amorphous, liquid metal surface. As shown in Figure 7.2(c), following exposure to nitrogen, ring patterns appear, suggesting the nucleation and growth of a polycrystalline phase at the gas-liquid interface.

For future work and experiments, testing of the carbon source and the installation of Ti source to high temperature effusion cells is needed. We plan to prepare substrates for carburization using pulsed-laser deposition of various AlTi alloys and observe real-time carburization of aluminum-titanium alloys by varying the conditions for alloy melting and carburization. Following the growth, studies of ex-situ characterization of evolution of the molten alloy surfaces using X-ray Diffraction (XRD), SEM, EDS, and Auger spectroscopy can be performed.

7.2.7 Writing fellow intervention study

In Chapter 7, we studied the effect of WTL on introductory materials science and engineering course from the following terms (Spring 2016, Winter 2017, Winter 2018, and Winter 2019). Since Winter 2020, additional support for students is provided by two peer tutors ("Writing Fellows") familiar with introductory materials science through prior enrollment in this course or its equivalent. The writing fellows are trained by the MWrite program to help students approach the writing assignments while learning content; they are available to facilitate the peer review process and answer both writing and content questions. During recent course offerings (Winter

2020, Spring 2020, Winter 2021, and Spring 2021), an additional intervention from the Writing Fellows was added. For all draft submissions (following the peer review stage), Writing Fellows provide rigorous written feedback to the students. This additional intervention provides a scaffolded review process in which students receive directed feedback and reinforcement on how to better align with assignment expectations and goals.[26,27] The effects of this additional intervention on student learning are currently under investigation.

For future work, researchers can start with grading above-mentioned semesters with WF intervention—Winter 2020, Spring 2020, Winter 2021, Spring 2021, Winter 2022, and Winter 2023—based on existing research rubrics used in the published research and listed in supplemental materials of Ref. 28, then analyze pre-post scores of these semesters. Bar charts for writing analysis and pre-post test scores can be used to compare with our published WTL studies to study the effects of this additional intervention on student learning are currently under investigation.

7.3 Tables

Step	Growth Details
Outgas 35 mins.	• In buffer chamber heating station • T_{HS}=180°C
Oxide desorption 10 min.	• T_{SUB} = 800 °C (T_{CAR} ~ 890 ºC)
Ga pre-deposition 3 min.	• T_{SUB} = 800 °C (calibrated to oxide desorb temperature) • Ga shutter open • Ga BEP at 3E-8 (1st sample) and 1.5E-7 (2nd sample) • Collect RHEED for the entire duration. Close RHEED shutter when not collecting RHEED.
Interruption 3 min.	• T_{SUB} = 800 °C (calibrated to oxide desorb temperature) • All shutters close. Ramp Ga temperature.
NW growth 3 hr.	• N shutter open • MFC = 0.35 • Power = 350 W • Plasma mode: high brightness • Ga shutter open • Ga BEP at 7.6E-9 (1st sample) and 3.0E-8 (2nd sample) • N flux at 2.7E-8 (1st sample) and 1.0E-6 (2nd sample) • T_{SUB} = 800 ºC • Collecting RHEED for 5 mins every 15 mins. Close RHEED shutter when not collecting RHEED.

Table 7.1 Growth suggestion to re-establish ZB/WZ NW growth conditions using Riber plasma source. The intention is to test ranges of different high-low combinations, while keeping N/Ga ratio ≥ 33. Both conditions are chosen as a variable of previous growth attempts, described in Appendix E, where GaN films (but not NWs) are observed, keeping N/Ga ratio ≥ 33 and High/Low ratio ≈ 5, a condition that had successfully resulted in NW with Veeco plasma source. Since the Addon plasma has not been fully test for nitride growth, the suggested growths intend to explore different values of nitrogen flux, while keeping N/Ga≈33 to establish desired nitrogen plasma source condition. Intentional collection of RHEED patterns and explicit guidance on when RHEED shutter should be opened is also included.

7.4 Figures

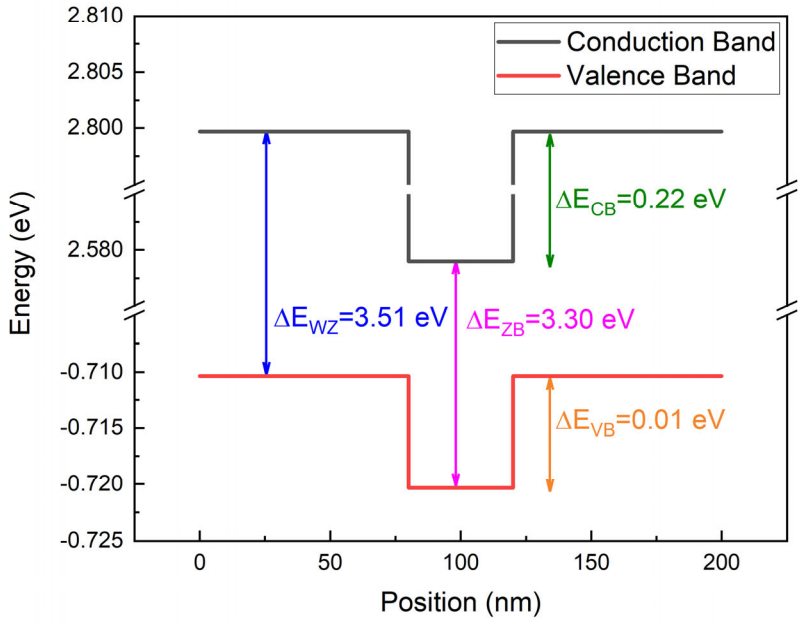

Figure 7.1 Illustration of the conduction and valence band offsets at the GaN WZ/ZB and ZB/WZ interfaces with parameters listed in Table E.7. To improve the accuracy of calculated bandgap values at room temperatures, Varshni fitting parameters, β and γ, were added, which describe the temperature-dependence of the conduction and valence band edges.

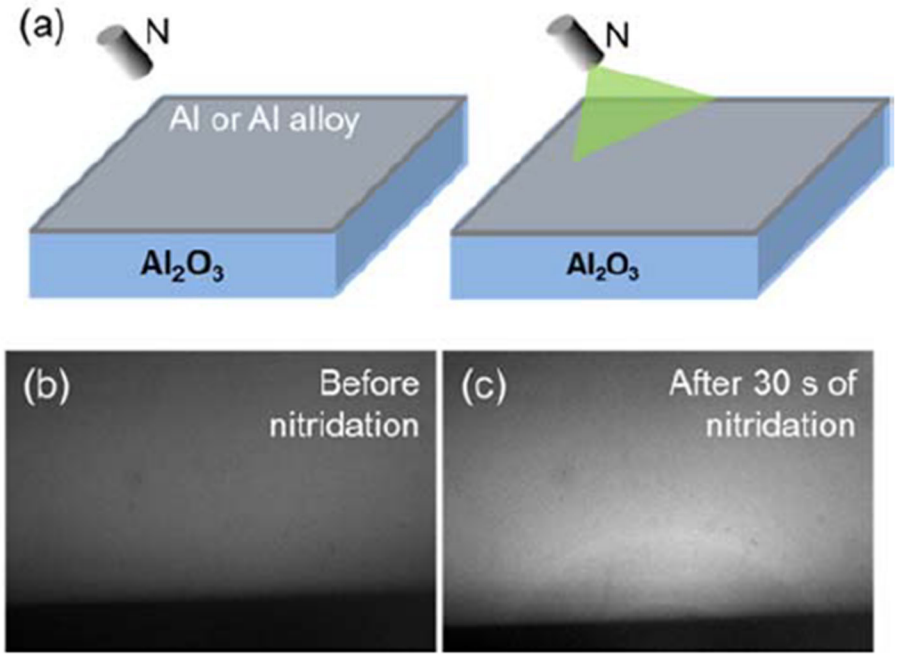

Figure 7.2 (a) Schematic diagram of the nitridation experiment for Al-5wt%Li alloy on alumina substrate. The alloy is heated above the melting temperature (left) and subsequently exposed to nitrogen (right). (b) Diffuse RHEED signal from the (above melting temperature) heated surface, suggesting the presence of a molten alloy (c) RHEED pattern collected during nitridation of the molten alloy, with rings suggesting polycrystalline growth. This experiment and RHEED is done by Dr. Caleb Reese.

7.5 Reference

[1] Z. Dang, J. Shamsi, Q.A. Akkerman, M. Imran, G. Bertoni, R. Brescia, and L. Manna, "Low-Temperature Electron Beam-Induced Transformations of Cesium Lead Halide Perovskite Nanocrystals", ACS Omega. 2, 5660 (2017).

[2] Z. Dang, Y. Luo, Y. Xu, P. Gao, and X-S Wang, "Transformation and degradation of metal halide perovskites induced by energetic electrons and their practical implications" Nano Futures. 5, 032001 (2021).

[3] J. Köster, M. Ghorbani-Asl, H-P Komsa, T. Lehnert, S. Kretschmer, A.V. Krasheninnikov, and U. Kaiser, "Defect Agglomeration and Electron-Beam-Induced Local-Phase Transformations in Single-Layer MoTe2", J. Phys. Chem. C, 125, 13601 (2021).

[4] S.H. Huh, and A. Nakajima, "Electron-beam-induced surface quasimelting of Co granular nanowires", Appl. Phys. Lett. 85, 6149 (2004).

[5] J. Kwoen and Y. Arakawa, "Classification of Reflection High-Energy Electron Diffraction Pattern Using Machine Learning", Cryst. Growth Design. 20, 5289 (2020).

[6] Y. Haneda, T. Akiyama, K. Nakamura, T. Ito, "Theoretical investigations for zinc blende–wurtzite polytypism in GaAs layers at Au/GaAs(111) interfaces", Appl. Surf. Sci. 254, 7746 (2008).

[7] D. Schikora, M. Hankeln, D. J. As, K. Lischka, T. Litz, A. Waag, T. Buhrow, and F. Henneberger, "Epitaxial growth and optical transitions of cubic GaN films", Phys. Rev. B 54, R8381R (1996).

[8] M. Hjort, S. Lehmann, J. Knutsson, A.A. Zakharov, Y.A. Du, S. Sakong, R. Timm, G. Nylund, E. Lundgren, P. Kratzer, K.A. Dick, and A. Mikkelsen, "Electronic and Structural Differences between Wurtzite and Zinc Blende InAs Nanowire Surfaces: Experiment and Theory", ACS Nano, 8, 12346 (2014).

[9] L. Li, L. Jin, J. Wang, D.J. Smith, W-J Yin, Y. Yan, H. Sang, W.C.H. Choy, M.R. McCartney, "Polarization-Induced Charge Distribution at Homogeneous Zincblende/Wurtzite Heterostructural Junctions in ZnSe Nanobelts", Adv. Mater. 24, 1328 (2012).

[10] D. Spirkoska, A.L. Efros, W.R.L. Lambrecht, T. Cheiwchanchamnangij, A.F i Morral, and G. Abstreiter, "Valence band structure of polytypic zinc-blende/wurtzite GaAs nanowires probed by polarization-dependent photoluminescence", Phys. Rev. B. 85, 045309 (2012).

[11] S-H Park and S-L Chuang, "Comparison of zinc-blende and wurtzite GaN semiconductors with spontaneous polarization and piezoelectric field effects", J. Appl. Phys. 87, 353 (2000).

[12] S-H. Park, "Crystal Orientation Effects on Electronic Properties of Wurtzite GaN/AlGaN Quantum Wells with Spontaneous and Piezoelectric Polarization", Jpn. J. Appl. Phys. 39 3478 (2000).

[13] X.W. Zhang and J.B. Xia, "Optical properties of GaN wurtzite quantum wires", J. Phys.: Condens. Matter 18 3107 (2006).

[14] M.A. Al Humayun, A.Z. Alam, S. Khan, M. AbdulMalek, and M.A. Rashid, "A Comparative Analysis of Effect of Temperature On Band-Gap Energy Of Gallium Nitride And Its Stability Beyond Room Temperature Using Bose–Einstein Model and Varshni's Model." IIUM Engineering Journal, 18, 151 (2017).

[15] W. Shen, M. Li, Y. Li, and S. Wang, "Theoretical study of borazine and its derivatives", Inorg. Chim. Acta. 360, 619 (2007).

[16] R.C. Cramer, B. Bonef, J. English, C.E. Dreyer, C.G. Van de Walle, and J.S. Speck, "Growth of coherent BGaN films using BBr3 gas as a boron source in plasma assisted molecular beam epitaxy", J. Vac. Sci. Technol., A. 35, 041509 (2017).

[17] K. Ebara, K. Mochizuki, Y. Inoue, T. Aoki, K. Kojima, S.F. Chichibu, and T. Nakano, "Impact of growth temperature on the structural properties of BGaN films grown by metal-organic vapor phase epitaxy using trimethylboron", Jpn. J. Appl. Phys. 58, SC1042 (2019).

[18] E.B. Mozdzynska, S. Złotnik, P. Ciepielewski, J. Gaca, M. Wojcik, P.P. Michałowski, K. Rosinski, K. Pietak, M. Rudzinski, E. Jezierska, and J.M. Baranowski, "Insights on boron impact on structural characteristics in epitaxially grown BGaN", J Mater Sci. 57, 7265 (2022).

[19] A. Kadys, J. Mickevičius, T. Malinauskas, J. Jurkevičius, M. Kolenda, S. Stanionytė, D. Dobrovolskas, and G. Tamulaitis, "Optical and structural properties of BGaN layers grown on different substrates", J. Phys. D: Appl. Phys. 48, 465307 (2015).

[20] L. Lymperakis, "Ab-initio study of boron incorporation and compositional limits at GaN and AlN (0001) surfaces", Aip Advances 8, 065301 (2018).

[21] F. Tang, B.Q. Han, M. Hagiwara, and J.M. Schoenung, "Tensile Properties of a Nanostructured Al-5083/SiC_p Composite at Elevated Temperatures", Adv. Eng. Mater. 9, 286 (2007).

[22] Y. Flom, and R. Arsenault, "Interfacial bond strength in an aluminium alloy 6061—SiC composite," Materials Science and Engineering, 77, 191 (1986).

[23] V. Nardone, and K. Prewo, "On the strength of discontinuous silicon carbide reinforced aluminum composites", Scr. Metall. 20, 4 (1986).

[24] I. Anza, PhD Thesis, "Synthesis of Aluminum-Titanium Carbide Nanocomposites by the Rotating Impeller Gas-Liquid In Situ Method," Worchester Polytechnic Institute (2016)

[25] I. Anza, and M.M. Mahklouf, "Synthesis of Al-TiC Nanocomposites by an In-Situ Gas-Liquid Method", Light Met. 2016, pp 245-254 (Springer 2016).

[26] E. Hall, and B. Hughes, "Preparing faculty, professionalizing fellows: Keys to success with undergraduate writing fellows in WAC", The WAC Journal. 22, 2 (2011).

[27] D.R. Regaignon and P. Bromley, "What Difference Do Writing Fellows Programs Make?" The WAC Journal. 22, 41 (2011).

[28] L. Marks, H. Lu, T. Chambers, and R.S. Goldman, “Writing-to-learn in introductory materials science and engineering”, MRS Commun. 12, 1 (2022).

Appendices

Appendix A Experimental Procedures and Data

A.1 Introduction

This appendix describes the experimental procedure used in this thesis. Section A.2 describes the ignition process of addon nitrogen plasma source described in Chapter 2. Section A.3 describes the GaN growth procedure post the replacement of Veeco plasma source described in Chapter 5. Section A.4 describes the dendrite cleaning procedure on the surface of the GaN samples.

A.2 Ignition process of addon nitrogen plasma sources

For the Addon plasma source, a three-step ignition process is used.

Step 1. **"low brightness ignition":** In this step, the MFC is set to 1.5 sccm and the forward power is raised to 350W, while the reflected power is minimized. The resulting "low brightness" plasma exhibits a dim orange color. If the low brightness (orange) plasma is not ignited at 350W, the flow rate is increased to 1.5 to 2.0 sccm. If the "low brightness" is still not ignited, the forward power is increased to 400 to 450W, while the reflected power is again minimized. Typically, the "low brightness" (orange) plasma is ignited at 350 to 400W, with a flow rate of 1.5 sccm.

Step 2. **"medium brightness ignition":** In this step, the MFC flow rate is increased to 3 sccm and the forward power is increased toward 500W, while the reflected power is

reduced, until the plasma color transforms from dim orange to dim purple. Typically, this transition happens for forward power <500W.

Step 3. **"high brightness ignition":** In this step, the forward power is increased to 500W, and the MFC flow rate is lowered to 1 sccm at 0.1 sccm/sec, and then to <1 sccm at 0.02 sccm/sec until the plasma turns purple at ~0.35 sccm.

We note that in the Addon source, the plasma is often unstable for 156 MFC > 0.35 sccm. If the plasma is extinguished during the flow rate lowering process, one must restart the process form the "low brightness ignition" step.

A.3 GaN sample growth after the replacement of Veeco plasma source and XRD observations

As mentioned in Section 2.2.2, following the above-mentioned growth of samples studied in Chapter 3 and Chapter 5, the Veeco source was accidentally powered without water cooling, rendering it nonfunctional. Subsequently, the water flow safety interlock was re-installed, and a "spare" Addon RF plasma source, originally intended to be installed on the Riber 32 MBE, was installed on the Gen II. Attempts and growth recipe is under investigation to successfully achieve GaN nanowire growth with Addon RF plasma source. For such growths, 3" Si (001) substrates mounted on In-free blocks were used. In preparation for epitaxy, silicon substrates were etched in a 5% HF solution for 45 s, mounted on In-free blocks, and pre-baked at 180°C for 1 hour in the load-lock. Each substrate was then transferred into the molecular-beam epitaxy (MBE) growth chamber, and the substrate temperature was increased until 960°C when the reflection high-energy electron diffraction pattern transformed from a diffuse (1 × 1) to a streaky (2 × 1) pattern, considered to be the surface oxide desorption temperature, 880 ºC. Following oxide desorption, Ga pre-deposition step was performed using Ga beam-equivalent-pressure (BEP) of 3.0×10^{-8} for

3 min, in the absence of N ("Ga pre-deposition"). Following Ga pre-deposition step, Ga cell temperature was ramped down to 848 ºC from 907 ºC with N plasma source open. The ramp down process took 4 mins. GaN growth step was performed using Ga BEP of 7.6×10^{-9} for 3 hours with N plasma source open. For the nitridation step (Ga surface saturation in the presence of N), the N_2 flow rate/plasma power were held at 1.0 sccm/350 W for 3 hours, resulting in a N flux of 2.7×10^{-7} Torr, as determined by the partial pressure of 14 amu with a residual gas analyzer. For both steps, the substrate temperature was fixed at 800°C. The Ga BEP was chosen such that N/III ratio is equal to 35, which was hypothesized to lead to GaN NW growth. XRD scans ranges from 32.9°–33.0°, 33.6°–34.7°, 36.7°–37.2°, and 39.8°–40.3° were used to verify the presence of WZ($10\bar{1}0$), WZ(0002), WZ($10\bar{1}1$), and ZB(200), respectively, in the sample. From the XRD scans, only WZ GaN($10\bar{1}0$) were observed, as shown in Figure A.2. A chart of d-spacing and 2 theta for GaN XRD is included in Table F.1 and Table F.2.

A.4 Dendrites and cleaning procedure

Following the attempted growth of GaN NWs, dendrites were observed by SEM on the surface of the sample. We consider the hydrocarbon from the SEM may be a potential source of contamination. The dendrite on the surface of GaN was successfully removed following solvent cleaning procedure. Following the cleaning procedures outlined in this section, dendrites were successfully removed (shown in Figure A.1).

Step 1. Wash the beaker and petri dish using water and glassware soap, then dry them using a lint-free wipe.

Step 2. Fill the clean 40 mL beaker with about 25-30 mL of trichloroethylene (TCE) and place the sample inside, film side up. Place the clean petri dish lid over the beaker to reduce TCE evaporation.

Step 3. Place the beaker in the ultrasonic cleaner, making sure the water bath level is slightly lower than the TCE level, and turn on the ultrasonic cleaner. Place a lint-free disposable wipe on a benchtop to create a clean working surface.

Step 4. After six minutes, remove the beaker from the ultrasonic cleaner and place it on top of the lint-free disposable wipe. Remove the sample from the TCE and place it film side up on the lint free wipe.

Step 5. Discard the used TCE in an appropriate waste container.

Step 6. Fill the clean 40 mL beaker with about 25-30 mL of acetone and place the sample inside, film side up.

Step 7. Place the beaker in the ultrasonic cleaner, making sure the water bath level is slightly lower than the acetone level, and turn on the ultrasonic cleaner. Place the clean petri dish lid over the beaker to reduce acetone evaporation.

Step 8. After six minutes, remove the beaker from the ultrasonic cleaner and place it on top of the lint-free disposable wipe. Keeping the sample submerged in acetone, pick it up with clean tweezers. Remove the sample from the acetone while spraying it with IPA using the squeeze bottle to rinse the surface and prevent the formation of an acetone film. Discard the used acetone/IPA in an appropriate waste container.

Step 9. Fill the clean 40 mL beaker with about 25–30 mL of IPA and place the sample inside, film side up. Place the beaker in the ultrasonic cleaner, making sure the water bath level is slightly lower than the IPA level, and turn on the ultrasonic cleaner. Place the clean petri dish lid over the beaker to reduce IPA evaporation.

Step 10. After six minutes, remove the beaker from the ultrasonic cleaner and place it on top of the lint-free disposable wipe.

Step 11. Remove the sample from the IPA while spraying it with IPA using the squeeze bottle to rinse the surface and dispose of the used IPA in an appropriate waste container. Place the sample film-side-up on the lint-free disposable wipe and allow to air-dry. Dispose of the IPA in an appropriate waste container.

Step 12. Once the sample is fully dried, place it in the clean petri dish and cover it with the lid.

A.5 Figures

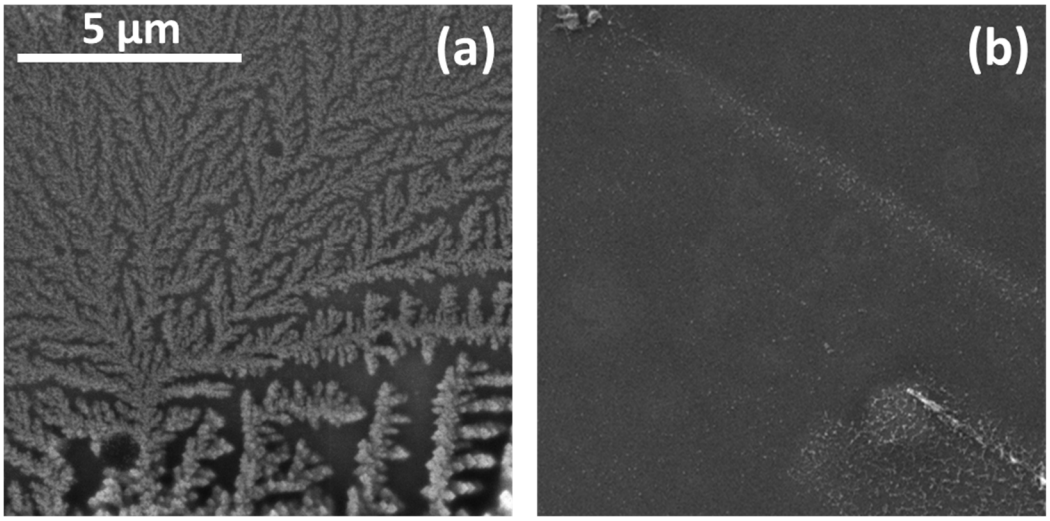

Figure A.1 Outcome of dendrite cleaning on GaN sample surface. (a) Dendrite observed on the surface of the GaN sample. (b) Surface of the same GaN sample, same area after dendrite removal following the procedure in Section A.3.

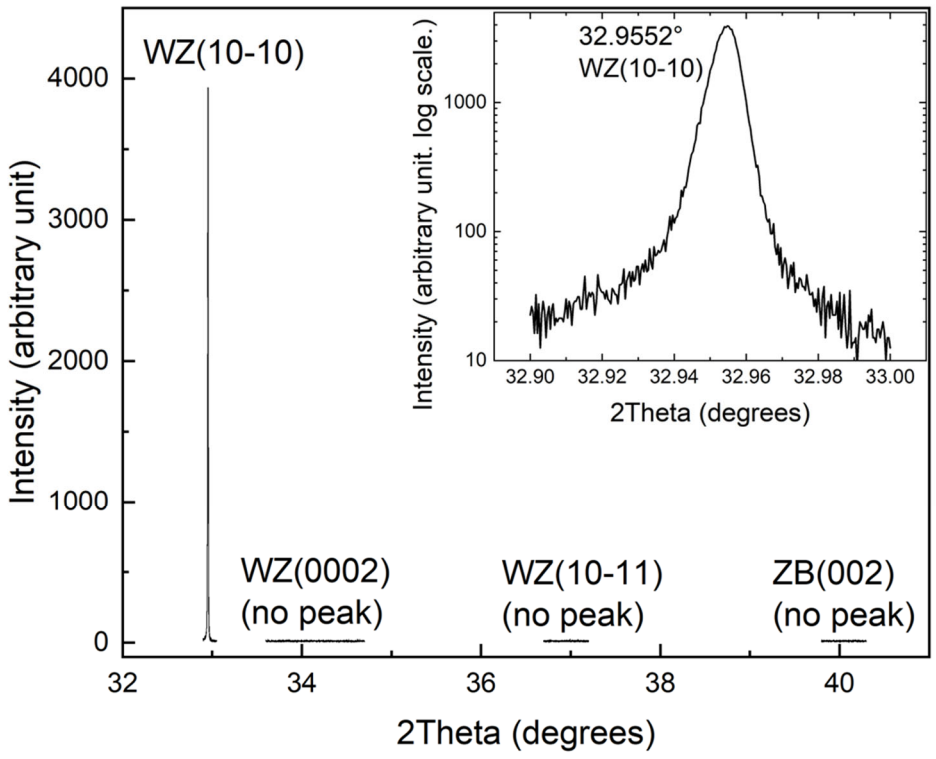

Figure A.2 XRD of GaN sample growth attempt with Addon plasma source. XRD scans ranges from 32.9°–33.0°, 33.6°–34.7°, 36.7°–37.2°, and 39.8°–40.3° were used to verify the presence of WZ(10$\bar{1}$0), WZ(0002), WZ(10$\bar{1}$1), and ZB(200), respectively. One peak from WZ(10-10) at 32.96° with FWHM = 0.00854° (30.74 arcsec) was observed. The close-up in logarithm scale is shown in the inset. For the XRD spectra, step size of 2 arcsec (0.0005°, 1 sec integration time) were used.

Appendix B Density Functional Theory Calculation

B.1 Introduction

In this appendix, we describe density functional theory (DFT) calculations of diffusion barriers and adsorption energetics on silicon surfaces. We first discuss calculations of the diffusion barriers of Ga and N adatoms on SiO_2(001), Si(001), and Si(111) surfaces. Using the Nudged-Elastic Band method, reaction paths are constructed for various Ga and N adatom surface diffusion processes. We then discuss calculations of the adsorption energetics of Ga adatoms on nitride/oxidized Si(001) with varying surface coverages.

B.2 Ga and N surface diffusions

To compute the Ga and N surface diffusion barriers, a Materials Studio CASTEP module was used,[1,2] with exchange and correlation interactions described using the Generalized Gradient Approximation (GGA) and the Perdew-Burke-Ernzerhof (PBE)[3] functional, and electron-ion core interactions described using ultra-soft pseudopotentials.[4] Geometric optimization was performed using the Broyden-Fletchter-Goldfarb-Shanno (BFGS) optimization algorithm,[5] with convergence criteria including (a) self-consistent field (SCF) of 5.0×10^{-7} eV/atom, (b) energy of 5×10^{-6} eV/atom, (c) displacement of 5×10^{-4} Å, (d) force of 0.01 eV/Å, and (e) stress of 0.02 GPa. Transition states were determined using the complete linear synchronous transitions (LST)/ quadratic synchronous transitions (QST) method[6] with convergence criteria set to 0.05 eV/Å, and confirmed by the Nudged-Elastic Band (NEB) method,[7] with convergence criteria including (a) energy of 1.0×10^{-5} eV/atom, (b) maximum force of 0.05 eV/ Å, and (c) maximum displacement of 0.004 Å.

The energies of crystalline Si and SiO_2 cells were converged with 6 × 6 × 6 k points in a Monhorst-pack grid,[8] while the slab models and related adsorption structures were converged with 2 × 2 × 1 k points. The electronic wave functions were expanded in a plane wave basis with a 300 eV cutoff energy. With relaxed surface layer of atoms and fixed buried layers,[9] the vacuum region between slabs was set to 12 Å to avoid interactions among periodic image charges.[10] As shown in **Table F.4**, the calculated lattice parameters are consistent with prior experimental and computational studies,[11,12] confirming the reliability of our calculations. In addition, the computed coordination numbers for Si atoms on Si (001), Si (111), and SiO_2 (001) surfaces are 2, 3, and 2, respectively, consistent with values computed in prior first-principles calculations.[13,14,15]

B.3 Ga adsorption on nitrided/oxidized silicon surfaces

We also used DFT to compute the adsorption energy of Ga on nitrided and oxidized Si surfaces as follows:

$$E_{ads}^{Ga} = \left[E_{Si} + E_{Si-N(O)-Ga}\right] - \left[E_{Si-N(O)} + E_{Si-Ga}\right] \qquad \text{(Equation B.1)}$$

where E_{Si-Ga} and $E_{Si-N(O)}$ denote the reference energies for isolated Ga atoms and gas atoms (N or O) on the Si surface; E_{Si} and $E_{Si-N(O)-Ga}$ denote the energies for a clean silicon surface and N(O) bonded to Ga on the silicon surface, respectively. Since first principles methods replicate the thermodynamically-stable (2 x 1) Si (001) surface reconstruction[16] but not the (7 x 7) Si (111) surface reconstruction,[17] our DFT calculations are limited to those for E_{ads}^{Ga} on the Si (001) surface.

All calculations were performed with the Vienna ab initio Simulation Package (VASP)[21], using the Perdew-Burke-Ernzerhof[18] (PBE) pseudopotential implemented with the projected augmented-wave[19,20] (PAW) method. The Si (001) surface was modeled using 48 Si atoms in 6 layers, with 16 Å vacuum thickness in the z-direction perpendicular to (001). In the bottom 3 layers,

Si ions were kept fixed, while those in the bottom Si surface were H-saturated. In the top 3 layers, the Si ions were mobile and fully relaxed. Following DFT relaxations, the (2 × 1) reconstruction of the Si (001) surface unit cell was observed, as shown in Figure B.**7**.

Additional calculations were performed to obtain the Ga adsorption energy as a function of N/O surface coverage on Si(001). For the adsorption of a single N or O atom, E_{ads}^{Ga} is lowest for the bridge site, indicating it is the most favorable thermodynamically. These adsorption geometries of 1 N atom and 1 N + 1 Ga atoms are presented in Figure B.7. Higher surface coverage (2N or 2O atoms) was generated by adsorption of gas atoms at 2 nearby bridge sites (the less stable hollow and lattice sites are not considered). The corresponding adsorption configurations for 2 N atoms and 2 N + 1 Ga atoms are shown in Figure B.8.

C.1 Figures

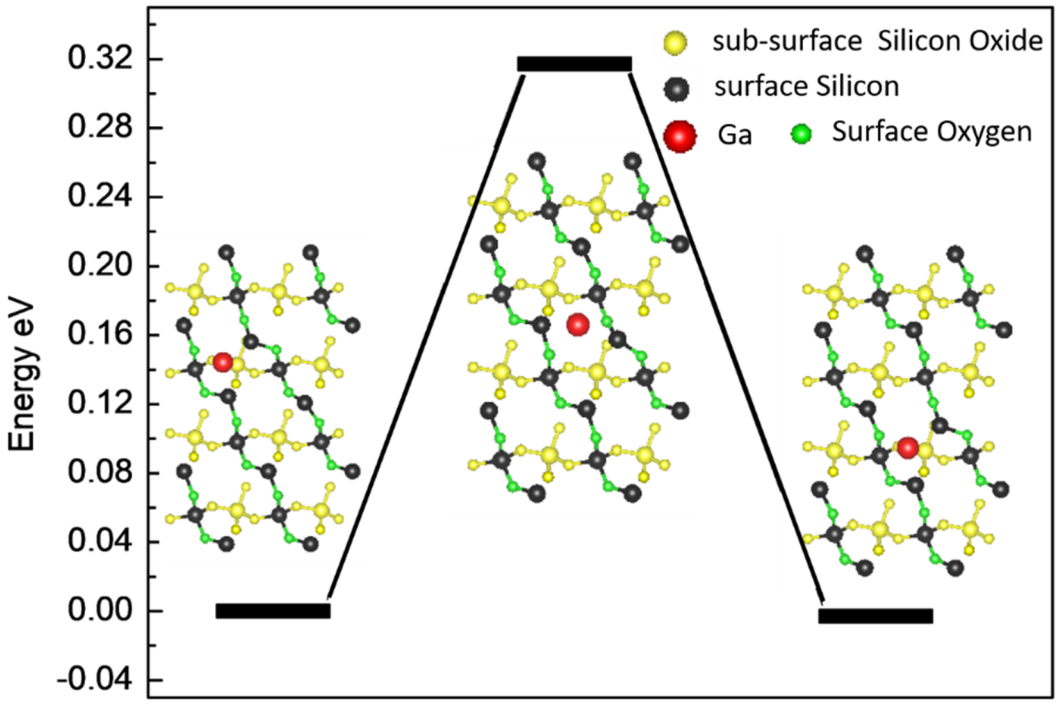

Figure B.1 Reaction path for Ga adatom (red) diffusion on SiO_2(001) surface viewed from the top, overlaid on a plot of the energies of the initial, intermediate, and final states. The initial energy state is defined as zero, and the surface oxygen, surface silicon, and sub-surface SiO_2 are shown in green, black, and yellow, respectively. Reprinted figure with permission from Ref 36 (Copyright 2020, AIP Publishing).

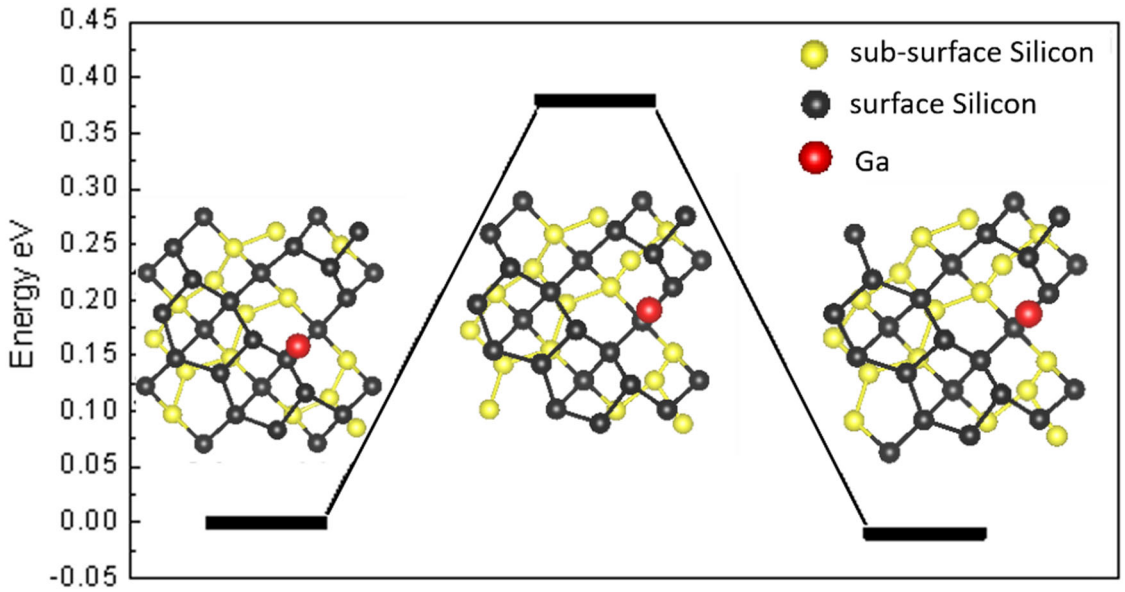

Figure B.2 Reaction path for Ga adatom (red) diffusion on Si (001) surface viewed from the top, overlaid on a plot of the energies of the initial, intermediate, and final states. The initial energy state is defined as zero, and the sub-surface silicon, surface silicon, and gallium are shown in yellow, black, and red, respectively. Reprinted figure with permission from Ref 36 (Copyright 2020, AIP Publishing).

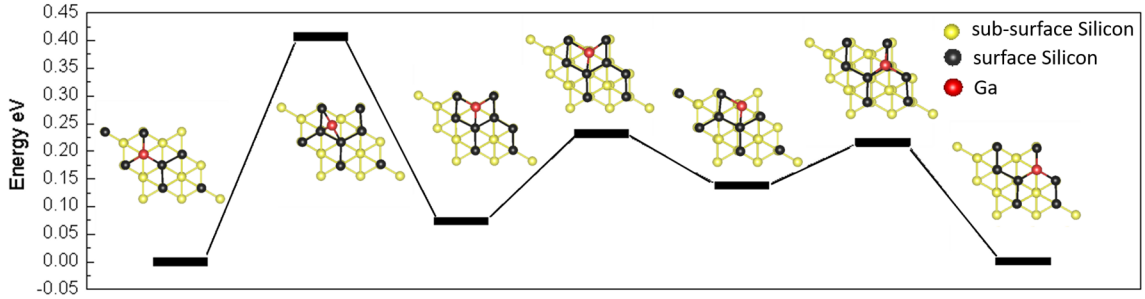

Figure B.3 Reaction path for Ga adatom (red) diffusion on Si (111) surface viewed from the top, overlaid on a plot of the energies of the initial, intermediate, and final states. The initial energy state is defined as zero, and the sub-surface silicon, surface silicon, and gallium are shown in yellow, black, and red, respectively. Reprinted figure with permission from Ref 36 (Copyright 2020, AIP Publishing).

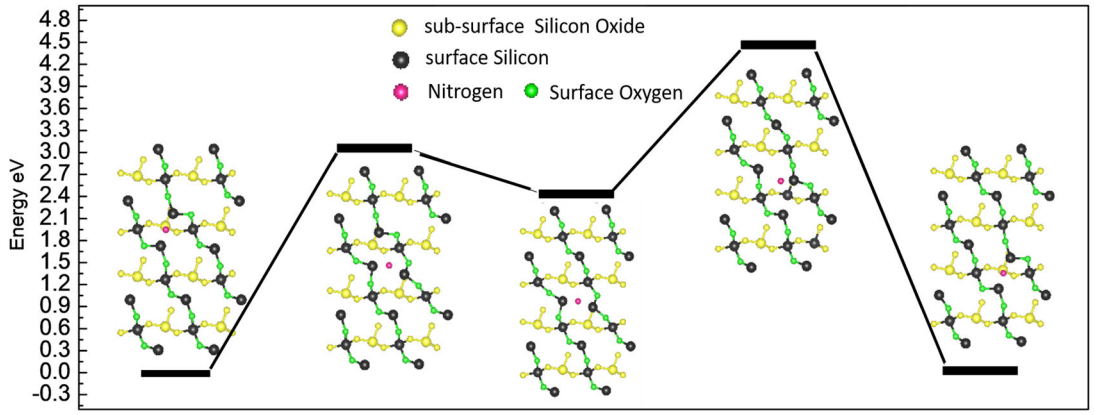

Figure B.4 Reaction path for N adatom (pink) diffusion on SiO_2(001) surface viewed from the top, overlaid on a plot of the energies of the initial, several intermediate, and final states. The initial energy state is defined as zero, and the surface oxygen, surface silicon, and sub-surface SiO_2 are shown in green, black, and yellow, respectively. Reprinted figure with permission from Ref 36 (Copyright 2020, AIP Publishing).

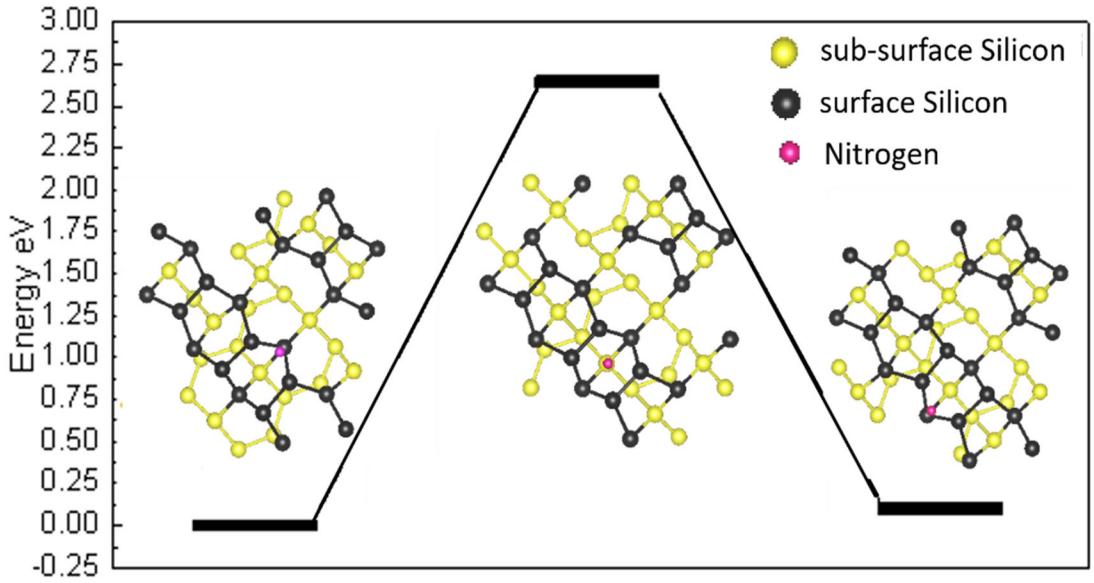

Figure B.5 Reaction path for N adatom (pink) diffusion on Si (001) surface viewed from the top, overlaid on a plot of the energies of the initial, intermediate, and final states. The initial energy state is defined as zero, and the surface oxygen, surface silicon, and sub-surface Si are shown in green, black, and yellow, respectively. Reprinted figure with permission from Ref 36 (Copyright 2020, AIP Publishing).

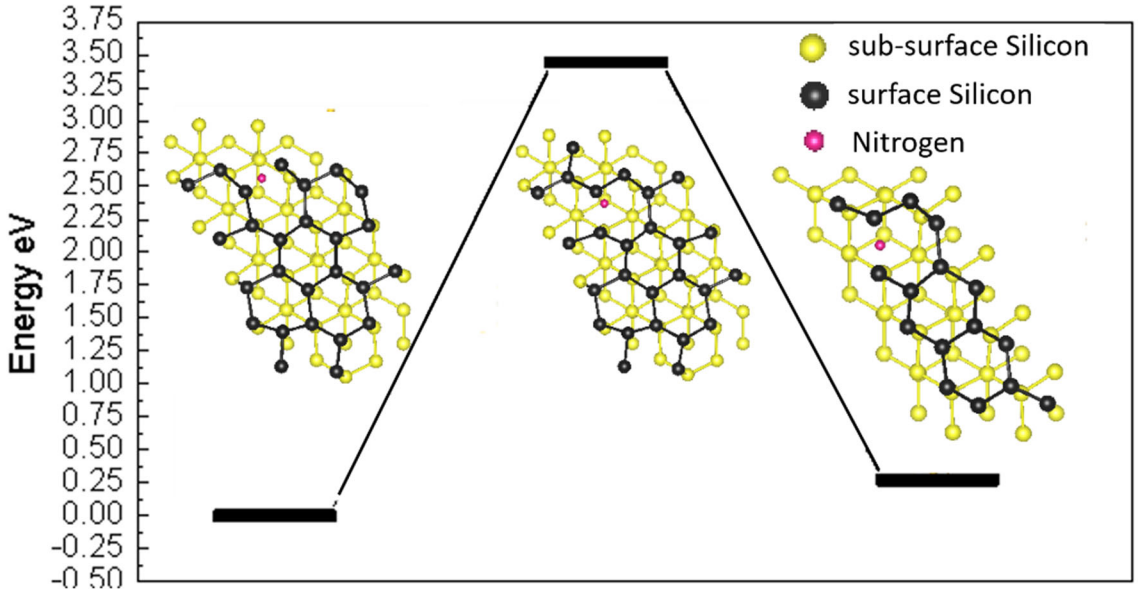

Figure B.6 Reaction path for N adatom (pink) diffusion on Si (111) surface viewed from the top, overlaid on a plot of the energies of the initial, intermediate, and final states. The initial energy state is defined as zero, and the surface oxygen, surface silicon, and sub-surface Si are shown in green, black, and yellow, respectively. Reprinted figure with permission from Ref 36 (Copyright 2020, AIP Publishing).

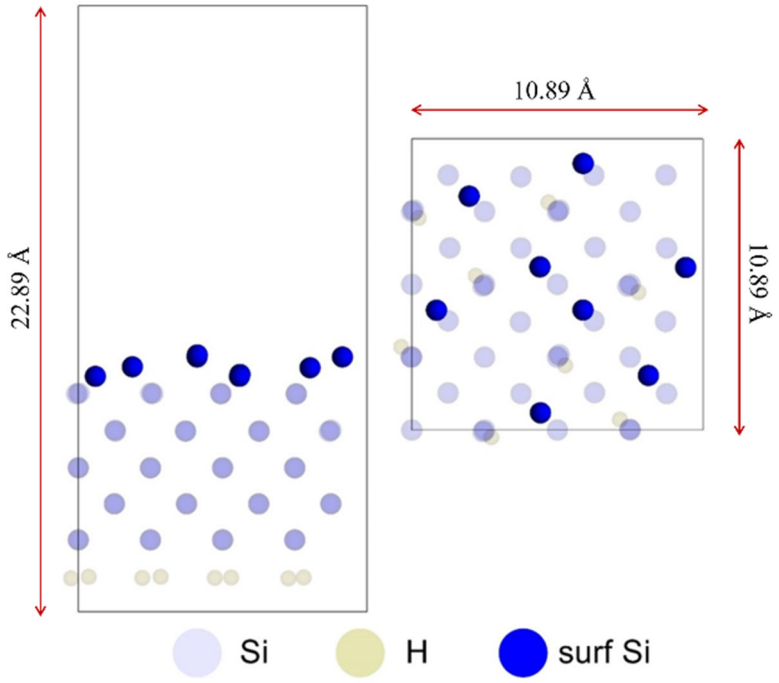

Figure B.7 Side and top views of the (2×1) reconstructed Si (001) supercell with 8 surface Si atoms (dark blue dots labeled as "surf Si"). The bottom surface is saturated by H atoms. By fixing the bottom 3 layers and relaxing atoms in the top 3 layers, the free (001) Si surface undergoes a reconstruction where two near surface Si atoms always come close to each other. The energy of this configuration is E_{Si}. Reprinted figure with permission from Ref 36 (Copyright 2020, AIP Publishing).

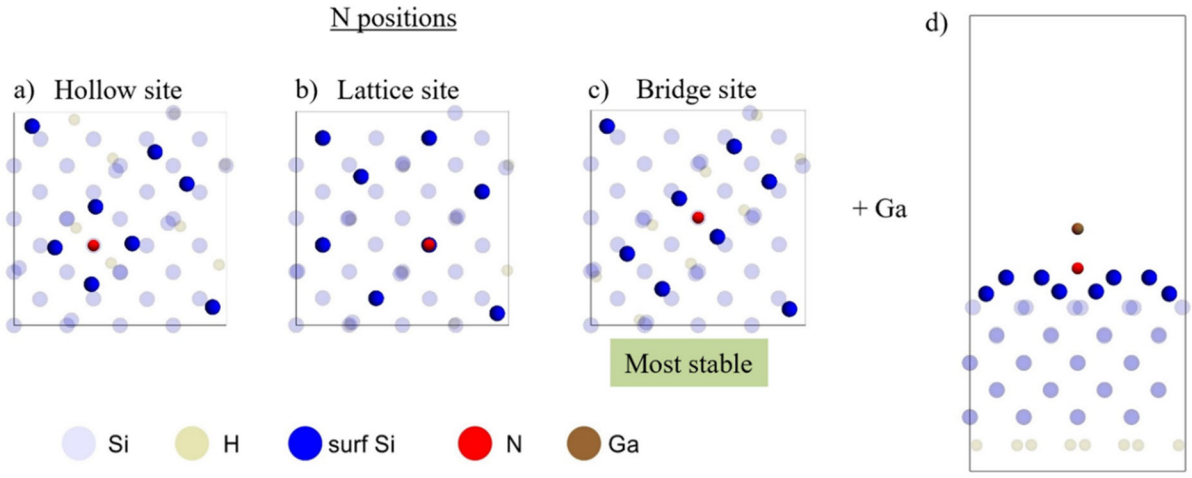

Figure B.8 (a) - (c): Top views of adsorption configurations for 1N atom on (2×1) Si (001). The different configurations identified for N are (a) the hollow site with N bonded to 4 surface Si atoms, (b) the lattice site with the N vertically above a surface Si atom, and (c) the bridge site with N bonded to 2 surface Si atoms, respectively. The bridge site is found to be most stable thermodynamically and its energy corresponds to E_{Si-N} in (Equation B.1 A Ga atom is added to the surface configuration of (c), resulting a Ga-N bonded configuration as shown in (d) (Side View). The total energy of (d) is accounted for $E_{Si-N-Ga}$ in (Equation B.1 Similar structures were obtained for the adsorption of 1 Ga atom on the same Si (001) supercell with 1 O atom. Reprinted figure with permission from Ref 36 (Copyright 2020, AIP Publishing).

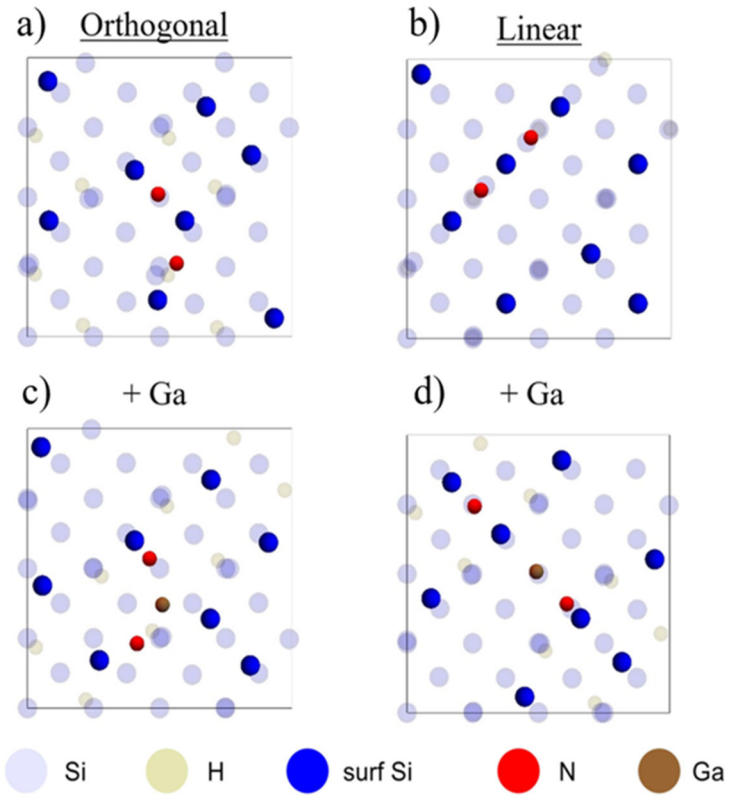

Figure B.9 Adsorption energetics of Ga on Si (001) with increasing N surface coverage. 2 N atoms adsorbed in (a) orthogonal or (b) linear bridge sites on the Si (001) surface (hollow and lattice sites are not considered since the bridge site was found to be more stable). In both cases, the central Si atom is bonded to 2 N atoms. The orthogonal arrangement of N atoms in (a) is more stable by 2.0 eV compared with (b). (c) and (d) show adsorption of 1 Ga atom and subsequent bond formation with N. (d) is found to be more stable than (c) by 2.0 eV. Similar structures were obtained for the adsorption of 1 Ga atom on the same Si (001) supercell with 2 O atoms. Reprinted figure with permission from Ref 36 (Copyright 2020, AIP Publishing).

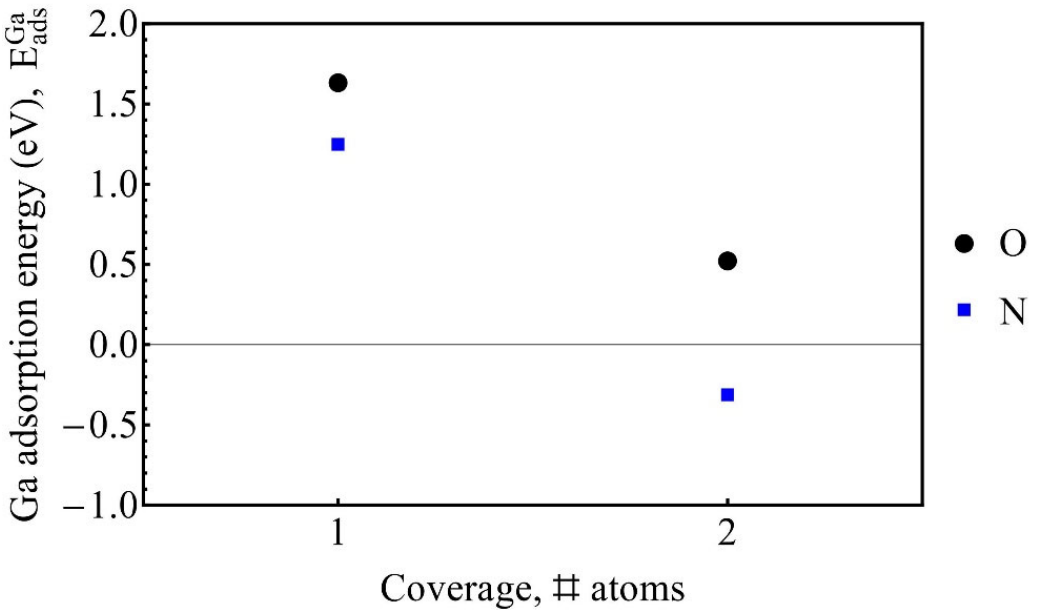

Figure B.10 Plot of adsorption energies for a single Ga atom, $\mathbf{E_{ads}^{Ga}}$, as a function of the number of adsorbed surface O or N on the (2 × 1) reconstructed Si (001) surface supercell shown in Figure B.7. Positive (negative) energies are repulsive (attractive). Black dots and blue squares correspond to O and N atoms, respectively. Reprinted figure with permission from Ref 36 (Copyright 2020, AIP Publishing).

C.2 References

[1] M.D. Segall, P.J. Lindan, M.A. Probert, C.J. Pickard, P.J. Hasnip, S.J. Clark, and M.C. Payne, "First-principles simulation: ideas, illustrations and the CASTEP code", J. Phys. Condens. Mat. 14, 2717 (2002).

[2] S.J. Clark, M.D. Segall, C.J. Pickard, P.J. Hasnip, M.A. Probert, K. Refson, and M.C. Payne, "First principles methods using CASTEP", Cryst. Mater. 220, 567 (2005).

[3] J.P. Perdew, K. Burke, and M. Ernzerhof, "Generalized Gradient Approximation Made Simple", Phys. Rev. Lett. 77, 3865 (1996).

[4] D. Vanderbilt, "Soft self-consistent pseudopotentials in a generalized eigenvalue formalism", Phys. Rev. B 41, 7892 (1990).

[5] W.H. Press, S.A. Teukolsky, W.T. Vetterling, and B.P. Flannery, *Numerical Recipes in C.* Cambridge University Press (1996).

[6] T.A. Halgren and W.N. Lipscomb, "The synchronous-transit method for determining reaction pathways and locating molecular transition states", Chem. Phys. Lett. 49, 225 (1977).

[7] G. Henkelman and H. Jónsson, "Improved tangent estimate in the nudged elastic band method for finding minimum energy paths and saddle points", J. Chem. Phys. 113, 9978 (2000).

[8] H.J. Monkhorst and J.D. Pack, "Special points for Brillouin-zone integrations", Phys. Rev. B 13, 5188 (1976).

[9] S. Sun, D. Zhang, C. Li, Y. Wang, and Q. Yang, "Superior sponge-like carbon self-doping graphitic carbon nitride nanosheets derived from supramolecular pre-assembly of a melamine–cyanuric acid complex for photocatalytic H2 evolution", Chem. Eng. J. 258, 128 (2014).

[10] W. Xiang, J. Liu, M. Chang, and C. Zheng, "Density functional theory study on Hg removal mechanisms of Cu-impregnated activated carbon prepared by simplified method", Chem. Eng. J. 200, 91 (2012).

[11] S. Baroni and R. Resta, "Ab initio calculation of the macroscopic dielectric constant in silicon", Phys. Rev. B 33, 7017 (1986).

[12] S. Tsuneyuki, M. Tsukada, H. Aoki, and Y. Matsui, "First-Principles Interatomic Potential of Silica Applied to Molecular Dynamics", Phys. Rev. Lett. 61, 869 (1988).

[13] K. Johnston, A. Gulans, T. Verho, and M.J. Puska, "Adsorption structures of phenol on the Si(001)-(2×1) surface calculated using density functional theory", Phys Rev. B 81, 235428 (2010).

[14] H.H. Arefi and G. Fagas, "Chemical Trends in the Work Function of Modified Si(111) Surfaces: A DFT Study", J. Phys. Chem. C 118, 14354 (2014).

[15] O.I. Malyi, P. Thiyam, M. Boström, and C. Persson, "A first principles study of CO2 adsorption on α-SiO2(001) surfaces", Phys. Chem. Chem. Phys. 17, 20125 (2015).

[16] D. J. Chadi, "Atomic and Electronic Structures of Reconstructed Si(100) Surfaces", Phys. Rev. Lett. 43, 43 (1979).

[17] K. D. Brommer, M. Needels, B. Larson, and J. D. Joannopoulos, "Ab initio theory of the Si(111)-(7×7) surface reconstruction: A challenge for massively parallel computation", Phys. Rev. Lett. 68, 1355 (1992).

[18] J. Perdew, K. Burke, and M. Ernzerhof, "Generalized Gradient Approximation Made Simple", Phys. Rev. Lett. 77, 3865 (1996).

[19] P. E. Blöchl, "Projector augmented-wave method", Phys. Rev. B 50, 17953 (1994).

[20] G. Kresse and D. Joubert, "From ultrasoft pseudopotentials to the projector augmented-wave method", Phys. Rev. B 59,1758 (1999).

Appendix C RHEED and Nanoparticle Analysis

C.1 Introduction

This appendix describes the data analysis details used in this thesis. Section C.2 describes the RHEED video and pattern analysis used in Chapter 5. Section C.3 describes the lattice parameter analysis using FFT used in Chapter 4. Section C.3.2, describes the size distribution analysis used in Chapter 4.

C.2 RHEED Video and Pattern Analysis

Reflection High Energy Electron Diffraction (RHEED) allows direct measurements of the surface structure in real time during epitaxy. RHEED patterns are most often used to identify surface morphology and the oscillations of the specular beam are used to calculate growth rate. In principle a detailed analysis of the diffraction patterns also permits an exact determination of the complete structure of the surface structure. In this appendix, the first script can be used to extract every frame of a RHEED video. The second script provides a way to analyze RHEED video and image quantitively and accurately.

C.2.1 RHEED analysis approach of epitaxial thin films and nanostructures

The script that I developed using Matlab finds regions around each spot and treats each region differently based on the overall brightness of that region. Figure C.1 is an example of what the spot extraction result looks like for a RHEED collected during GaN NW growth.

From the spot extraction, the script first defines locations by its coordinate in the image. Then, the distance of each spot from the center beam spot can be calculated. In the case where the center spot is not visible in the RHEED image, it can be calculated using diffraction fundamentals, where symmetrical spots lie on the intersection of reciprocal lattice planes and Ewald sphere to

calculate the expected location of where the center beam spot. The calculated distances are the radius of the circles on the cross section of Ewald sphere, as illustrated in Figure C.2. Following the calculation of the radius, we compare the ratio square values in the RHEED with theoretical values as listed in Table E.1 and Table E.2 to analyze the diffraction patterns.

The spot identification script does the following:

1) Finds and extracts exactly where the spots are including the faint ones (Figure C.2(b)).
2) Defines spot coordinate (Figure C.2 (c)).
3) Defines center beam spots if not present.
4) Measures the distance of each RHEED spots to the center spot (Figure C.2(d)).
5) Analyzes the possible indices for the RHEED spots.

C.2.2 Detailed analysis of the diffracted pattern using spot identification script

The first script is used for a qualitative analysis of RHEED videos. First, all the frames are extracted from a single RHEED video and lined up together, for individual visual inspection. For example, in a 2-min video with a video frame rate of 10 frames/sec, there should be a total of 1154 frames. By displaying them next to each other, angles between frames can be calculated, and any extra spots or features can be found and analyzed using the second script.

C.2.3 MATLAB code for frame extraction

```
% import the video file
obj = VideoReader('[file name].avi');
vid = read(obj);

 % read the total number of frames
frames = obj.NumberOfFrames;

% file format of the frames to be saved in
ST ='[file name].jpg';

% reading and writing the frames
for x = 1 : frames

   % converting integer to string
   Sx = num2str(x);

   % concatenating 2 strings
   Strc = strcat(Sx, ST);
   Vid = vid(:, :, :, x);
   cd frames

   % exporting the frames
   imwrite(Vid, Strc);
   cd ..
end
```

C.2.4 MATLAB code for spot identification

```
X = imread('[file name].png');
R = size(X, 1);
C = size(X, 2);
g = zeros(R,C);

% set section boundary

imshow(X);
hold on

xline(260,'Color','green','LineWidth',1); %c
xline(280,'Color','green','LineWidth',1); %c
yline(110,'Color','magenta','LineWidth',1); %r
yline(125,'Color','magenta','LineWidth',1); %r

% Use the following code to box region of interest and treat each section separately
```

```
for r = 1:size(X, 1)    % for number of rows of the image
   for c = 1:size(X, 2)    % for number of columns of the image
      if c>=260 && c<=280 && r>=110 && r<=125 && X(r, c) > 57
         g(r,c) = 255;
      end
      if c>=340 && c<=350 && r>=110 && r<=125 && X(r, c) > 50
         g(r,c) = 255;
      end
      if c>=180 && c<=190 && r>=120 && r<=130 && X(r, c) > 120
         g(r,c) = 255;
      end

      %{ other regions of interest goes here %}

   end
end

% Clean up individual pixels. Use when necessary: if the spots identified from step above is not
a well-defined circle
for r = 1:size(X, 1)    % for number of rows of the image
   for c = 1:size(X, 2)    % for number of columns of the image
      if r>1 && r<R && c>1 && c<C && g(r,c-1)==0 && g(r,c+1)==0
         g(r,c) = 0;
      end
   end
end

figure;
imshow(g);
hold on

% For each column of spots, the following section of code calculates the center of each spot
r = 1;
while r <= R    % for number of rows of the image
   for c = 1:50    % for number of columns of the image
      if g(r,c)==255 % encounter the first white pixel, mark as the start of the new spot
         tracing = c;
         while tracing <= 210 && g(r,tracing)==255 % count horizontal white pixels
            tracing = tracing + 1; % increase count
         end
         starting_point = [r c];
         diameter_count = 1; % start counting diameter
         down = [r+1 starting_point(2)]; % move to diagonal pixel
         while g(down(1),down(2))== 255 % keep counting until not white
```

```
            diameter_count = diameter_count+1; % increase diagonal count
            down = [down(1)+1 down(2)]; % move to the next diagonal pixel
        end
        radius = ceil(diameter_count/2);
        center_r = starting_point(1) + radius;
        center_c = starting_point(2);
        hold on
        if radius > 1
            plot(center_c, center_r, '.', 'MarkerSize', 10,'Color','red');
            viscircles([center_c, center_r], radius,'Color','red','LineWidth',2);
            disp('here1')
            disp([center_c, center_r]);
        end
        r = down(1);
    end
  end
  r = r+1;
end

%{ other columns of spots go here %}

figure;
imshow(g);
hold on
```

C.3 Lattice Spacing Analysis via FFT

This section demonstrates how to use fast Fourier transform (FFT) to estimate lattice spacings from TEM images. This process is used to estimate lattice spacings in InN droplet epitaxy study mentioned in Chapter 4. Note that GMS3 is available only for Windows operating system at the time this thesis is being written, but the approach is transferable to other TEM analysis software.

C.3.1 TEM lattice spacing analysis using Gatan GMS3 software

Step 1. Box region of interest.

Step 2. Calibrate GMS software measurement with scale bar.

Step 3. Perform FFT. If spots do not stand out from the background brightness, adjust display control so that the spot locations are unambiguous.

Step 4. Apply mask.

Step 5. Measure distance between peaks.

Step 6. Calculate the inverse of the measured distance.

C.3.2 Size Analysis of Nanoparticles

C.3.2.1 Introduction

Here we describe the procedure for identification and size quantification of the MBE-grown nanoparticles based on ETEM images. ImageJ and MountainsSPIP® (previously SPIP™)[1] were used to perform the analyses. The image processing and size analysis used in this thesis involves two steps: background subtraction and size analysis. For size analysis, threshold segregation was used for all particle size distribution analysis. The first section describes the image processing steps, and the steps for threshold detection are described in the second section.

C.3.2.2 Background Subtraction using ImageJ

Step 1. If the background is noisy as in the example shown in

Step 2. Figure C.4 (a), reduction of background noises is needed. To do so, use the [Process] → [Smooth] in the menu of ImageJ. The "smooth" function blurs the active image or selection. This filter replaces each pixel with the average of its 3 × 3 neighborhood, thus reducing noises from the background.

Step 3. If the illumination in the background is uneven, as in the example shown in

Step 4. Figure C.4 (center is brighter than the edges), the brightness unevenness needs to be corrected. To do so, use the [Process] → [Subtract background] menu of ImageJ. This "subtract background" function corrects for uneven illuminated background by using a "rolling ball" algorithm. A local background value is determined for every pixel by averaging over a very large ball around the pixel. This value is hereafter subtracted from

the original image, hopefully removing large spatial variations of the background intensities. The radius should be set to at least the size of the largest object that is not part of the background. The rolling-ball algorithm was inspired by Stanley Sternberg's article, "Biomedical Image Processing.[2]

C.3.2.3 Size Analysis Using Threshold Segmentation MoutainsSPIP®

Threshold detection method in MoutainsSPIP® detects particles using user-defined thresholds.

Step 1. In MoutainsSPIP® software, open the image processed by ImageJ (the output from step 3).

Step 2. Use [Operators] → [Scale the image] to set the scale of image based on scale bar or image information obtained from TEM image info files or headers.

Step 3. Use [Studies] → [Particle analysis] → [Threshold detection] in MoutainsSPIP® to detect particles. In this thesis, in the "Particles to detect" pull down menu, "Below a threshold value" was selected.

Step 4. Remove small particles (noises) from the background by using [Studies] → [Particle Analysis] → [Refine detection] feature in the menu. Select [Remove small particles] with area < _____ nm^2. Size threshold needs to be determined based on the smallest particles in the image. In the size analysis used in this thesis, area < 2 nm^2 is used. Refine area detected by using [Studies] → [Particle Analysis] → [Morphological correction]. In the size analysis used in this thesis, under "Operation", "Opening" was selected. Condition for strength and iteration needs to be determined based on the image. In this thesis, highest strength (4) and highest iteration (5) were used. Depending on the

result of the particle analysis, select “Merge continuous particles”. In the size analysis, “Merge continuous particles” was selected.

C.3.3 Stain calculations within nanoparticles

The strain within nanoparticles discussed in section 4.4.2 is calculated using the following equation:[3]

$$\varepsilon \equiv \frac{d_{\text{relaxed}} - d_{\text{strained}}}{d_{\text{relaxed}}} \qquad \text{(Equation C.1)}$$

where d_{relaxed} is relaxed lattice spacing values found in Table F.3, and d_{strained} is the calculated lattice spacing d_2 values, following (Equation 4.1, using observed moiré fringe spacings of 3.4 nm as D and observed lattice spacings within nanostructures as d_1. Thus, a negative value of ε represents tension, while a positive value of ε represents compressions.

	d_1 [nm]	d_2 [nm]		
(a) Between InN-ZB(111) and In_2O_3(400)	**InN ZB(111) (calculated)**	**In_2O_3(400) (measured)**	**$d_{relaxed}$ InN ZB(111)**	**strain (in InN)**
	0.233	0.25	0.253	8%
	0.27	0.25	0.253	-7%
	InN ZB(111) (measured)	**In_2O_3(400) (calculated)**	**$d_{relaxed}$ In_2O_3(400)**	**strain (in In_2O_3)**
	0.25	0.23	0.262	12%
	0.25	0.27	0.262	-3%
(b) Between InN-ZB(001) and In_2O_3(220)	**InN ZB(001) (calculated)**	**In_2O_3(220) (measured)**	**$d_{relaxed}$ InN ZB(220)**	**strain (in InN ZB)**
	0.478	0.42	0.453	-6%
	0.374	0.42	0.453	17%
	InN ZB(001) (measured)	**In_2O_3(220) (calculated)**	**$d_{relaxed}$ In2O3(220)**	**strain (in In_2O_3)**
	0.42	0.478	0.357	-34%
	0.42	0.374	0.357	-5%
(c) Between InN-WZ(10-10) and In_2O_3(311)/(222)	**InN-WZ(10-10) (calculated)**	**In_2O_3(311) (measured)**	**$d_{relaxed}$ InN-WZ(10-10)**	**strain (in InN WZ)**
	0.276	0.3	0.306	10%
	0.329	0.3	0.306	-8%
	InN-WZ(10-10) (measured)	**In_2O_3(311) (calculated)**	**$d_{relaxed}$ In_2O_3(311)**	**strain (in In_2O_3)**
	0.3	0.276	0.304	9%
	0.3	0.329	0.304	-8%
	InN-WZ(10-10) (calculated)	**In_2O_3(222) (measured)**	**$d_{relaxed}$ InN-WZ(10-10)**	**strain (in InN WZ)**
	0.276	0.3	0.306	10%
	0.329	0.3	0.306	-8%
	InN-WZ(10-10) (measured)	**In_2O_3(222) (calculated)**	**$d_{relaxed}$ In_2O_3(222)**	**strain (in In_2O_3)**
	0.3	0.276	0.292	5%
	0.3	0.329	0.292	-13%

Table C.1 Full analysis of strains expected from different combinations of possible lattice planes. The green selection is illustrated in Figure 4.9. The "calculated" lattice spacing values are referring to the values calculated using (Equation 4.1 with D = 3.4 nm. The $d_{relaxed}$ values are taken from Table F.3.

C.3.5 Figures

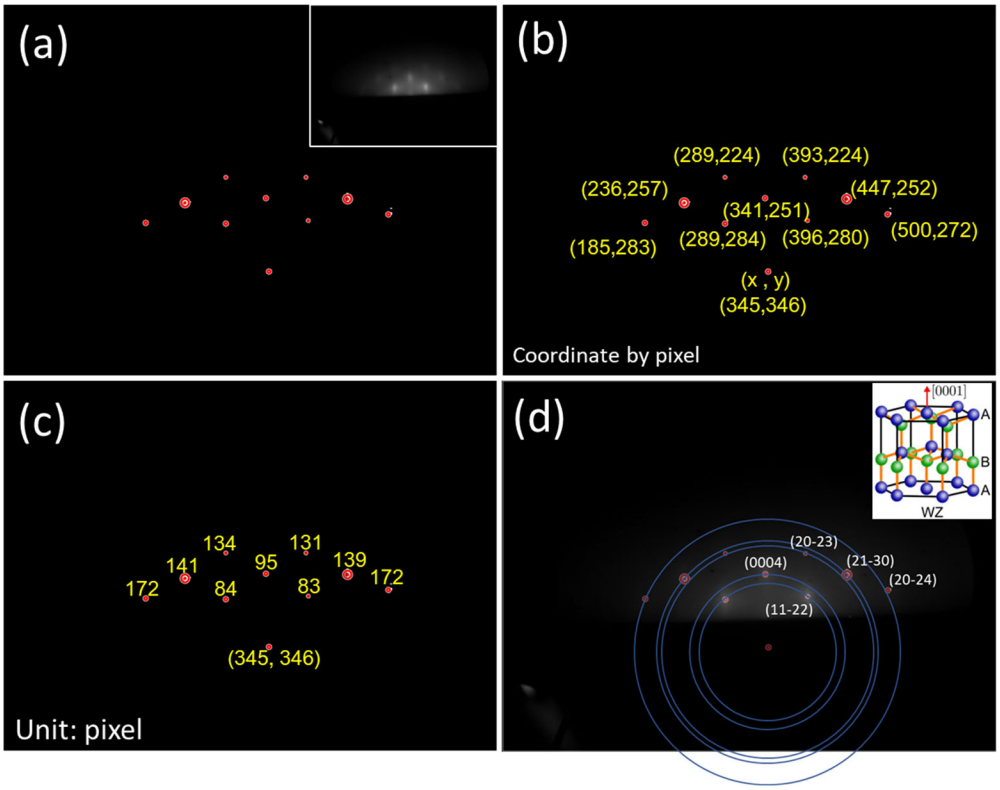

Figure C.1 Example of RHEED spot extraction approach. (a) Results of spot identification; inset is the RHEED from GaN NW growth used for this example. (b) Spot identified by coordinates by pixel. (c) Distance from center calculated for each spot. (d) Diffraction patterns analyzed by comparing squares of the ratios.

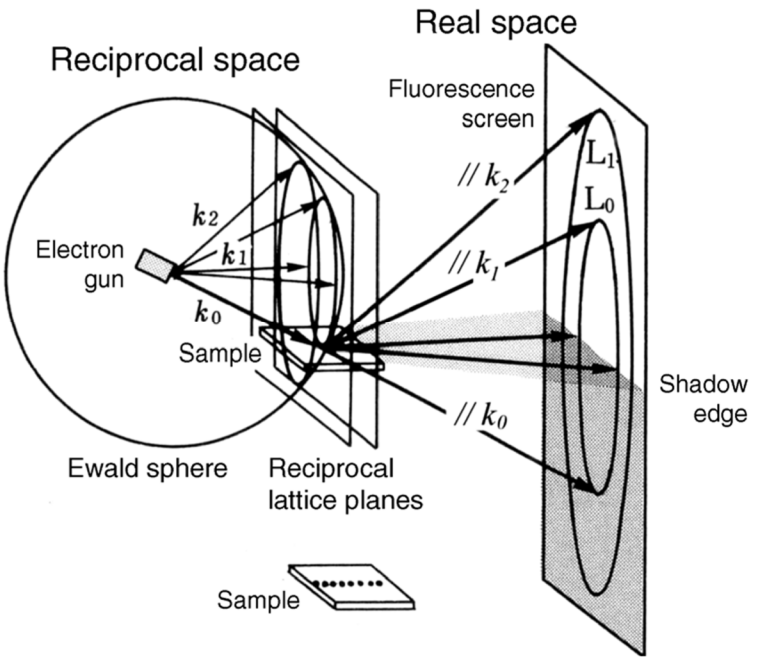

Figure C.2 Illustrations of RHEED in real and reciprocal space. The intersection of reciprocal lattice planes and Ewald sphere is shown as the concentric circles labeled with "L_0" and "L_1".[4]

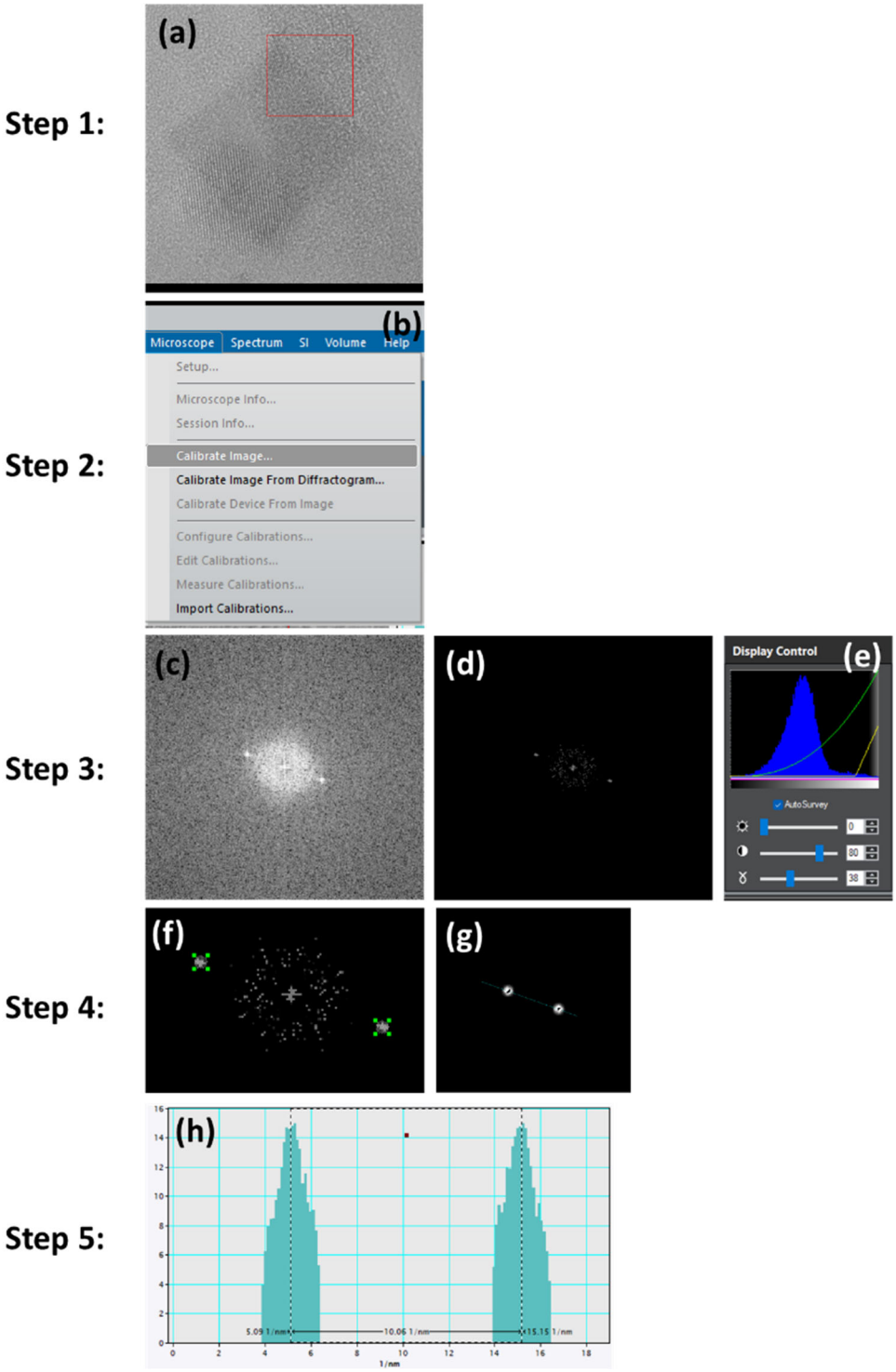

Figure C.3 Steps for analyzing TEM lattice spacing using FFT in GMS3 software. (a) Select region of interest. (b) Calibrate image. (c)-(e) Perform FFT and adjust display control if the spots do not stand out from the background. (f)-(g) Apply masks. (h) Measure distance between peaks; note that the measured distance has unit nm^{-1}, so taking an inverse is necessary to get the lattice spacing value in nm.

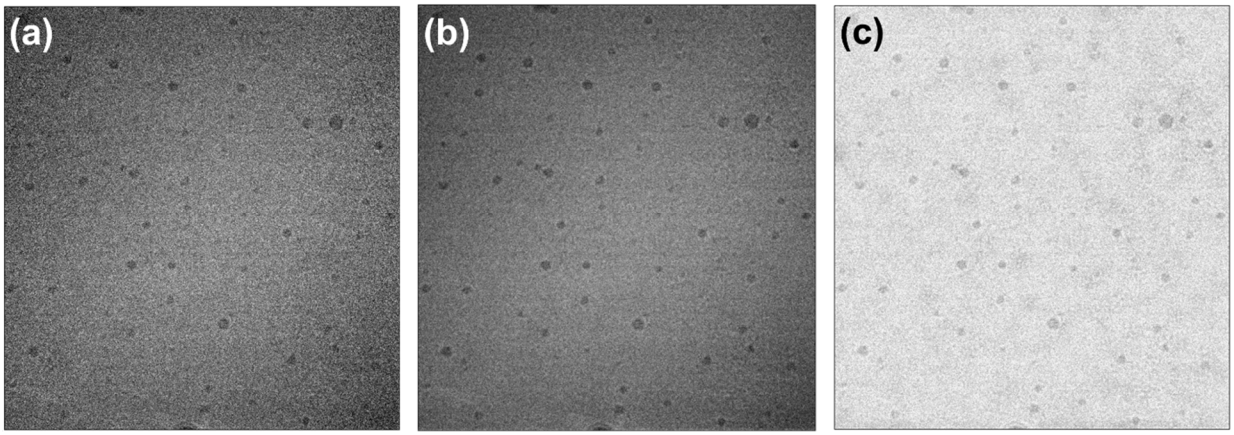

Figure C.4 Example of pre-processing of TEM image using ImageJ software for particle analysis. (a) Original image of a frame from ETEM video. (b) Image after smoothing. (c) Image after background subtraction.

C.3.6 References

[1] Digital Surf (November 12, 2018) The Story Behind Mountainsspip® https://www.digitalsurf.com/news/the-story-behind-mountainsspip/

[2] S. R. Sternberg, "Biomedical Image Processing", Computer 16, 22 (1983).

[3] S.C. Jain, A.H. Harker and R.A. Cowley "Misfit strain and misfit dislocations in lattice mismatched epitaxial layers and other systems", Philos. Mag. A, **75**, 1461 (1997).

[4] S. Hasegawa, in Characterization of Materials, edited by E. N. Kaufmann (John Wiley & Sons, NY, 2003), pp. 1925-1938.

Appendix D Overlapping Area Calculation Algorithm

D.1 Introduction

Here we describe the algorithm for calculating area overlap between images.

The overlapping area is calculated using equation:

$$\text{Overlapping area} = (2a - A)(2b - B) \qquad \text{(Equation D.1)}$$

coming from the overlapping area. (Figure D.1). In the case where the overlapping area is between three or more overlapping frames, pairwise overlapping needs to be calculated.

D.2 MATLAB code for calculating overlapping area

```
clear
NumOfFrames = 2;
size_of_one_frame = 160*172;

S = imread('Full reference frame.jpg');
a = size(S, 1); %height
b = size(S, 2); %width

O = imread('capture 1 overlap.jpg');
A = size(O, 1); %height
B = size(O, 2); %width

Overlap_in_pixel = (a-A)*(b-B);

% unit converstion: 1 pix = ? nm
% width pixels = 160nm
% 1 pix = 160/a nm
% Area conversion factor = pix^2

pix = 160/(b/NumOfFrames);

Overlap_in_nm2 = Overlap_in_pixel*(pix^2)
Total_area = 2*size_of_one_frame - Overlap_in_nm2
```

D.3 Figures

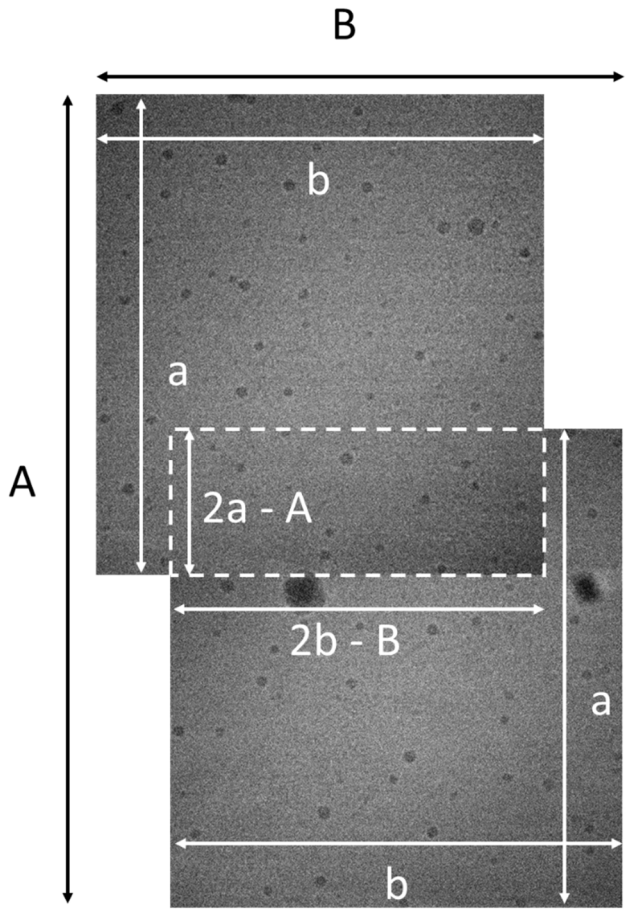

Figure D.1 Illustration of the calculation of overlapping area between frames as described in Equation F.1. The difference in the overlapping imaging and the full image without overlapping came from the overlapping section.

Appendix E Tabulated Data

E.1 Introduction

This appendix lists the tabulated data used in this thesis.

E.2 RHEED Analysis Table

(Tables start next page)

GaN-WZ																					
#	(HKIL)	d-spacing (Å)	$(R_i/R_1)^2$	$(R_i/R_2)^2$	$(R_i/R_3)^2$	$(R_i/R_4)^2$	(R_i/R_5)	$(R_i/R_6)^2$	$(R_i/R_7)^2$	$(R_i/R_8)^2$	$(R_i/R_9)^2$	$(R_i/R_{10})^2$	$(R_i/R_{11})^2$	$(R_i/R_{12})^2$	$(R_i/R_{13})^2$	$(R_i/R_{14})^2$	$(R_i/R_{15})^2$	$(R_i/R_{16})^2$	$(R_i/R_{17})^2$	$(R_i/R_{18})^2$	$(R_i/R_{19})^2$
1	(0001)	5.158	1.000																		
2	(10-10)	2.762	3.488	1.000																	
3	(0002)	2.593	3.957	1.135	1.000																
4	(10-11)	2.437	4.480	1.285	1.132	1.000															
5	(10-12)	1.891	7.440	2.133	1.880	1.661	1.000														
6	(11-20)	1.595	10.464	3.001	2.645	2.336	1.406	1.000													
7	(-211-1)	1.517	11.557	3.314	2.921	2.580	1.553	1.104													
8	(10-13)	1.465	12.398	3.555	3.133	2.768	1.666	1.185	1.000												
9	(20-20)	1.381	13.952	4.001	3.526	3.114	1.875	1.333	1.125	1.000											
10	(11-22)	1.358	14.422	4.135	3.645	3.219	1.938	1.378	1.163	1.034	1.000										
11	(20-21)	1.335	14.939	4.284	3.775	3.335	2.008	1.428	1.205	1.071	1.036	1.000									
12	(0004)	1.296	15.830	4.539	4.001	3.534	2.128	1.513	1.277	1.135	1.098	1.060	1.000								
13	(20-22)	1.219	17.916	5.137	4.528	3.999	2.408	1.712	1.445	1.284	1.242	1.199	1.132	1.000							
14	(10-14)	1.174	19.313	5.538	4.881	4.311	2.596	1.846	1.558	1.384	1.339	1.293	1.220	1.078	1.000						
15	(20-23)	1.079	22.852	6.552	5.775	5.101	3.071	2.184	1.843	1.638	1.584	1.530	1.444	1.275	1.183	1.000					
16	(21-30)	1.044	24.419	7.002	6.171	5.451	3.282	2.334	1.970	1.750	1.693	1.635	1.543	1.363	1.264	1.069	1.000				
17	(21-31)	1.023	25.402	7.284	6.420	5.670	3.414	2.427	2.049	1.821	1.761	1.700	1.605	1.418	1.315	1.112	1.040	1.000			
18	(11-24)	1.006	26.294	7.539	6.645	5.870	3.534	2.513	2.121	1.885	1.823	1.760	1.661	1.468	1.361	1.151	1.077	1.035	1.000		
19	(10-15)	0.971	28.224	8.093	7.133	6.300	3.793	2.697	2.276	2.023	1.957	1.889	1.783	1.575	1.461	1.235	1.156	1.111	1.073	1.000	
20	(21-32)	0.968	28.375	8.136	7.171	6.334	3.814	2.712	2.289	2.034	1.967	1.899	1.792	1.584	1.469	1.242	1.162	1.117	1.079	1.005	1.000
21	(20-24)	0.945	29.779	8.539	7.526	6.648	4.003	2.846	2.402	2.134	2.065	1.993	1.881	1.662	1.542	1.303	1.220	1.172	1.133	1.055	1.049
22	(30-30)	0.921	31.385	8.999	7.932	7.006	4.218	2.999	2.532	2.250	2.176	2.101	1.983	1.752	1.625	1.373	1.285	1.236	1.194	1.112	1.106
23	(0-331)	0.902	32.671	9.368	8.257	7.293	4.391	3.122	2.635	2.342	2.265	2.187	2.064	1.824	1.692	1.430	1.338	1.286	1.243	1.158	1.151
24	(21-33)	0.894	33.318	9.553	8.420	7.437	4.478	3.184	2.687	2.388	2.310	2.230	2.105	1.860	1.725	1.458	1.364	1.312	1.267	1.180	1.174
25	(30-32)	0.868	35.345	10.135	8.932	7.890	4.751	3.378	2.851	2.533	2.451	2.366	2.233	1.973	1.830	1.547	1.447	1.391	1.344	1.252	1.246
26	(0006)	0.864	35.607	10.210	8.999	7.948	4.786	3.403	2.872	2.552	2.469	2.383	2.249	1.987	1.844	1.558	1.458	1.402	1.354	1.262	1.255
27	(02-25)	0.825	39.076	11.205	9.875	8.723	5.252	3.734	3.152	2.801	2.709	2.616	2.468	2.181	2.023	1.710	1.600	1.538	1.486	1.385	1.377
28	(22-40)	0.790	42.629	12.223	10.773	9.516	5.730	4.074	3.438	3.055	2.956	2.854	2.693	2.379	2.207	1.865	1.746	1.678	1.621	1.510	1.502
29	(4-2-2-2)	0.759	46.231	13.256	11.684	10.320	6.214	4.418	3.729	3.314	3.206	3.095	2.920	2.580	2.394	2.023	1.893	1.820	1.758	1.638	1.629
30	(2-1-1-6)	0.756	46.550	13.348	11.764	10.391	6.257	4.448	3.755	3.336	3.228	3.116	2.941	2.598	2.410	2.037	1.906	1.833	1.770	1.649	1.641
31	(02-26)	0.729	50.076	14.359	12.655	11.178	6.731	4.785	4.039	3.589	3.472	3.352	3.163	2.795	2.593	2.191	2.051	1.971	1.904	1.774	1.765
32	(0-332)	0.712	52.519	15.059	13.273	11.724	7.059	5.019	4.236	3.764	3.642	3.516	3.318	2.931	2.719	2.298	2.151	2.067	1.997	1.861	1.851
33	(0-440)	0.687	56.303	16.144	14.229	12.568	7.568	5.380	4.541	4.035	3.904	3.769	3.557	3.143	2.915	2.464	2.306	2.216	2.141	1.995	1.984

Table E.1 d-spacing ratio squared table for WZ.

GaN-ZB																						
#	(hkl)	d-spacing (Å)	$(R_i/R_1)^2$	$(R_i/R_2)^2$	$(R_i/R_3)^2$	$(R_i/R_4)^2$	$(R_i/R_5)^2$	$(R_i/R_6)^2$	$(R_i/R_7)^2$	$(R_i/R_8)^2$	$(R_i/R_9)^2$	$(R_i/R_{10})^2$	$(R_i/R_{11})^2$	$(R_i/R_{12})^2$	$(R_i/R_{13})^2$	$(R_i/R_{14})^2$	$(R_i/R_{15})^2$	$(R_i/R_{16})^2$	$(R_i/R_{17})^2$	$(R_i/R_{18})^2$	$(R_i/R_{19})^2$	$(R_i/R_{20})^2$
1	(001)	4.520	1.000																			
2	(110)	3.196	2.000	1.000																		
3	(111)	2.599	3.025	1.512	1.000																	
4	(200)	2.250	4.036	2.018	1.334	1.000																
5	(021)	2.021	5.000	2.500	1.653	1.239	1.000															
6	(220)	1.592	8.061	4.031	2.665	1.997	1.612	1.000														
7	(003)	1.507	9.000	4.500	2.976	2.230	1.800	1.116	1.000													
8	(311)	1.358	11.078	5.539	3.663	2.745	2.216	1.374	1.231	1.000												
9	(222)	1.300	12.089	6.044	3.997	2.996	2.418	1.500	1.343	1.091	1.000											
10	(400)	1.126	16.114	8.057	5.328	3.993	3.223	1.999	1.790	1.455	1.333	1.000										
11	(331)	1.033	19.146	9.573	6.330	4.744	3.829	2.375	2.127	1.728	1.584	1.188	1.000									
12	(204)	1.011	20.000	10.000	6.613	4.956	4.000	2.481	2.222	1.805	1.654	1.241	1.045	1.000								
13	(224)	0.923	24.000	12.000	7.935	5.947	4.800	2.977	2.667	2.166	1.985	1.489	1.254	1.200	1.000							
14	(115)	0.870	27.000	13.500	8.927	6.690	5.400	3.349	3.000	2.437	2.233	1.676	1.410	1.350	1.125	1.000						
15	(440)	0.799	32.000	16.000	10.580	7.929	6.400	3.970	3.556	2.889	2.647	1.986	1.671	1.600	1.333	1.185	1.000					
16	(135)	0.764	35.000	17.500	11.572	8.673	7.000	4.342	3.889	3.159	2.895	2.172	1.828	1.750	1.458	1.296	1.094	1.000				
17	(244)	0.7533	36.000	18.000	11.903	8.921	7.200	4.466	4.000	3.250	2.978	2.234	1.880	1.800	1.500	1.333	1.125	1.029	1.000			
18	(600)	0.753	36.000	18.000	11.903	8.921	7.200	4.466	4.000	3.250	2.978	2.234	1.880	1.800	1.500	1.333	1.125	1.029	1.000			
19	(335)	0.689	43.000	21.500	14.217	10.655	8.600	5.334	4.778	3.881	3.557	2.669	2.246	2.150	1.792	1.593	1.344	1.229	1.194	1.000		
20	(622)	0.681	44.000	22.000	14.548	10.903	8.800	5.458	4.889	3.972	3.640	2.731	2.298	2.200	1.833	1.630	1.375	1.257	1.222	1.023	1.000	
21	(551)	0.633	51.000	25.500	16.862	12.637	10.200	6.327	5.667	4.604	4.219	3.165	2.664	2.550	2.125	1.889	1.594	1.457	1.417	1.186	1.159	1.000
22	(642)	0.604	56.000	28.000	18.515	13.876	11.200	6.947	6.222	5.055	4.632	3.475	2.925	2.800	2.333	2.074	1.750	1.600	1.556	1.302	1.273	1.098
23	(535)	0.588	59.000	29.500	19.507	14.620	11.800	7.319	6.556	5.326	4.880	3.661	3.082	2.950	2.458	2.185	1.844	1.686	1.639	1.372	1.341	1.157
24	(800)	0.565	64.000	32.000	21.160	15.859	12.800	7.939	7.111	5.777	5.294	3.972	3.343	3.200	2.667	2.370	2.000	1.829	1.778	1.488	1.455	1.255
25	(733)	0.552	67.000	33.500	22.152	16.602	13.400	8.312	7.444	6.048	5.542	4.158	3.499	3.350	2.792	2.481	2.094	1.914	1.861	1.558	1.523	1.314
26	(644)	0.548	68.000	34.000	22.483	16.850	13.600	8.436	7.556	6.138	5.625	4.220	3.552	3.400	2.833	2.519	2.125	1.943	1.889	1.581	1.545	1.333
27	(660)	0.533	72.000	36.000	23.805	17.841	14.400	8.932	8.000	6.499	5.956	4.468	3.761	3.600	3.000	2.667	2.250	2.057	2.000	1.674	1.636	1.412
28	(555)	0.522	75.000	37.500	24.797	18.584	15.000	9.304	8.333	6.770	6.204	4.654	3.917	3.750	3.125	2.778	2.344	2.143	2.083	1.744	1.705	1.471
29	(662)	0.518	76.000	38.000	25.128	18.832	15.200	9.428	8.444	6.860	6.287	4.716	3.970	3.800	3.167	2.815	2.375	2.171	2.111	1.767	1.727	1.490
30	(664)	0.482	88.000	44.000	29.095	21.806	17.600	10.917	9.778	7.943	7.279	5.461	4.596	4.400	3.667	3.259	2.750	2.514	2.444	2.047	2.000	1.725
31	(666)	0.435	108.000	54.000	35.708	26.762	21.600	13.398	12.000	9.749	8.934	6.702	5.641	5.400	4.500	4.000	3.375	3.086	3.000	2.512	2.455	2.118

Table E.2 d-spacing ratio squared table for ZB.

E.3 Tables of indexed RHEED patterns

(The table is on the next page)

Sample	Flux series	Polytypes and nanostructure	RHEED capture time	Identified polytype	Identified planes
R1102	Low-low	WZ NW	10 mins	WZ	$(10\bar{1}2)$, $(\bar{2}11\bar{1})$*, (0004), $(20\bar{2}2)$, $(30\bar{3}0)$*, $(30\bar{3}2)$, $(02\bar{2}5)$
R1102	Low-low	WZ NW	10 mins	WZ	$(11\bar{2}0)$, $(20\bar{2}0)$*, $(20\bar{2}2)$, $(10\bar{1}4)$, $(21\bar{3}2)$, $(21\bar{3}3)$, $(30\bar{3}2)$, (0006)
R1099	Low-low	WZ NW	1 hr	WZ	$(11\bar{2}0)$, $(20\bar{2}0)$, $(10\bar{1}4)$, $(20\bar{2}3)$, (0006), $(02\bar{2}5)$
R1101	Low-low	WZ NW	2 hrs	WZ	$(10\bar{1}0)$, $(10\bar{1}2)$, $(10\bar{1}3)$, $(20\bar{2}1)$, (0004), $(21\bar{3}2)$, (0006)
R1101	Low-low	WZ NW	2 hrs	WZ	$(10\bar{1}3)$, $(20\bar{2}0)$*, $(10\bar{1}4)$, $(20\bar{2}3)$*,$(21\bar{3}0)$, $(21\bar{3}1)$, $(21\bar{3}3)$
R1100	Low-low	WZ NW	2 hrs	WZ	$(21\bar{3}0)$, $(21\bar{3}1)$, $(11\bar{2}4)$, $(20\bar{2}4)$
R1090	High-high	ZB/WZ film	5 mins	ZB	(220), (222) *, (331), (244), (335)
R1090	High-high	ZB/WZ film	15 mins	ZB	(220), (222), (331), (244), (335)
R1090	High-high	ZB/WZ film	15 mins	ZB	(111), (222), (331), (204), (244), (335)
R1082	High-high	ZB/WZ film	22 mins	ZB	(400), (331), (440)
R1081	High-high	ZB/WZ film	22 mins	ZB	(220), (331), (115), (244)
R1081	High-high	ZB/WZ film	23 mins	ZB	(220), (400), (331)*, (204)*, (440), (244)
R1089	High-high	ZB/WZ film	30 mins	WZ	$(11\bar{2}0)$, $(20\bar{2}0)$, $(11\bar{2}4)$, $(21\bar{3}2)$, $(02\bar{2}5)$
R1089	High-high	ZB/WZ film	30 mins	WZ	$(10\bar{1}3)$, (0004), $(20\bar{2}2)$*, $(21\bar{3}1)$, $(10\bar{1}5)$, $(20\bar{2}4)$, $(02\bar{2}5)$
R1095	High-high	ZB/WZ film	2.5 hrs	WZ	$(10\bar{1}3)$, $(20\bar{2}2)$,$(21\bar{3}4)$, $(20\bar{2}4)$, $(30\bar{3}2)$,
R1142	High-low	ZB/WZ NW	20 mins	WZ	(0002), $(21\bar{3}1)$*, $(11\bar{2}4)$, $(21\bar{3}2)$
R1141	High-low	ZB/WZ NW	2.5 hrs	WZ	$(10\bar{1}1)$, $(\bar{2}11\bar{1})$, $(20\bar{2}2)$, $(20\bar{2}2)$, $(20\bar{2}3)$, $(21\bar{3}0)$, $(10\bar{1}5)$, $(30\bar{3}0)$, (0006) , $(02\bar{2}5)$
R1142	High-low	ZB/WZ NW	2.5 hrs	WZ	(0002), $(10\bar{1}3)$, $(11\bar{2}2)$, $(20\bar{2}1)$, $(10\bar{1}4)$, $(21\bar{3}0)$, $(11\bar{2}4)$, $(21\bar{3}2)$, (0006)

Table E.3 Table of RHEED analysis for RHEED patterns discussed in Chapter 5, as well as additional RHEED patterns of WZ NWs, WZ-on-ZB films, and WZ-on-ZB NWs. Additional features are indicated with an asterisk.

E.4 Samples studied in this thesis

Sample #	Substrate	Ga flux		Plasma	N Flux
		pre-dep	nitridation		
RMBE 1081	Si(100)	1.5E-07	1.5E-07	400W/1 sccm	9.6E-07
RMBE 1082	Si(100)	7.8E-08	7.8E-08	400W/1 sccm	9.7E-07
RMBE 1089	Si(100)	9E-10	9E-10	400W/1 sccm	1E-06
RMBE 1090	Si(100)	1.5E-07	1.5E-07	400W/1 sccm	9.7E-07
RMBE 1091	Si(100)	1.5E-07	1.5E-07	400W/1 sccm	9.7E-07
RMBE 1095	Si(100)	1.5E-07	1.5E-07	400W/1 sccm	1.0E-06
RMBE 1099	Si(100)	3E-08	3E-08	400W/1 sccm	1.0E-06
RMBE 1100	Si(100)	2.0E-08	2.0E-08	400W/1 sccm	1.0E-06
RMBE 1101	Si(100)	3.0E-08	3.0E-08	400W/1 sccm	1.0E-06
RMBE 1102	Si(100)	1.5E-08	1.5E-08	400W/1 sccm	1E-06
RMBE 1141	Si(100)	1.5E-07	3.0E-08	400W/1 sccm	1E-06
RMBE 1142	Si(100)	3.0E-07	3.0E-08	400W/1 sccm	1E-06
RMBE 1391	Si(100)	3.0E-08	7.6E-09	350W/0.35 sccm	2.6E-07
RMBE 1396	Si(100)	3.0E-08	7.6E-09	350W/0.35 sccm	2.7E-07

Table E.4 Table of GaN NW samples studied in Chapter 5. RMBE 1391 and RMBE 1396 are done by Hongling Lott. The rest of the samples are done by Sunyeol Jeon.

Sample #	substrate	$T_{final\text{-}nit}$ (°C)
RMBE 969	Si(001)	550
RMBE 972	Si(001)	550
RMBE 970	Si(001)	650
RMBE1009	Si(001)	650
RMBE 909	Si(001)	720
RMBE 911	Si(001)	720
RMBE 921	Si(111)	550
RMBE 920	Si(111)	650
RMBE 983	Si(111)	720
RMBE 867	Silica	550
RMBE 868	Silica	550
RMBE 882	Silica	550
RMBE 866	Silica	650
RMBE 883	Silica	650
RMBE 884	Silica	700

Table E.5 Table of GaN QD samples studied in Chapter 3. The substrate temperature during initial nitridation and Ga droplet step is 550 °C for all samples. The time for initial nitridation is 10 mins for all samples. The equivalent monolayer for deposited Ga droplets is 7.5 ML for all samples.

Sample #	In BEP (Torr)	In deposition time (sec)	The equivalent monolayer for deposited In (ML)
RMBE 1220	1.0 E-7	30	3
RMBE 1221	1.0 E-7	80	8
RMBE 1222	1.0 E-7	50	5
RMBE 1223	1.0 E-7	40	4
RMBE 1224	1.0 E-7	65	6.5
RMBE 1225	1.0 E-7	50	5

Table E.6 Table of indium droplet samples mentioned in Chapter 4. Si(001) wafers with SiMPore TEM grid indium mounted are used for all samples.

E.5 Parameters used in nextnano simulation

Parameter name	material		Reference
	WZ GaN	**ZB GaN**	
lattice constant a	3.189 Å	4.5 Å	I. Vurgaftman et al [1]
lattice constant c	5.185 Å	----	I. Vurgaftman et al [1]
Conduction band energies	2.80 eV	2.58 eV	P. Rinke et al [2]
Valence band energies	-0.73 eV	-0.73 eV	P. Rinke et al [2]
Heavy-hole effective mass m_{hh}	1.4 m_e	1.3 m_e	M.E. Levinshtein [3]
Light-hole effective mass m_{lh}	0.3 m_e	0.19 m_e	M.E. Levinshtein [3]
Spin-orbit splitting effective mass m_{so}	0.6 m_e	0.33 m_e	M.E. Levinshtein [3]
Varshni parameter β	830		I. Vurgaftman et al [1]
Varshni parameter γ	0.909		I. Vurgaftman et al [1]

Table E.7 Table of parameters, their values, and the references used in nextnano to plot Figure 7.1, as discussed in Chapter 7 .

E.6 References

[1] I. Vurgaftman, J.R. Meyer, and L.R. Ram-Mohan, "Band parameters for III–V compound semiconductors and their alloys", Jpn. J. Appl. Phys. 89, 5815 (2001).

[2] P. Rinke, M. Scheffler, A. Qteish, M. Winkelnkemper, D. Bimberg, and J. Neugebauer, "Band gap and band parameters of InN and GaN from quasiparticle energy calculations based on exact-exchange density-functional theory", Appl. Phys. Lett. 89, 161919 (2006).

[3] M.E Levinshtein, S.L. Rumyantsev, and M.S. Shur, *Properties of Advanced Semiconductor Materials: GaN, AlN, InN, BN, SiC, SiGe* (Wiley 2001).

Appendix F Material Parameters

F.1 Introduction

This Appendix lists a variety of materials parameters used in this research. Table F.1 and Table F.2 are the table of d-spacings for GaN WZ and ZB, used in Chapter 3 and Chapter 5. Table F.3 is a table for lattice spacings from planes from WZ InN, ZB InN, Silicon, and In_2O_3 used in Chapter 4. Table F.4 is a table of parameters used in DFT calculations, used in Chapter 3.

F.2 Tables

(Tables start next page)

Appendix G #	(HKIL)	h	k	l	d-spacing (Å) - Bragg's Law	2Theta (◦)
1	(10-10)	1	0	0	2.76	32.39
2	(0002)	0	0	2	2.60	34.56
3	(10-11)	1	0	1	2.44	36.85
4	(10-12)	1	0	2	1.89	48.08
5	(11-20)	1	1	0	1.60	57.77
6	(10-13)	1	0	3	1.47	63.45
7	(20-20)	2	0	0	1.38	67.81
8	(11-22)	1	1	2	1.36	69.10
9	(20-21)	2	0	1	1.33	70.51
10	(0004)	0	0	4	1.30	72.91
11	(20-22)	2	0	2	1.22	78.41
12	(10-14)	1	0	4	1.17	82.03
13	(20-23)	2	0	3	1.08	91.10
14	(21-30)	2	1	0	1.04	95.12
15	(21-31)	2	1	1	1.02	97.64
16	(11-24)	1	1	4	1.01	99.95
17	(10-15)	1	0	5	0.97	105.00
18	(21-32)	2	1	2	0.97	105.40
19	(20-24)	2	0	4	0.95	109.16
20	(30-30)	3	0	0	0.92	113.57
21	(21-33)	2	1	3	0.89	119.08
22	(30-32)	3	0	2	0.87	125.20
23	(0006)	0	0	6	0.87	126.03
24	(02-25)	0	2	5	0.83	137.98
25	(22-40)	2	2	0	0.80	154.34

Table F.1 Table of d-spacing and 2θ for WZ GaN with lattice parameters a = 3.29 Å and c = 5.19 Å.

#	(hkl)	h	k	l	d-spacing (Å) - Bragg's Law	2θ (◦)
1	(111)	1	1	1	2.61	34.48
2	(200)	2	0	0	2.26	40.04
3	(220)	2	2	0	1.60	57.87
4	(311)	3	1	1	1.36	69.11
5	(222)	2	2	2	1.30	72.67
6	(400)	4	0	0	1.13	86.33
7	(331)	3	3	1	1.04	96.43
8	(204)	2	0	4	1.01	99.30
9	(224)	2	2	4	0.92	113.20
10	(115)	1	1	5	0.87	124.63
11	(440)	4	4	0	0.80	149.17

Table F.2 Table of d-spacing and 2θ for ZB GaN with lattice parameters a = 4.52 Å.

(a)

InN - WZ	
(hkil)	d (Å)
(0001)	5.70
(10-10)	3.06
(0002)	2.85
(10-11)	2.70
(10-12)	2.09
(11-20)	1.77
(10-13)	1.62
(20-20)	1.53
(11-22)	1.50
(20-21)	1.48
(0004)	1.43
(20-22)	1.35

(b)

InN - ZB	
(hkl)	d (Å)
(001)	4.53
(111)	2.62
(200)	2.27
(220)	1.6
(311)	1.37
(222)	1.30
(400)	1.13
(331)	1.04
(420)	1.01
(422)	0.93
(511)	0.87
(440)	0.80

(c)

Silicon	
(hkl)	d (Å)
(001)	5.47
(011)	3.86
(111)	3.14
(220)	1.92
(311)	1.64
(222)	1.57
(400)	1.36
(331)	1.25
(422)	1.11
(333)	1.05
(511)	1.05
(440)	0.92
(531)	0.91

(d)

In_2O_3	
(hkl)	d (Å)
(001)	10.11
(011)	7.15
(111)	5.84
(220)	3.57
(311)	3.04
(222)	2.92
(400)	2.53
(331)	2.32
(422)	2.06
(333)	1.95
(511)	1.95
(440)	1.79
(531)	0.94

Table F.3 Lattice spacings from planes from WZ InN, ZB InN, Silicon, and In_2O_3 (indium oxide) from © 2021 International Centre for Diffraction Data.

Lattice parameters	Prior simulation[11,12]	Experiment[13,14]	This work
$\mathbf{a_{Si}}$ (Å)	5.424	5.431	5.465
$\mathbf{a_{SiO2(quartz)}}$ (Å)	5.020	4.9965	5.107
$\mathbf{c_{SiO2(quartz)}}$ (Å)	5.560	5.4570	5.578

Table F.4 Table of DFT computed lattice parameters for Si and SiO_2, in comparison with computed[11,12] and experimental[1,2] literature reports.

G.1 References

[1] M.G. Ganchenkova, I.A. Supriadkina, K.K. Abgaryan, D.I. Bazhanov, I.V. Mutigullin, and V.A. Borodin, “Influence of the ab initio Calculation Parameters on Prediction of Energy of Point Defects in Silicon”, Mod. Electron. Mater. 1, 103 (2015).

[2] E. Bourova and P. Richet, “Quartz and cristobalite: High-temperature cell parameters and volumes of fusion”, Geophysical Research Letters 25, 2333 (1998).